Pressure and temperature dependence of recombination reactions of benzyl-type radicals

Dissertation

zur Erlangung des Doktorgrades

der Mathematisch-Naturwissenschaftlichen Fakultäten

der Georg-August-Universität zu Göttingen

vorgelegt von

Changyoul Lee

aus Cheonan, Südkorea

Göttingen 2008

D7

Referent :   **Prof. Dr. J. Troe**

Korreferent :   **PD Dr. T. Lenzer**

Tag der mündlichen Prüfung : 27. Oktober 2008

Table of contents

Summary

The combination reactions p-F-C$_6$H$_4$CH$_2$ + p-F-C$_6$H$_4$CH$_2$ (+M) $\rightarrow$ C$_{14}$H$_{12}$F$_2$ (+M), p-CH$_3$-C$_6$H$_4$CH$_2$ + p-CH$_3$-C$_6$H$_4$CH$_2$ (+M) $\rightarrow$ C$_{16}$H$_{18}$ (+M) and C$_6$H$_5$CH$_2$ + C$_6$H$_5$CH$_2$ (+M) $\rightarrow$ C$_{14}$H$_{14}$ (+M) have been investigated over the pressure $0.2 - 800$ bar and the temperature $255 - 420$ K for p-fluorobenzyl radicals, the pressure $2 - 200$ bar and the temperature $300 - 515$ K for p-methylbenzyl radicals, and the pressure $1 - 70$ bar and temperature $250 - 400$ K for benzyl radicals. Helium, argon, CO$_2$, SF$_6$, CF$_3$H and CF$_4$ were used as bath gases. Additionally, transient UV absorption spectra of p-fluorobenzyl and p-methylbenzyl radicals were determined at 300 K from single – wavelength transient absorption measurements. Radicals were generated via the laser photolysis of Cl$_2$ at 308 nm and the subsequent hydrogen abstraction of precursor molecules by chlorine atom. The transient absorption signals of p-fluorobenzyl and benzyl radicals were measured at 253 nm and of p-methylbenzyl radicals at 260 nm. The absorption coefficients of p-fluorobenzyl and p-methylbenzyl radicals were determined as :

$$\sigma_{p-fluorobenzyl}(253\,\text{nm}, 300\,K) = 8.4 \times 10^{-17}\,\text{cm}^2\text{molecule}^{-1}$$

and

$$\sigma_{p-methylbenzyl}(260\,\text{nm}, 300K) = 5.0 \times 10^{-17}\,\text{cm}^2\text{molecule}^{-1}.$$

There was an experimental indication of the weak pressure dependence of the absorption coefficient of p-fluorobenzyl, p-methylbenzyl and benzyl radicals in CO$_2$ over the pressure range $1 - 45$ bar. The rate constants of three reactions reached a pressure-independent range at below 1 bar, such that the limiting "high-pressure" rate constants of the energy-transfer (ET) mechanism, $k_{1,\infty}^{ET}$ could be determined from the experimental results without falloff extrapolation. Also the temperature dependence of the $k_{1,\infty}^{ET}$ were investigated and our results can be expressed as, respectively:

$$k_{1,\infty}^{ET}(T) = (4.3 \pm 0.5) \times 10^{-11} (\frac{T}{300\text{K}})^{-0.2}\,\text{cm}^3\text{molecule}^{-1}\text{s}^{-1} \qquad \text{for } p\text{-fluorobenzyl radical}$$

and

$$k_{1,\infty}^{ET}(T) = (3.3 \pm 0.25) \times 10^{-11} (\frac{T}{300\text{K}})^{-0.89}\,\text{cm}^3\text{molecule}^{-1}\text{s}^{-1} \qquad \text{for } p\text{-methylbenzyl radical}$$

The dependences of k_1 on temperature, and density for p-fluorobenzyl and p-methylbenzyl radicals were similar to those for benzyl radicals. The magnitude of enhancement of the rate

constants increased in the order He < Ar < CO_2 in all three radicals. The decrease of the rate constant after passing over the maximum were observed in all three radical recombination reactions studied in this work, which can be attributed to a transition to diffusion-controlled kinetics.

Acknowledgement

I also take this opportunity to thank the people of the Korean Church in Göttingen who made my stay here very pleasant and fruitful.

My little son, Minjae!!   Your smile is the best recreation for Daddy!

Finally my biggest thanks go to Hanna, my dear wife and steady companion. Her warm love, confidence and prayer made me feel at home anywhere. Thanks for exploring the highs and lows of life with me.

Chapter 1

Introduction

The pressure- and temperature-dependence of the radical recombination and the corresponding unimolecular dissociation rate constants have been one of the interesting subjects in experimental and theoretical kinetic aspects, because they reflect the important influence of the surrounding medium on the dynamics of these processes. Especially, addition and recombination processes involving organic free radicals play an important role in fundamental kinetic studies as well as in the applied sciences such as combustion or atmospheric chemistry as key intermediates.

In radical combination kinetics, collisional energy transfer in low-pressure gases and molecular diffusion at the high densities of liquid solutions are the well understood extremes of the rate-limiting intermolecular interactions. However, in the intermediate regime between high-density gases and liquids, the superposition of various reactant-solvent interactions is not yet well understood. As the rates of the combination reactions depend on several factors, such as the concentration of the reactants, temperature and also the concentration of the bath gases and their chemical nature, it is difficult to understand fully the radical combination kinetics in the gas-to-liquid transition range. In this range, interactions between solutes and bath gases, forming van der Waals complexes, may influence chemical reaction dynamics.

For formation of stable products combination reactions always require some energy removal process in addition to the actual reactant encounter dynamics. The well-established "Energy Transfer" (ET) mechanism includes association, dissociation, and collisional energy transfer steps. These mechanisms characterize the pressure dependence of the rate coefficient

k between the low-pressure and high-pressure limiting ranges. Linear pressure dependence of the rate constant at low pressures is followed by a transition regime leading into the "high pressure" range with a constant, limiting value, k_∞, independent of the density and nature of the bath gas. In general, this leads to the typical ("fall-off") pressure dependence of such reactions.

In the gas-to-liquid range, ordinary van der Waals reactant-bath gas complexes may play important roles in combination reaction dynamics much more often than commonly believed The alternative "Radical-Complex (RC)" mechanism (also "chaperon" mechanism) involves van der Waals reactant-bath gas complexes and has early been proposed to explain peculiarities in atom recombinations. But since then it has generally been assumed to be of marginal importance apart from atom recombination or possibly some cases of triatomic products. The RC mechanism is still a hypothesis. However, recently, there have been several experimental results which can be consistently interpreted within the radical-complex mechanism. These can be found in extensive experimental studies on pressure- and temperature-dependent rate constants of atom and radical recombination reactions from the Troe group: For example, indications of the involvement of the radical complex mechanism can be found in atoms or small radicals in refs. 1-6. More recently, an unexpected enhancement of combination rates of intermediate sized-polyatomic radicals, such as CCl_3[7] or CH_3,[8] was observed. The most prominent indication for the RC mechanism has been found in density-dependent recombination rate constants of benzyl-type radicals.[9-11] A clear enhancement of recombination rate constants was observed at higher pressures, larger than those where the "high-pressure limit" of the ET mechanism was already established. New evidence for a more general importance of the RC mechanism may also provide a considerable challenge for theoretical analysis, which has so far been focused overwhelmingly only on the ET mechanism.
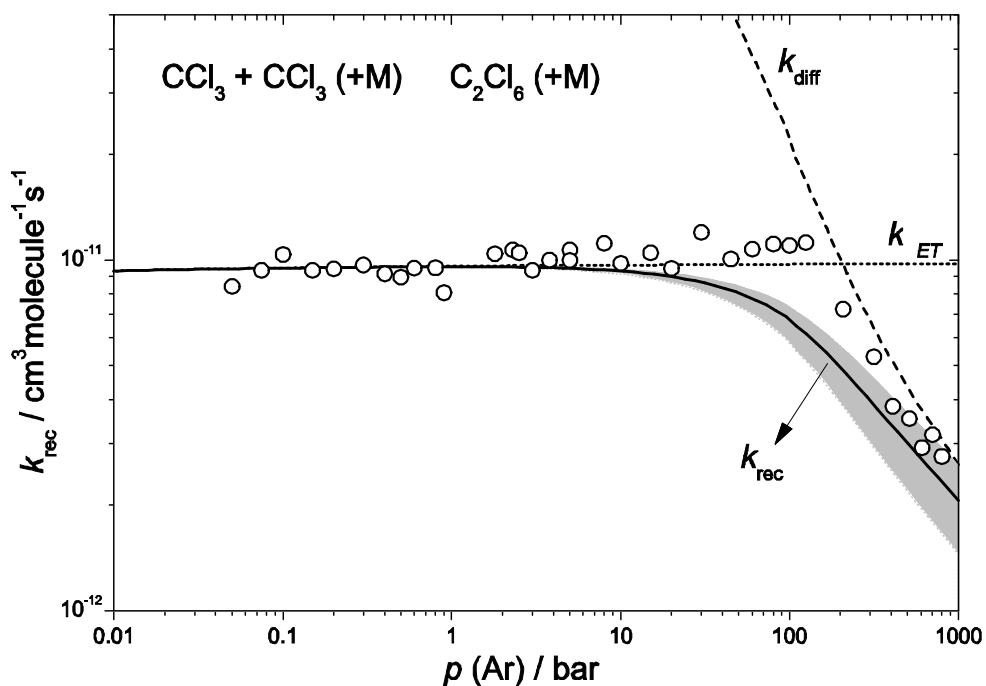
Figure 1.1 Combination rate constants k_{rec} in the bath gas Ar at 300 K showing the transition to the onset of diffusion control. Dashed line: limiting diffusion-controlled rate constants. Dotted line: k^{ET} from the energy transfer mechanism. Solid line: rate constants without contribution from the radical-complex mechanism, error estimation of the calculation illustrated by the shaded area. The figure was taken from ref. 12.
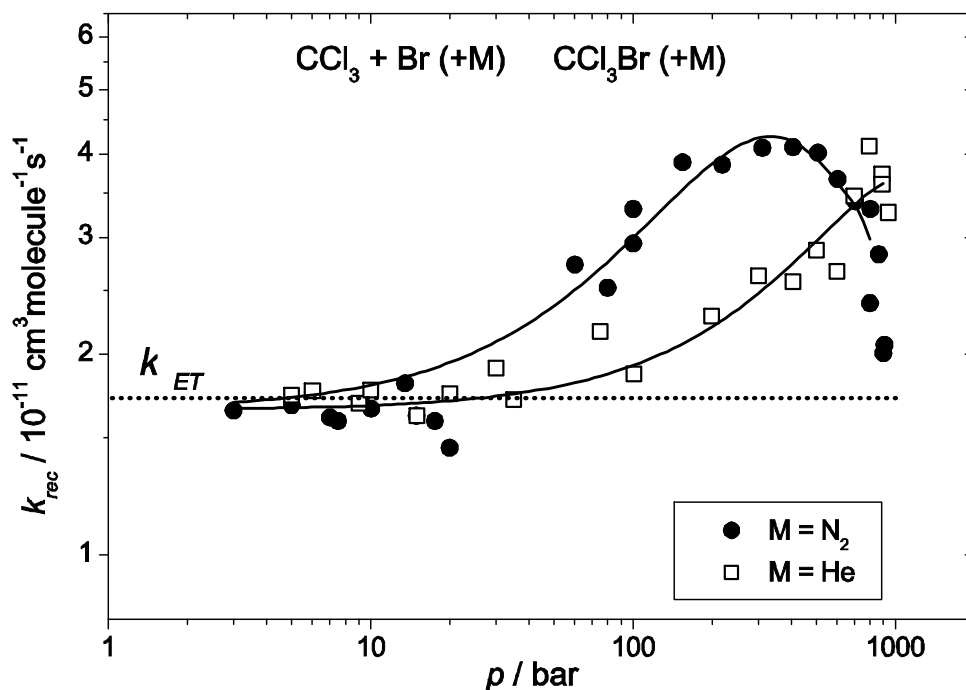
Figure 1.2 Combination rate constants of $CCl_3 + Br (+ M) \rightarrow CCl_3Br (+ M)$ at 300 K: measurements in the bath gases He and N_2. The figure was taken from ref. 12.

3
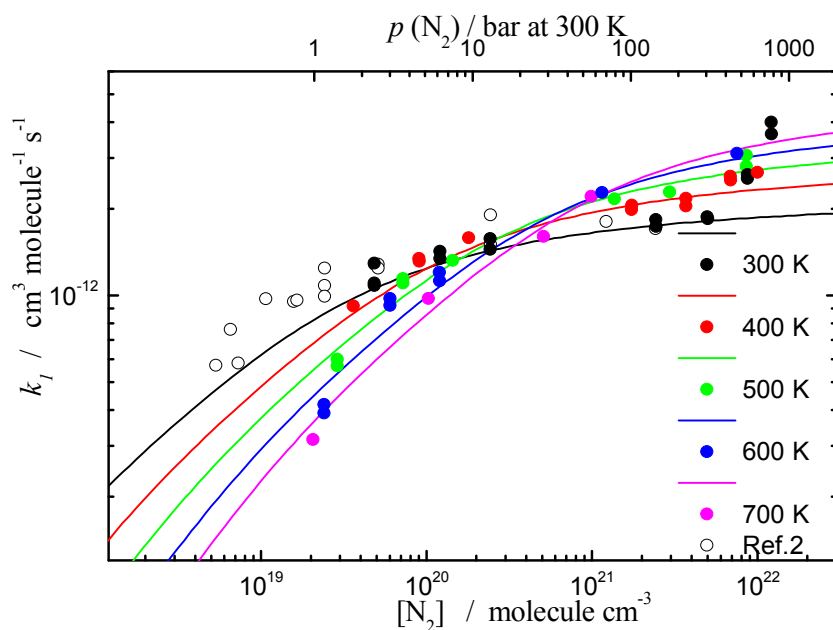
Figure 1.3   Combination rate constants of $CH_3 + O_2\,(+\,M) \rightarrow CH_3O_2\,(+\,M)$ at various temperatures.[8] The deviation of k_{rec} values at 300 K in the high density region from the expected values based on the energy transfer mechanism (lines) was observed. Note that this deviation is disappearing at higher temperatures.
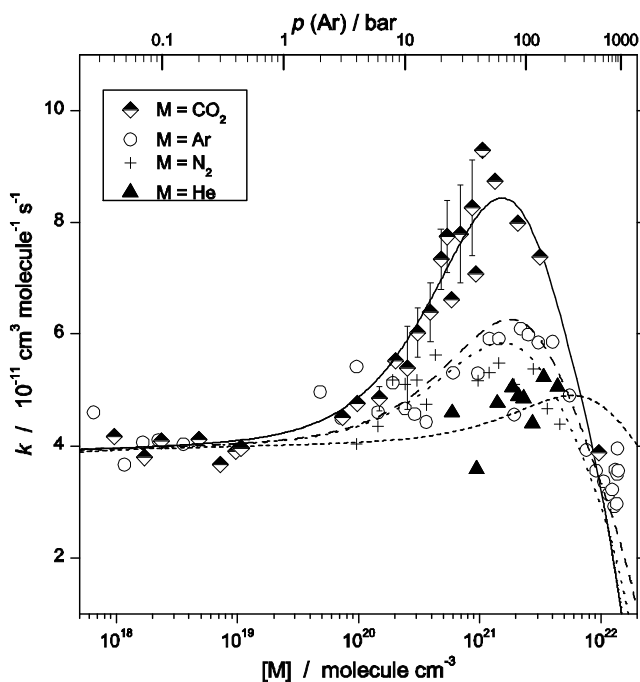
Figure 1.4   Density dependence of the self-combination rate constant of benzyl radicals in helium, argon, N_2 and CO_2 at 300 K.[9] The enhancement of recombination rate constants at higher densities was clearly observed in the order $CO_2 > Ar \approx N_2 > He$.

1.1 Energy-Transfer (ET) mechanism

The theoretical analysis of bimolecular reactions is often difficult because several reactions, such as complex formation, complex dissociation and rearrangement, compete. In general, bimolecular recombination reactions can be written as:

$$A \quad + \quad B \quad \rightleftarrows \quad AB^* \quad \rightarrow \quad AB \tag{R.1}$$

The reactant can be activated due to collisions to form AB* which then might be deactivated due to collisions or form products. The difference between Energy-Transfer (ET) and Radical-Complex (RC) mechanisms is how the activated adduct AB* can be stabilized to produce AB. In the energy-transfer mechanism, stabilization of activated complex takes place by intermolecular energy transfer via collisions with the bath gas molecules. On the other hand, in the Radical-Complex mechanism, the product AB is formed via intramolecular energy transfer of the radical-bath gas molecule complexes.

Falloff curves of unimolecular dissociation and the reverse radical recombination reactions characterize the pressure dependence of the rate coefficients k between the low–pressure and high–pressure limiting ranges. Theories of unimolecular reactions are commonly discussed on the basis of mechanism involving collisional energy transfer, which was originally proposed by Lindemann and Christiansen.[13,14]

The energy-transfer mechanism can be formulated symbolically in terms of the steps

$$A \quad + \quad B \quad \xrightarrow{k_1} \quad AB^* \tag{R 2}$$

$$AB^* \quad \xrightarrow{k_{-1}} \quad A \quad + \quad B \tag{R 3}$$

$$AB^* \quad + \quad M \quad \xrightarrow{k_2} \quad AB \quad + \quad M \tag{R 4}$$
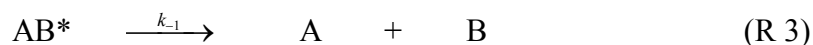
where A and B denote atom or radical and M is the third body partner. Under the assumption of the steady-state concentration of AB*, the reaction rate for the product formation can be written as:

$$\frac{1}{[A][B]} \frac{d[AB]}{dt} = k_{rec} = k_1 \left(\frac{k_2[M]}{k_{-1} + k_2[M]} \right) \tag{1.1}$$

5

Eqn 1.1 can be simplified and written as:

$$k_{ET,rec} = k_{ET,\infty} \times \frac{k_{ET,0}[M]}{k_{ET,\infty} + k_{ET,0}[M]} \qquad (1.2)$$

with the limiting low-pressure rate coefficient when $[M] \rightarrow 0$,

$$k_{ET,0} = (k_1/k_{-1})\, k_2\, [M] \qquad (1.3)$$

which is characterized by an equilibrium between A, B, and AB*, and the limiting high–pressure rate coefficient when $[M] \rightarrow \infty$,

$$k_{ET,\infty} = k_1 \qquad (1.4)$$

which is characterized by the rate-determining association of A and B forming AB*; here, AB* is efficiently depleted by fast collisional stabilization. Eqn. 1.3 shows that at very low pressures the first order rate constant increases linearly with the bath gas concentration and at very high pressures it becomes pressure independent.

Figure 1.5 shows the schematic representation of the Energy-Transfer (ET) mechanism.
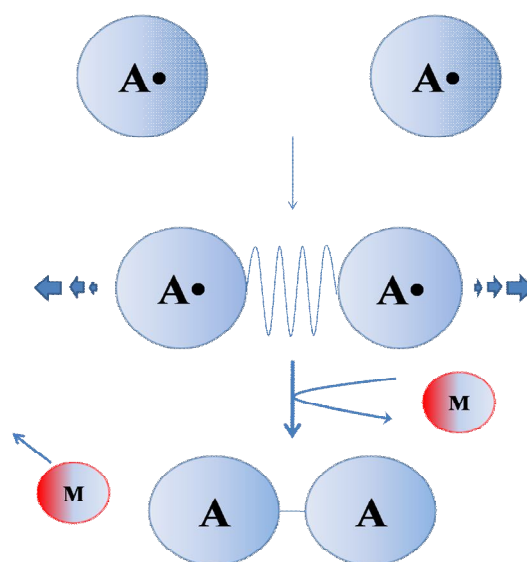
Figure 1.5   Schematic representation of the energy-transfer (ET) mechanism.

The "reduced form" of the recombination rate constant is derived by dividing eqn. 1.2 by the limiting high-pressure rate coefficient:

$$\frac{k_{rec}^{ET}}{k_{ET,\infty}} = \frac{k_{ET,0}[M]/k_{ET,\infty}}{1+k_{ET,0}[M]/k_{ET,\infty}} \qquad (1.5)$$

Eqn. 1.5 is the reduced fall-off expression of the Lindemann model and has a particularly simple form. Unfortunately, the experimental fall-off curves were not well represented by eqn. 1.5. By introducing "broadening factors" $F(k_{ET,0}/k_{ET,\infty})$,[15] the deviation can be compensated. The broadening of the reduced fall-off expressions are represented as

$$\frac{k_{rec}^{ET}}{k_{ET,\infty}} = \frac{k_{ET,0}[M]/k_{ET,\infty}}{1+k_{ET,0}[M]/k_{ET,\infty}} F(k_{ET,0}/k_{ET,\infty}) \qquad (1.6)$$

The details of broadening factors depend on the correct choice of $k_{ET,0}$ and $k_{ET,\infty}$. The "center broadening factors"

$$F_{cent} \quad = \quad F(k_{ET,0}/k_{ET,\infty} = 1) \qquad (1.7)$$

in particular depend on the selected k_0 and k_∞. There are several reasons for the appearance of the F broadening factors in eqn. 1.5. First, the excited species AB* in the Energy-Transfer mechanism are formed over a wide range of energies E and angular momentum (quantum number J). The second reason is the multistep character of the reactions (R.2), (R.3) and (R.4).

1.2   Radical-Complex (RC) mechanism

Experimental measurements of atom and radical combination rates have indicated that the behavior is consistent with the predictions based on the Energy-Transfer mechanism, but that sometimes the observed rates are much higher. For example, Porter[16] found that the combination rate constant of iodine atoms with argon as chaperon at 27°C is 3.0×10^9 dm^6 mol^{-2} s^{-1}, and it was proven that this value has the right order of magnitude to be explained by the ET mechanism.[17] On the other hand, with benzene as chaperon, the rate constant is about 30 times higher than the calculated value by Laidler.[17] Also, some atmospheric association

reactions have been postulated to follow a different mechanism. To explain such discrepancies, a different mechanism, the Radical-Complex (RC) mechanism, originally postulated as the "chaperon mechanism" of atom recombination,[16,18] was suggested. The radical-complex mechanism can be formulated symbolically in terms of the steps :

A	+	M	$\rightarrow$	AM			k_a, K_A	(R.5)
	AM		$\rightarrow$	A	+	M	$k_{-a,}$	(R.6)
B	+	M	$\rightarrow$	BM			k_b, K_B	(R.7)
	BM		$\rightarrow$	B	+	M	k_{-b}	(R.8)
AM	+	B	$\rightarrow$	AB	+	M	k_{AM+B}	(R.9)
BM	+	A	$\rightarrow$	AB	+	M	k_{BM+A}	(R.10)
AM	+	BM	$\rightarrow$	AB	+	2M	k_{AM+BM}	(R.11)
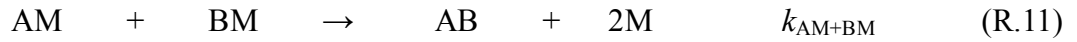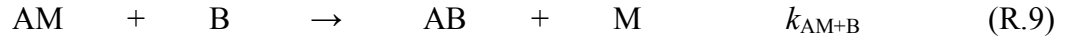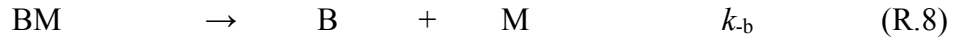
The competing intermolecular-complex mechanism may play an important role and the atom or radical may form a complex with the third-body particles in the RC mechanism. The stabilization of the energized adduct (AB*) takes place not via energy transfer to the bath gas but via the dissociation of the formed van der Waals complexes. These reaction steps lead to a rate coefficient in the form:

$$k_{RC,rec} = \frac{(K_A k_{AM+A} + K_B k_{BM+A})[M] + K_A K_B k_{AM+BM}[M]^2}{1 + (K_A + K_B)[M] + K_A K_B [M]^2}$$

(1.8)

Similar to the ET mechanism, it is shown that at very low pressures the first–order rate constant increases linearly with the bath gas concentration and at very high pressures it becomes pressure–independent.

$$k_{RC,0} = (K_A k_{AM+B} + K_B k_{BM+A})\,[M] \quad = \quad k_0[M]$$

(1.9)

$$k_{RC,\infty} \quad = \quad k_{AM+BM} \quad = \quad k_\infty$$

(1.10)

Figure 1.6 shows the schematic representation of the Radical-Complex mechanism.
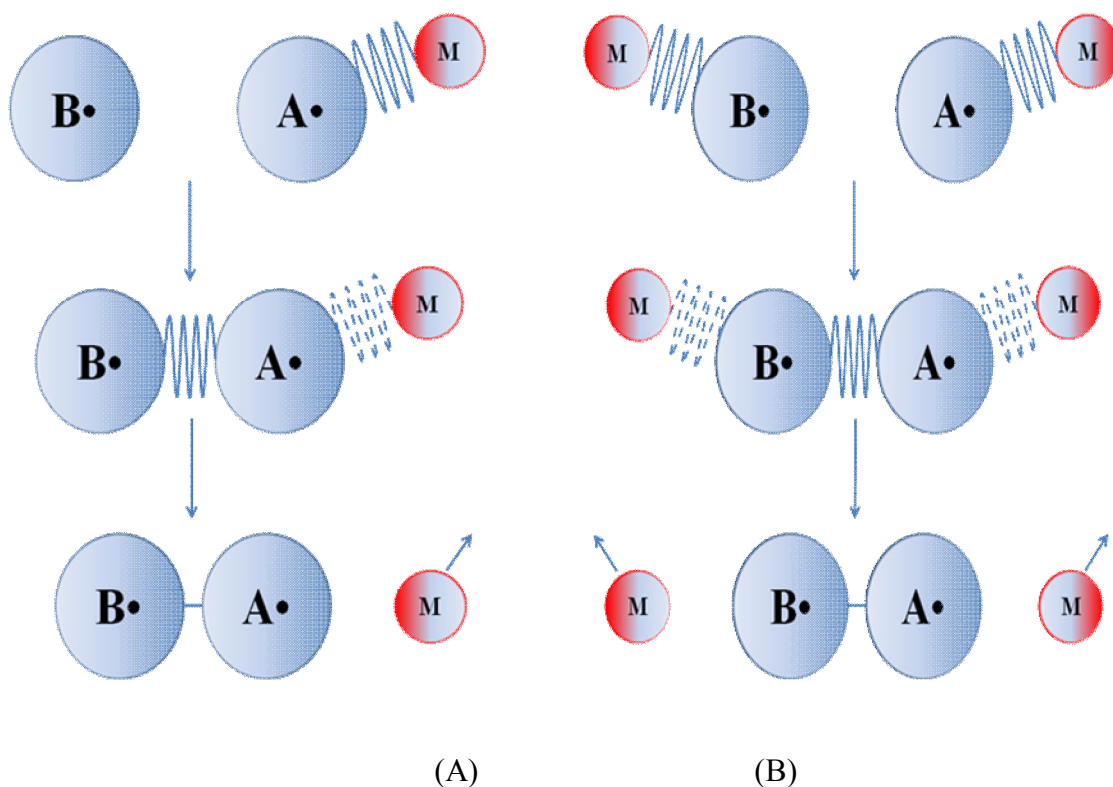
Figure 1.6 Schematic representation of the Radical-Complex (RC) mechanism. (a) AM + B step, (b) AM + BM step.

Earlier Bunker and Davidson[19] suggested an expression for K_{eq} for the complexation of a radical (A) with a solvent molecule (M) as

$$K_{eq} / \sigma_{LJ}^3 = \pi^{1/2} (\varepsilon_{LJ} / k_B T)^{3/2} \left(\frac{8}{3} + \frac{32 \cdot \varepsilon_{LJ}}{45 \cdot k_B T} \right)$$ (1.11)

with the Lennard-Jones diameter σ_{LJ} and the well-depth ε_{LJ} in the van der Waals type interaction between radical (A) and solvent molecule (M), where T is the temperature and k_B Boltzmann's constant. However, in this case, dimers which are in metastable states, *i.e.* at energies higher than the binding energy but below the centrifugal barrier, are not considered. This leads to errors of K_{eq} especially at high temperatures. As a result, a factor of 2 is missing. K_{eq} is evaluated with a modified expression suggested by Schwarzer and Teubner,[20] who calculated K_{eq} by decomposing the gas-phase radial distribution function into contributions arising from bound states and from scattering collisions:

9

$$K_{eq} = \frac{4\pi \int r^2 [g(r) - g_{scattering}(r)] dr}{1 - [M] 4\pi \int r^2 [g(r) - g_{scattering}(r)] dr} \qquad (1.12)$$

where g(r) is the radial distribution function, $g_{scattering}(r)$ the part of $g(r)$ from the scattering collision, and [M] the concentration of the third body. The condition, [AM] $\ll$ [A], should be fulfilled to use this equation.

The calculated equilibrium constants from expression (1.12) are usually in the range 10^{-22}–10^{-23} cm^3 under our experimental conditions. The most characteristic feature of the Radical-Complex mechanism comes from the strong negative temperature dependence of the equilibrium constant. An example of such a tendency is shown in Figure 1.7 for benzyl radicals.
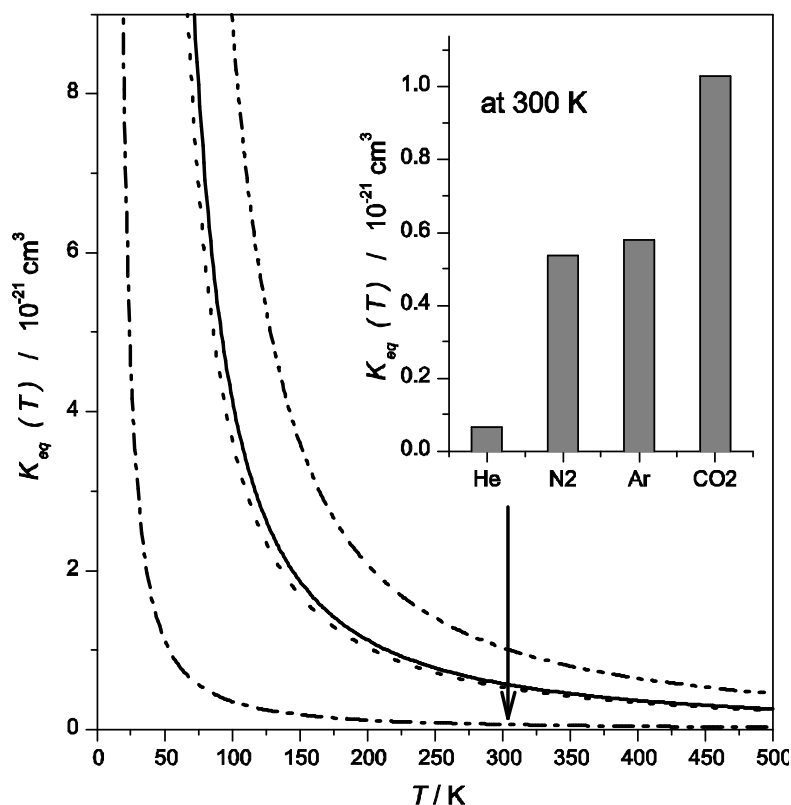
Figure 1.7 Temperature dependence of the equilibrium constant K_{eq}(T) for complexation of benzyl radicals with different solvent molecules, He (dash-dotted), N_2 (dotted), Ar (solid) and CO_2 (dash-dot-dotted). Inset: Equilibrium constant K_{eq} at 300 K for different bath gases. The figure was taken from ref. 12.

From the equilibrium constant, the degree of complexation (κ),

$$\kappa = \frac{[AM]}{[A]+[AM]} = 1 - \frac{1}{K_{eq}\left(T, \varepsilon_{AM}, \sigma_{AM}\right) \cdot [M] + 1} \qquad (1.13)$$

is calculated as a function of the interaction with the bath gas (M) and of temperature. Figure 1.8 shows an example of the density-dependent degree of complexation of benzyl radicals with 4 different bath gases. The degree of complexation is increasing at higher densities and with increasing strength of the radical-solvent molecule interaction, He $<$ N$_2$ $\approx$ Ar $<$ CO$_2$. Therefore, a pronounced growth of the concentration of complexed radicals at higher densities and at lower temperatures is expected.
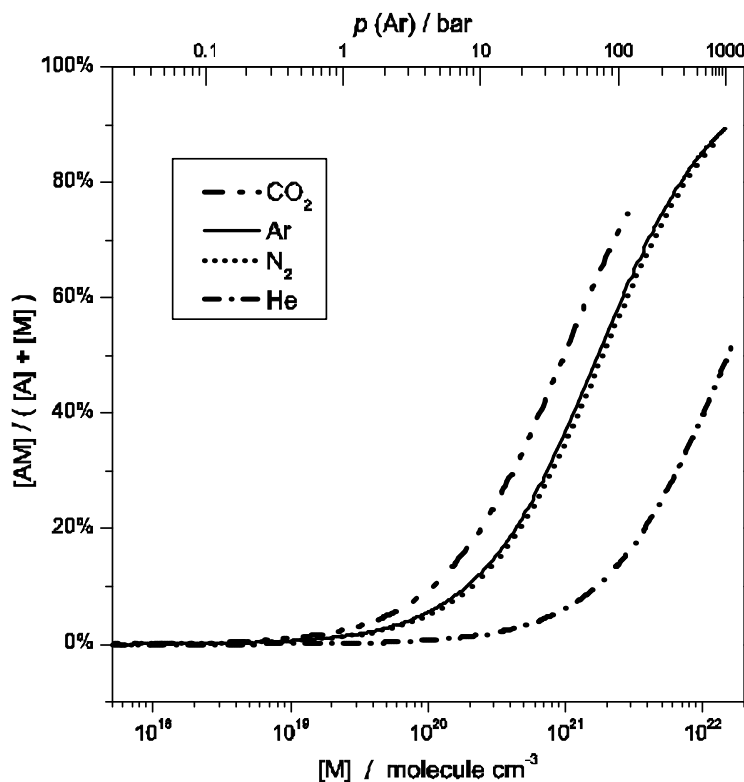
Figure 1.8   Density dependence of the degree of complexation of benzyl radicals with different solvent molecules, He, N$_2$, Ar and CO$_2$ at 300 K. The corresponding pressure scale for Ar is shown on the top axis as a reference. The figure was taken from ref. 12.

1.3 Combination of ET and RC mechanisms

The total radical combination rate constant can be expressed by the combined form of the Energy-Transfer and Radical-Complex mechanisms. As the recombination rate constant is strongly affected by the individual mechanisms, the rate constant depends on the rate constants of the elementary reactions and the equilibrium constant.

A general reaction pattern for the geminal recombination of the free radical A can be set up, which contains both mechanisms :

$$A \quad + \quad A \quad \rightleftarrows \quad A_2^* \qquad\qquad\qquad k_c, k_{-c} \qquad (R.12)$$

$$A_2^* \quad + \quad M \quad \rightarrow \quad A_2 \quad + \quad M \qquad k_d \qquad (R.13)$$

$$A \quad + \quad M \quad \rightleftarrows \quad AM \qquad\qquad k_e, k_{-e}, K_{eq} \qquad (R.14)$$

$$AM \quad + \quad A \quad \rightarrow \quad A_2 \quad + \quad M \qquad k_{AM+A} \qquad (R.15)$$

$$AM \quad + \quad AM \quad \rightarrow \quad A_2 \quad + \quad 2M \qquad k_{AM+AM} \qquad (R.16)$$
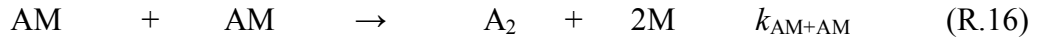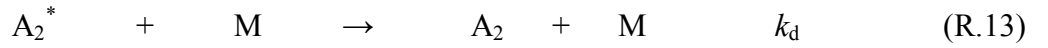
The two mechanisms mentioned form a system of parallel reactions, so that the total rate constant is computed as the sum of the single rate constants of each mechanism,

$$k_{rec} \quad = \quad k_{ET,rec} \quad + \quad k_{RC,rec} \qquad (1.13)$$

The total rate constant is then given by

$$k_{rec} = \frac{k_{ET,\infty} k_{ET,0}[M]}{k_{ET,\infty} + k_{ET,0}[M]} F_{cent} + \frac{K_{eq} k_{AM+A}[M] + K_{eq}^2 k_{AM+AM}[M]^2}{(1 + K_{eq}[M])^2} \qquad (1.14)$$

There have been extensive experimental studies on combination reactions of atoms and small radicals (for example, refs. 1-6), in which indications for an involvement of the Radical-complex mechanism were found; however, a separation of the contributions from various mechanisms was always difficult. Figure 1.9 (A) illustrates the density dependence of radical combination rate constants (k_{rec}) which can be the sum of the Energy-Transfer and Radical-Complex mechanisms. In this case, at low densities, we assume that radicals are much less

complexed and therefore the ET mechanism dominates (this is however not always the case, for example, in the ozone recombination reaction at low temperatures, one can expect a more pronounced contribution of the RC mechanism than that of the ET mechanism to the limiting low-pressure rate constant $(k_0)^{1,21}$). Considering "general" cases, at higher densities where radicals are expected to be more complexed with solvent molecules, the contributions of the Radical-Complex mechanism can dominate, resulting in an S-shape fall-off curve for the sum of the two mechanisms.
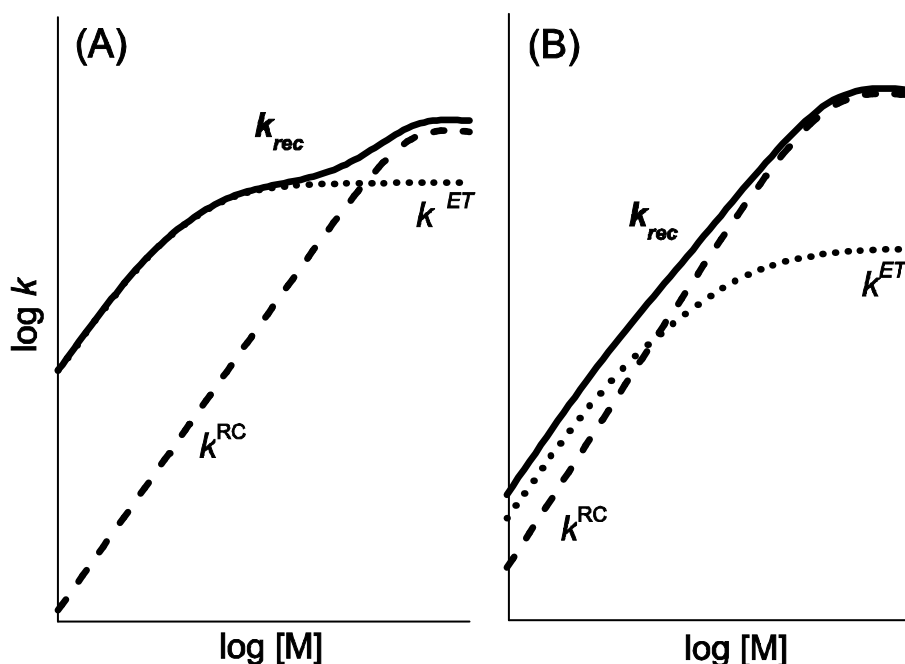
Figure 1.9 Simple illustrations of density dependence of recombination rate constants (k_{rec}) in terms of the sum of the Energy-Transfer (ET) and Radical-Complex (RC) mechanisms. The figure was taken from ref. 12.

It is often the case that the resulting fall-off curve of radical combination rate constants resembles a smooth shape, such that one cannot tell from the shape only if there is indeed an additional contribution from the RC mechanism. Figure 1.9 (B) illustrates such an example. Especially, this happens when the reaction reaches the limiting high-pressure rate constant of the ET mechanism (k_∞^{ET}) at very high densities where the RC mechanism starts playing a considerable role. Therefore, a smooth fall-off curve does not guarantee the absence of the RC mechanism.

1.4 Diffusion-controlled kinetics

Even at relatively low pressures, recombination reaction rate constants for large molecules are already essentially determined by the limiting high-pressure rate constant of the ET mechanism, which is independent of the bath gas density. But with increasing pressure, it must be considered that the diffusion-controlled kinetics of the radicals in the bath gas can play an additional role. The larger viscosity of the gas mixture increases the time interval between two impacts, so that diffusion becomes the rate-determining factor.

An expression for the rate constant of diffusion-controlled kinetics, k_{diff}, is given by the Smoluchowski relationship:

$$k_{diff} = 4\pi\alpha_{spin}(M)\ RD \tag{1.15}$$

where D is the diffusion coefficient of the recombining molecules in the bath medium and α_{spin} is the electronic weight ("spin statistical") factor. R is the effective capture distance. In the gas-to-liquid transition range, the combination rate constant k_{obs} traditionally has been approximated by the relationship[22]

$$k_{obs} = \frac{k_{rec}k_{diff}}{k_{rec} + k_{diff}} \tag{1.16}$$

1.5 Reaction systems studied in this thesis

The reason for the unexpected temperature- and pressure-dependent enhancement of combination rates at high pressures has not yet been clearly understood. This results from the difficulty in separating the contributions of the RC mechanism from those of the ET mechanism. Both ET and RC mechanisms yield a similar shape of the fall-off curve and therefore one obtains always the sum of two fall-off curves. As illustrated in Figure 1.9, the distinct difference may not be easily identified, especially if the limiting high-pressure rate constant of the ET mechanism is reached at higher pressures where the RC mechanism already sets on. For example, in the case of the ozone recombination,[1] even though the increase of rate constant was observed, it was difficult to separate the contribution of each mechanism because both mechanisms contribute to the increase until diffusion starts to

influence the rate constant. Therefore, the need to separate and clarify qualitatively and quantitatively the contribution of the RC mechanism to the radical combination kinetics in the gas-to-liquid transition region is urgently required to explain such an unexpected increase of recombination rate constants.

A successful experimental strategy was suggested to tackle this problem.[9] This is schematically represented in Figure. 1.10.
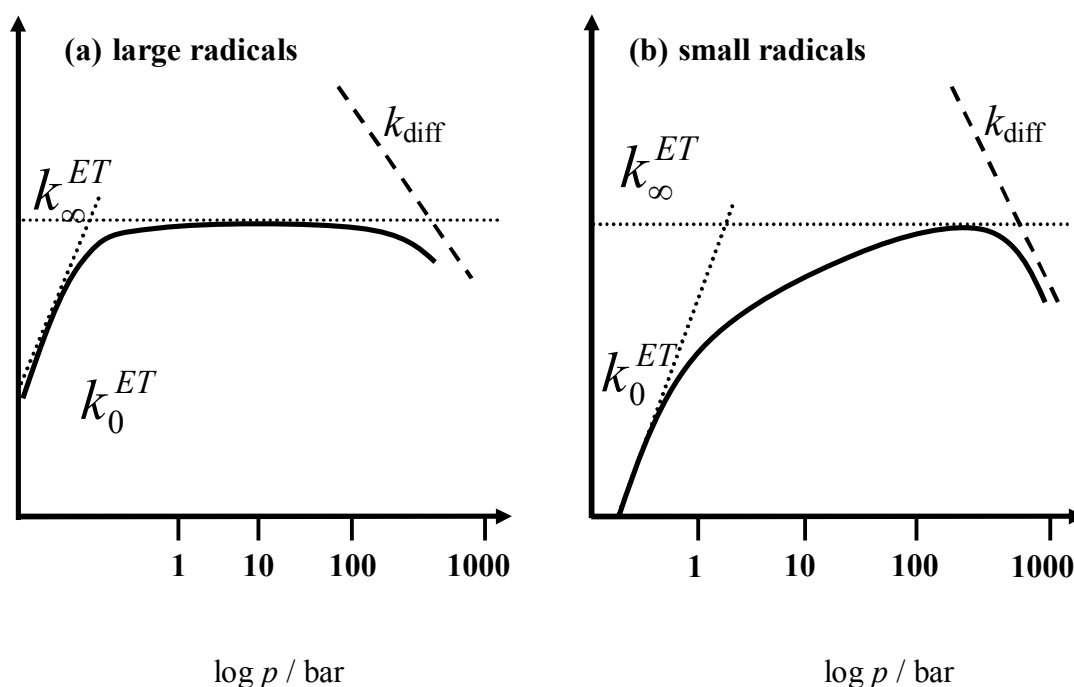
Figure 1.10 Schematic representation of limiting cases. (a) Combined reaction rate constant k_1 for large radicals and (b) for small radicals.

In the first step, a system, in which the limiting high-pressure rate constant of the ET mechanism is reached at relatively low pressure, is selected. It should be noted that the contribution of the RC mechanism at the "low" pressure region is expected to be negligible. In ref. 9, the limiting "high-pressure" rate constant of the ET mechanism is established far below 1 bar (case (a) in Figure 1.10). In the second step, the pressure is then increased up to the conditions where the RC mechanism may become visible. At this stage the additional enhancement of the combination rate constant will be completely due to the contribution of the RC mechanism. Several atom combination reactions, like iodine, have been investigated

and a higher value of the rate constant than the value calculated from the ET mechanism observed. But as atom and small radical recombination reactions belong to case (b) in Figure 1.10, it was difficult to separate the contribution of the RC mechanism. On the other hand, large radicals such as benzyl and *p*-fluorobenzyl radical, belong to case (a).

Oum *et al.*[9] selected the benzyl radical as target radical and investigated the contribution of the RC mechanism to the increase of the combination rate constant. In the present thesis, we also selected the benzyl radical as the target system and investigated the temperature and pressure dependence of the recombination rate constant in the bath gases (M) CF_3H, CF_4 and SF_6.

$$C_6H_5CH_2 \quad + \quad C_6H_5CH_2 \, (+M) \quad \rightarrow \quad C_{14}H_{14} \, (+M) \qquad \qquad (R.17)$$
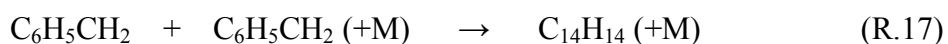
The benzyl radical is a prototype aromatic free radical and an important intermediate in various chemical reactive systems involving toluene; for example, at room temperature, it is formed in a preliminary step of the tropospheric oxidation mechanism of toluene initiated by OH radicals.[23] Subsequent reactions with O_2 and possibly with NO_2 in polluted urban atmospheres are responsible for the observed final oxidation products.[23] Benzyl is also an important species in high-temperature processes involving toluene, such as pyrolysis or combustion.[24-26] The spectroscopic characteristics of the benzyl radical have been studied both in the gas-phase and in the condensed phase. In addition to such important properties of benzyl radicals, pressures below 1 bar are required for approaching the high-pressure limit and truly constant k_∞^{ET} are measured over a broad density range before the additional pressure dependence of the rate constant is observed. Therefore, the benzyl radical is a suitable species to separate and investigate the contribution of the RC mechanism to the combination reaction constants.

In addition to benzyl radicals, several recombination reactions of benzyl-type radicals were studied in a systematic variation of the effect of the steric hindrance around the newly forming bond and functional groups which can influence the rotation of the radical. The recombination reactions of *p*-fluorobenzyl radicals and *p*-methylbenzyl radicals were investigated to see if the enhancement of recombination rate constants at high pressures can also be found in these systems.

p-Fluorobenzyl radical:

$$p\text{-F-C}_6\text{H}_4\text{CH}_2 \quad + \quad p\text{-F-C}_6\text{H}_4\text{CH}_2 \quad (+M) \quad \rightarrow \quad C_{14}H_{12}F_2 \ (+M) \qquad (R.18)$$

p-Methylbenzyl radical:

$$p\text{-CH}_3\text{-C}_6\text{H}_4\text{CH}_2 \quad + \quad p\text{-CH}_3\text{-C}_6\text{H}_4\text{CH}_2 \ (+M) \quad \rightarrow \quad C_{16}H_{18} \ (+M) \qquad (R.19)$$
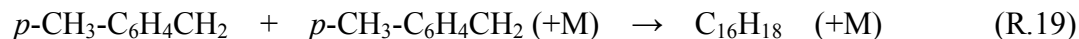
Helium, argon, N_2, and CO_2 were employed as bath gases to investigate the effect of different properties of the solvent molecules, such as dipole moment, polarizability, mass, etc. Furthermore, we employed a mixture of He and CO_2 as bath gas to investigate the preferential local composition effect in the RC mechanism.

In addition, the transient UV absorption spectra of *p*-fluorobenzyl radicals and *p*-methylbenzyl radicals were investigated, because no direct studies of the absorption band of these radicals in the UV region are available. The absorption coefficient of each radical and its temperature dependence were determined over the range 300–450 K.

In the following sections, the details of these studies are described. We focus on the view of the role of radical complexes in the radical combination reactions, consistently observed throughout several reaction systems tested here.

Chapter 2

Experimental set-up

This chapter describes the equipment, instrumental set-up, and methodology that were used for the measurement of recombination rate constants for benzyl, *p*-fluorobenzyl and *p*-methylbenzyl radicals over the pressure range 1–700 bar and the temperature range 300–520 K in different bath gases.

2.1. Laser system

2.1.1. Excimer laser

The target radicals (benzyl, *p*-fluorobenzyl and *p*-methylbenzyl radicals) were generated through a series of reaction steps. Laser flash photolysis of Cl_2, and subsequent H-atom abstraction reactions by the photolytically produced Cl atom are involved in these steps. A 308 nm XeCl excimer laser (Lambda Physik, model COMPEX) with a ca. 15 ns pulse length and pulse energies of ca. 200 mJ was used as excitation source. The laser was externally triggered by a TTL-pulse (11 V intensity, 5 μs pulse width). A pulse / delay generator (Stanford Research Systems, model DG 535/02) was interfaced with the laser controlling system. First, the TTL-pulse with 5 μs width and 1.1 V intensity was prepared, which was then amplified to 11 V using the pulse / delay generator.

The laser energy was measured behind the optical cell with a piezoelectric detector. The measured laser energy of each pulse was monitored by an oscilloscope and recorded in the computer.

2.1.2. Generation of radicals

The radicals were generated by laser photolysis of Cl_2 at 308 nm and the subsequent fast bimolecular reaction of chlorine atoms with an excess amount of precursors. Toluene (C_6H_5-CH_3), *p*-fluorotoluene (*p*-F-C_6H_4-CH_3) and *p*-xylene (*p*-CH_3-C_6H_4-CH_3) were used as precursors for benzyl, *p*-fluorobenzyl and *p*-methylbenzyl radicals, respectively:

$$Cl_2 \quad + \quad h\nu \quad \rightarrow \quad 2\ Cl \qquad\qquad (R\ 2.1)$$

$$Cl \quad + \quad C_6H_5CH_3 \quad \rightarrow \quad C_6H_5CH_2 \quad + \quad HCl \qquad (R\ 2.2)$$

The reaction rate constant for reaction 2.2 is known to be $k = 6.1 \times 10^{-11}$ cm^3 molecule^{-1} s^{-1}. The use of an excess amount of precursors ensured that chlorine atoms were instantly and stoichiometrically converted to benzyl radicals.[27]

2.2. The optical flow cells

Two slightly different types of optical flow cell for high-pressure measurements and one glass-cell for low-pressure (below 1 bar) experiments were used in the present work for different experimental conditions. One of the high-pressure optical flow cells which can be cooled or heated over the temperature range 200 – 420 K at pressures of 1 – 1000 bar. The other cell can be heated up to 600 K at pressure of 1 – 1000 bar but cannot be cooled. The cell used for experiments below 1 bar was a glass flow cell. Both high-pressure cells and the glass cell were designed for laser flash photolysis experiments and are described in detail below.

2.2.1. The coolable and heatable high-pressure optical flow cell

The cell was made of stainless steel (RGT 601) and the schematic diagram of the cell is shown in Figure 2.1. The cell has a path length of 10 cm and an optical diameter of 0.9 cm. As shown in Figure 2.1, an additional cooling or heating jacket was used. The desired temperature conditions were achieved by simply exchanging the jacket.

The temperature was measured by two platinum resistance thermometers (Pt-100), which have high accuracy, fast response, and a wide measurable range of temperatures (70 –1000 K).

They were directly attached to the front and back of the cell. The homogeneity of the temperature within the cell was monitored by the temperature difference between the two Pt-100s.
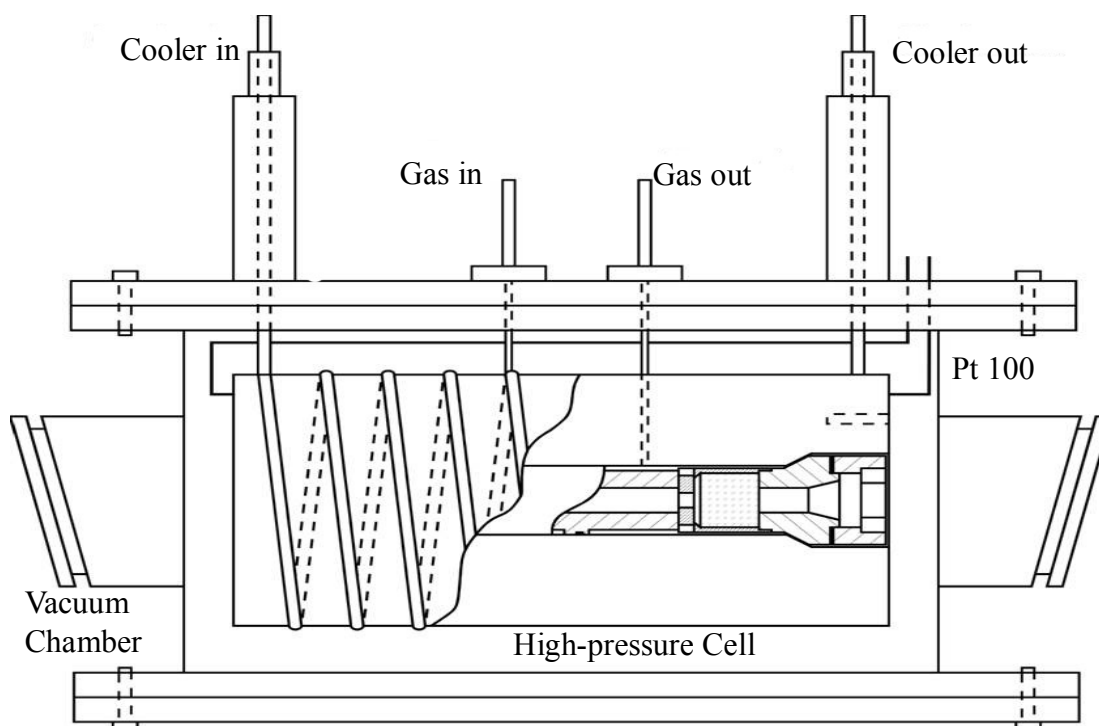
Figure 2.1   Schematic representation of the coolable and heatable optical high-pressure cell, ref. 6.

Temperatures above 300 K

The heating jacket (inner diameter 9.5 cm, thickness 0.5 cm) was introduced to reach high temperature experimental conditions. Approximately 3 m of heating wire with a resistance of 100 Ω were assembled on the heating jacket and the temperature was controlled by a controller Newtronic Micro 96.

Temperatures below 300 K

Temperatures below 300 K were achieved by flowing acetone cooled by liquid N_2 through the

cooling jacket. A coaxial copper capillary (approximately 3 m, diameter 6 mm, wall thickness 0.5 mm) was attached to the jacket through which the cooled acetone was pumped. The cooling system is shown in Figure. 2.2.
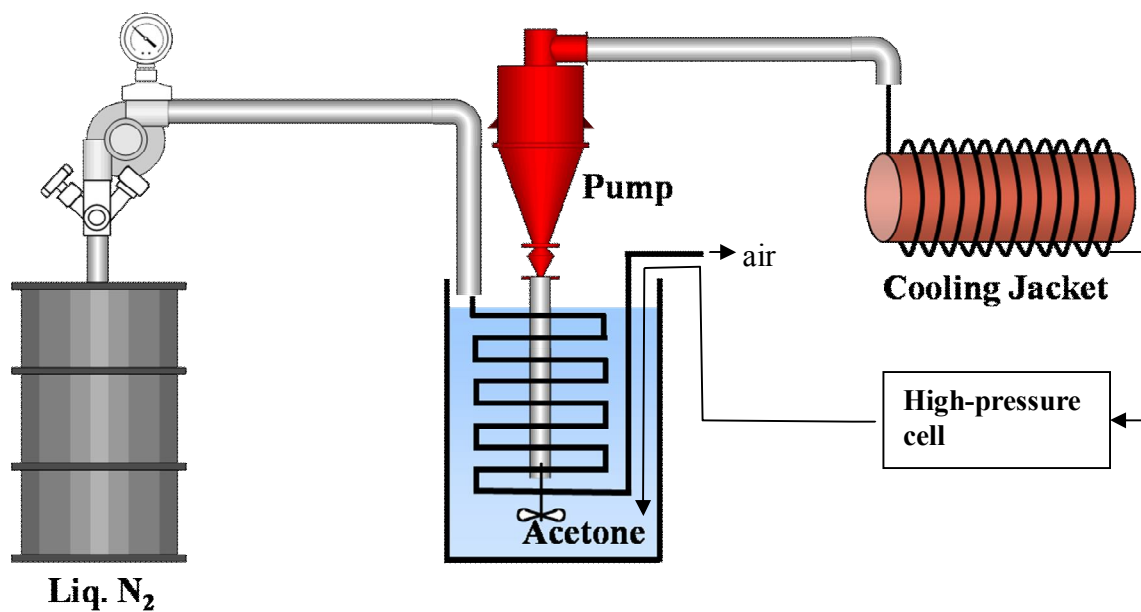
Figure 2.2 Schematic representation of the cooling system.[6]

As the freezing point of acetone is 179 K, it is a suitable cooling solvent for low temperature experiments down to 200 K. If an even lower temperature is required, isopentane (freezing point 113.4 K) can be used instead of acetone.

When low temperature experiments are conducted, the humidity in the air would condense on the surface of the windows, making it impossible for the lamp and laser light to pass through the cell. To prevent condensation, a vacuum chamber, which can house the high pressure cell, was employed. The windows of the vacuum chamber were made of magnesium fluoride and tilted by 20° to prevent back reflections of the laser. This configuration allows the cell to be heated up to 420 K and cooled down to 200 K at pressures up to 1000 bar.

2.2.2. High pressure and high temperature optical flow cell

Since a much higher temperature than 400 K is required to fully investigate the temperature dependence of the radical complex mechanism, a high-pressure and high-temperature optical flow cell was used. The cell is shown in Figure. 2.3.
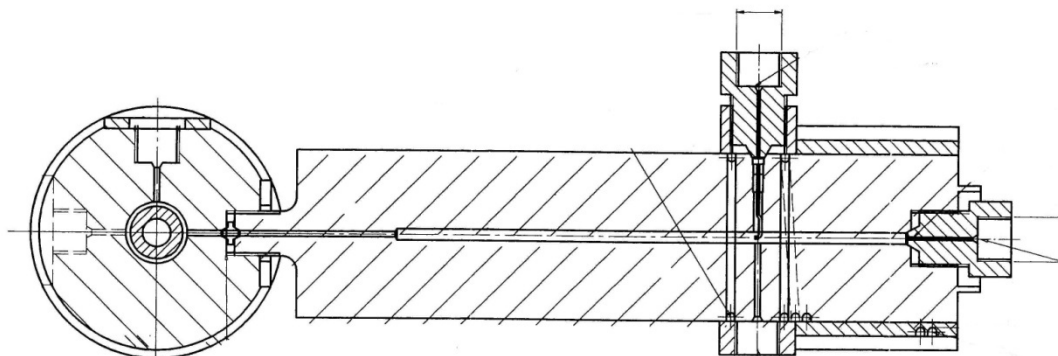
Figure 2.3   Schematic representation of the high-pressure and high-temperature cell.[12]

The optical windows were sealed applying a modification of the Bridgeman-Poulter-principle.[28-30] The Bridgeman-Poulter-principle is based on the fact that windows on the sealing surfaces of the stamp are pressed by the internal pressure, which prevails in the cell. In addition, the cell must be cleaned by evacuating volatile impurities. For this reason, the original sealing method was modified. Using caps made of high-grade steel, which were put over the windows and screwed onto the stamp, the windows were pressed in slightly against the sealing surfaces, so that they kept the cell closed. The conical stamp (angle 37.5°) was pressed by a screw against the cone (angle 39°) in the cell. Due to the different angle between stamp and cone in the cell, the sealing could be achieved.

The cell had a path length of 4 cm and an optical diameter of 1 cm. Instead of using a heating jacket, heating wires were directly attached both on the main and preheating cell bodies. The target temperature was derived from the preheating section, directly connected to the main cell. The gas mixture was preheated as it flowed through about 2 m of high-pressure tubing in the preheating section. Two Ni-Cr-Ni type thermoelements were directly inserted to measure the temperature. One was on the main cell body and the other on the preheating

section. Based on the temperature from the two thermoelements, the temperature was registered by a temperature controller (Eurotherm Type 2408) with an accuracy of 0.1 K. This configuration allowed the cell to be heated above 600 K and pressurized up to 700 bar.

2.2.3. Preheating cell

As described in the experimental part, all measurements have been carried out in a flow-type high-pressure cell. For measurements in CO_2 above 50 bar, it was necessary to flow mixtures of Cl_2, toluene, and CO_2 via a preheating cell, before they entered a membrane-type high-pressure compressor. By doing so, one could keep CO_2 in the supercritical state on compression. Since the density of liquid CO_2 is much higher than that of supercritical CO_2, it is less dangerous to handle the high-pressure system at the supercritical state of CO_2 than that of liquid CO_2 in the case that an unexpected leakage appears in the set up. The typical temperature, 323 K, of the preheating cell was controlled by a water heating / cooling jacket. The temperature of the water was kept constant by a thermostat (Lauda).
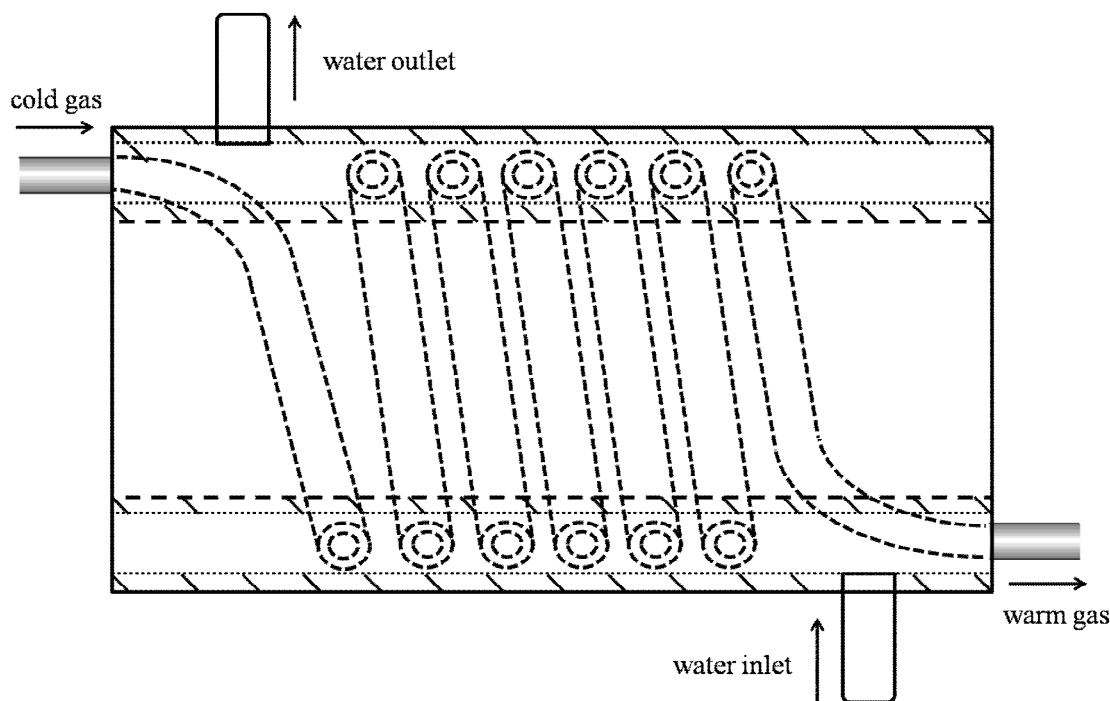
Figure 2.4   Schematic representation of the preheating cell.[31]

To prevent cooling down of the CO_2 behind the preheating cell, the compressor was heated up to 310 K, and the temperature was measured just after the preheating cell and in the outlet part of the compressor (Nova Swiss, Model 2122). Figure 2.4 shows the schematic diagram of the preheating cell, used in the high-pressure CO_2 experiments.

2.2.4. Low pressure (< 1 bar) optical flow cell

To determine the high-pressure limit of the rate constant in the energy-transfer mechanism, $k_{1,\infty}^{ET}$, for experiments below 1 bar, an existing flow cell made of glass was used. This glass cell had an optical path length of 52 cm and an optical diameter of 3 cm. Basically, the signal intensity was proportional to the concentration of Cl_2. As the concentration of Cl_2 was low for the experiments < 1 bar, the optical path length was increased to improve the signal intensity. Quartz windows were used, and the windows were tilted at Brewster's angle. The evacuation of the glass cell to reach pressures below 1 bar was performed using a rotary vacuum pump. The target pressure was achieved by controlling two needle valves, one before the inlet and the other one behind the outlet of the cell.

2.3. Flow system

The high-pressure capillary, which can hold high pressures up to 4000 bar (Nova Swiss, TBG 60 – 4, 1/4" outer diameter, 3/32" inner diameter), was used in the high-pressure section (from the compressor outlet to high-pressure cell outlet). Also, all components such as valves, unions, and reducers could withstand up to at least 1000 bar (Nova Swiss). On the other hand, standard 6 mm OD tubing (Swagelok) connected the sample vessel to the compressor, because the maximum pressure was less than 200 bar in this section. For experiments below 100 bar, a high pressure gas mixture was connected directly to the high-pressure optical cell without a compressor. Typically, gas mixtures with a pressure 20 bar above the highest pressure needed were prepared and used under flow condition for the experiments conducted without compression. The pressure inside the cell was controlled by two high-pressure micro-metering valves (Nova Swiss, Model 530.6131).
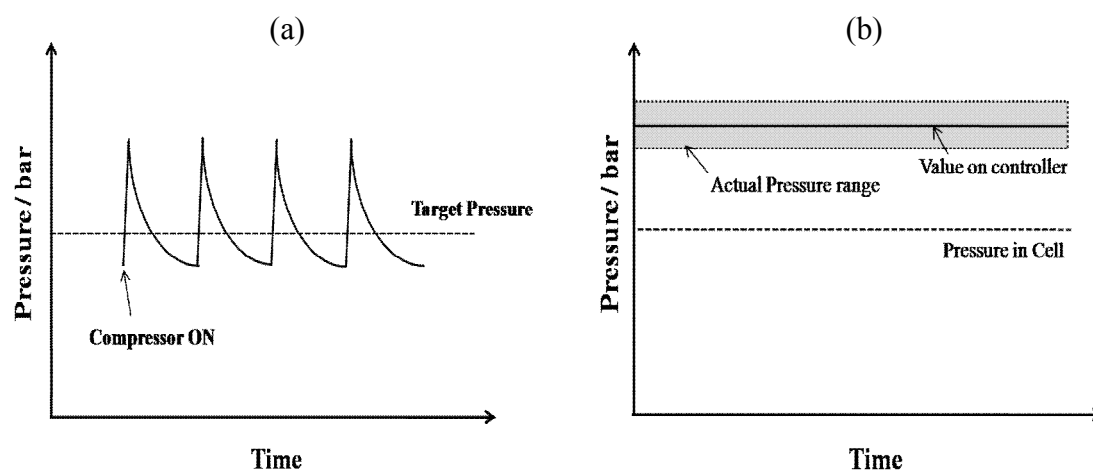
Figure 2.5 Schematic representation of the "continuous compressing method".
(a) Normal compressing process, (b) continuous compressing method.

The total pressure of the system was measured with high-pressure meters (Burster, Model 8201, 0–10 / 200/ 1000 bar), connected directly to the cell. Compressed mixtures of Cl_2, radical precursor molecules, and bath gas were flowed through the high-pressure cell by an oil-free diaphragm compressor (Nova Swiss, 554.2122). As the pressure variation can be more than ± 20 bar during the measurement when the compressor is used, it is hard to maintain a constant pressure in the optical high pressure cell. This problem is sketched in Figure 2.5 (a).

The so-called "continuous compressing method", was introduced to overcome this problem. The method is quite simple and very efficient. The target pressure on the compressor controller was set higher than the pressure needed in the cell, and the actual pressure inside the high-pressure cell was independently controlled by using two high-pressure micro metering valves. This guarantees a constant pressure (± 5 bar) and flow rate during the experiment. This method is also described in Figure 2.5.

One of the important experimental factors is the flow rate. Since the reagents and products were removed from the observation volume between consecutive laser pulses, possible side reactions initiated by multiple photolysis could be prevented. This was accomplished through the use of micro-metering valves. The pressure could be adjusted by 0.1 bar, and the flow-rate by 0.1 L min^{-1}. Flow-meters (Tylan FM 3911 0–30 SLM, FM 3921 0–300 SLM) were used to monitor the flow-rate.

2.4. The optical detection system

The complete optical set-up is shown in Figure 2.6.
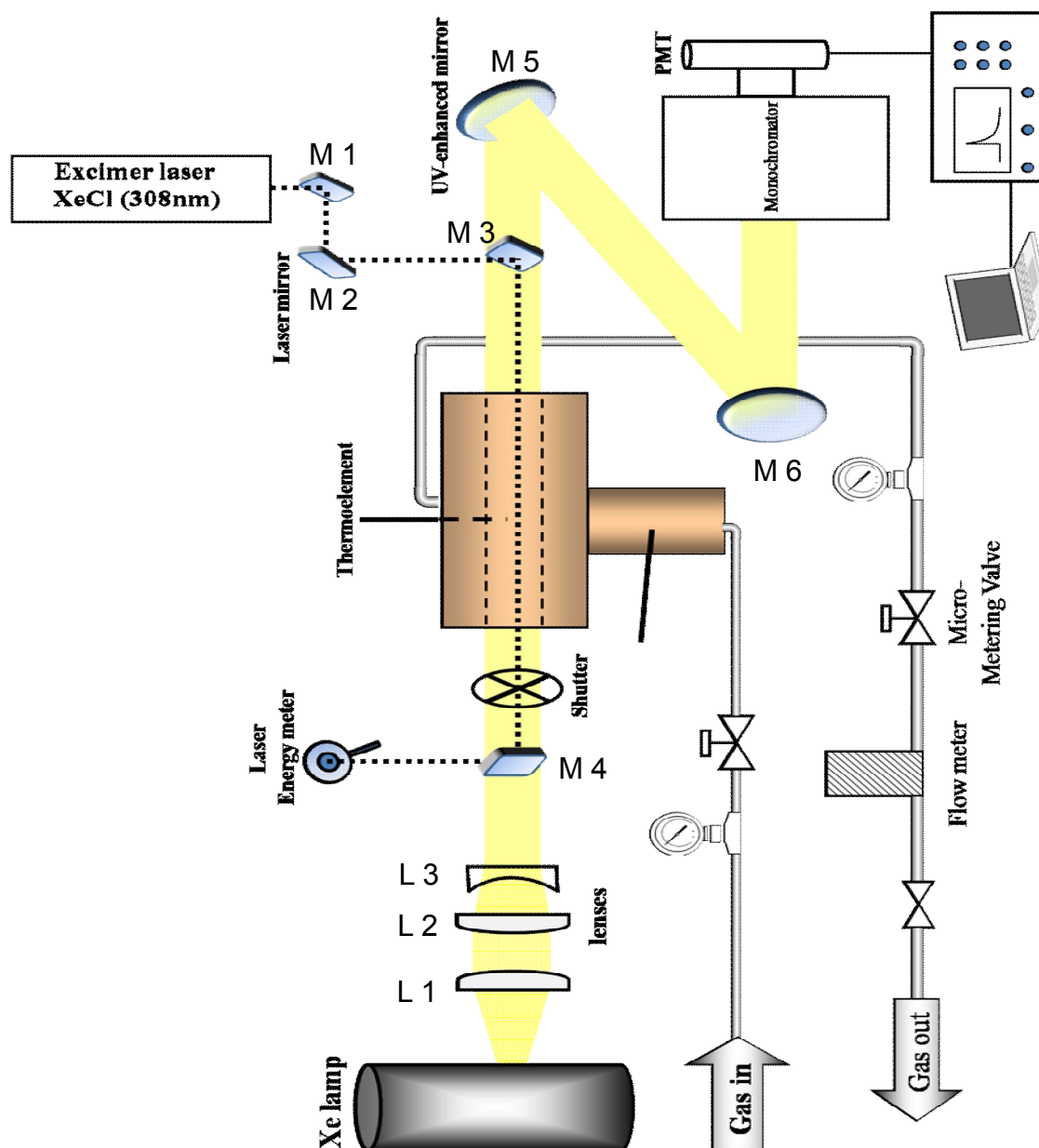
Figure 2.6 Schematic representation of the experimental optical set-up.

M1, M2, M3 and M4 were high-reflectance (HR) 308 nm laser mirrors and M5 and M6 were aluminum-coated UV enhanced mirrors. Figure 2.7 shows the transmittance curve of the HR 308 nm mirror.
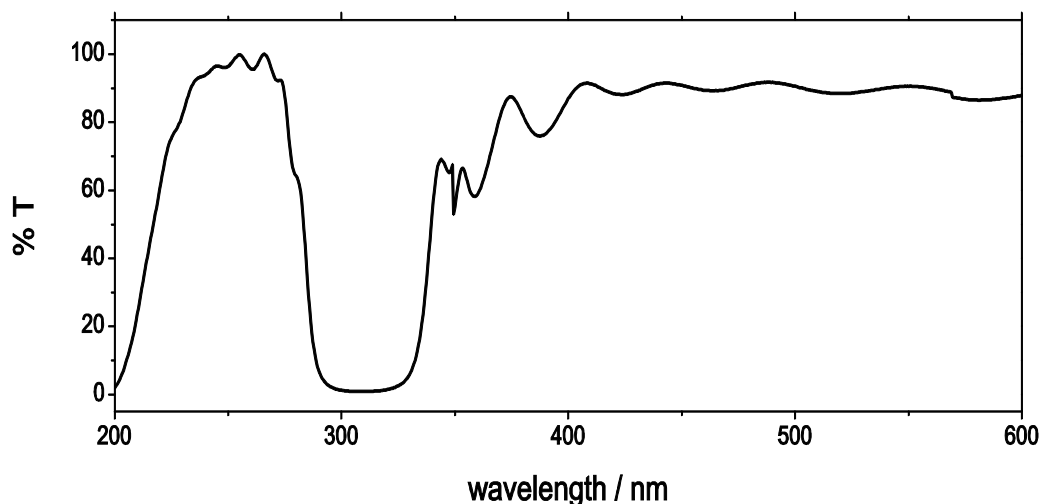
Figure 2.7   Transmittance curve of the HR 308 nm laser mirror.

2.4.1. Laser flash photolysis method

The use of the flash photolysis technique dates back to the late 1940s in the pioneering work of Norrish and Porter in Cambridge[32,33]. Flash photolysis is a commonly used technique for monitoring fast photochemical reactions. The basis of the technique is simple: Reactants and precursors are premixed and flow into the photolysis cell at the required pressure. A pulse of light is used to produce a transient species, an atom radical or excited state, whose concentration is then monitored as a function of time.

The advantages of the laser flash photolysis technique in the investigations of elementary reactions in gas phase are due to the following reasons:

I.   No mixing time is required, in contrast to e.g. stop-flow methods.

II. Temperature and pressure can be varied over a wide range.

III. Complications from wall-catalyzed reactions are minimized.

For reactions at a moderate rate, flash lamps provide sufficient time response. As the limitation on the timescales of reactions which can be studied is the duration of the light pulse,

pulsed xenon lamps are not suitable for very fast reactions. In general the pulse width of the light source must be much shorter than the half-life of the chemical reaction. Whilst lamps are still employed, the majority of flash photolysis experiments are now conducted with lasers. For faster reactions, lasers must be used that have pulse widths in the nanosecond range. Using ultrafast pulsed lasers allows processes in the sub-picosecond time scale to be studied. The excimer laser is particularly widely employed due to useful properties such as a pulse duration of ca.15 ns, repetition rates of up to 500 Hz and high pulse energies. In the present work, a XeCl excimer laser was employed to photolyze Cl_2. Kinetic absorption spectroscopy is an ideal method for fast reactions. The absorption signal of the reactant radical generated by the lamp or laser will increase instantaneously, and then decay as the radical reacts. Concentration and absorption are related via the Beer-Lambert Law

$$I = I_0 \exp(-\sigma c l) \tag{2.3}$$

where I is the measured change in light intensity, I_0 the intensity before the photolysis pulse, σ is the absorption coefficient, c the reactant concentration, and l is the optical path length. A schematic signal is shown in Figure 2.8.
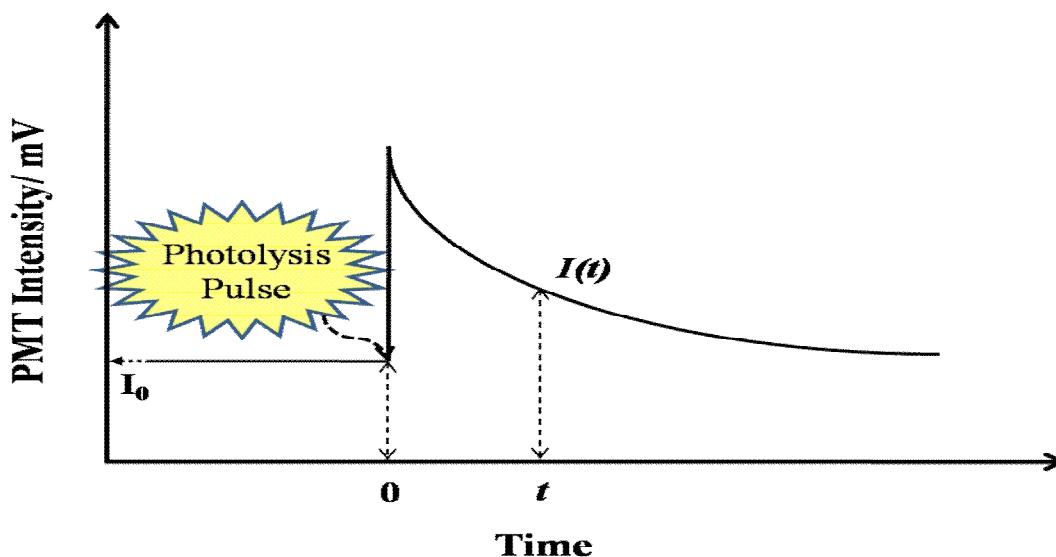
Figure 2.8   Schematic signal of absorption spectroscopy after laser flash photolysis.

2.4.2. Detection

The detection wavelength was determined based on the UV absorption spectrum of each radical. A wavelength of 253 nm for benzyl and *p*-fluorobenzyl, and 260 nm for the *p*-methylbenzyl radical (*p*-xylyl) were selected based on reference and measured UV absorption spectra. The transient absorption spectrum of each radical is discussed in detail later. The progress of each radical recombination reaction was monitored by recording the absorption signal of each radical at the selected wavelength on time scales of μs to ms. The light source used to monitor the absorption signals of benzyl and *p*-fluorobenzyl was a high-intensity Hg-Xe lamp (Ushio, model UXM-200 H, 200 W) because the lamp has a strong peak at 253 nm, which was ideal for these radicals. For a broadband absorption experiment, a high-pressure xenon arc lamp (Osram, model XBO 150W/1) was used as a light source instead of the Hg-Xe lamp. The radiant spectral distributions of the two lamps are shown in Figure 2.9.

(a)   (b)
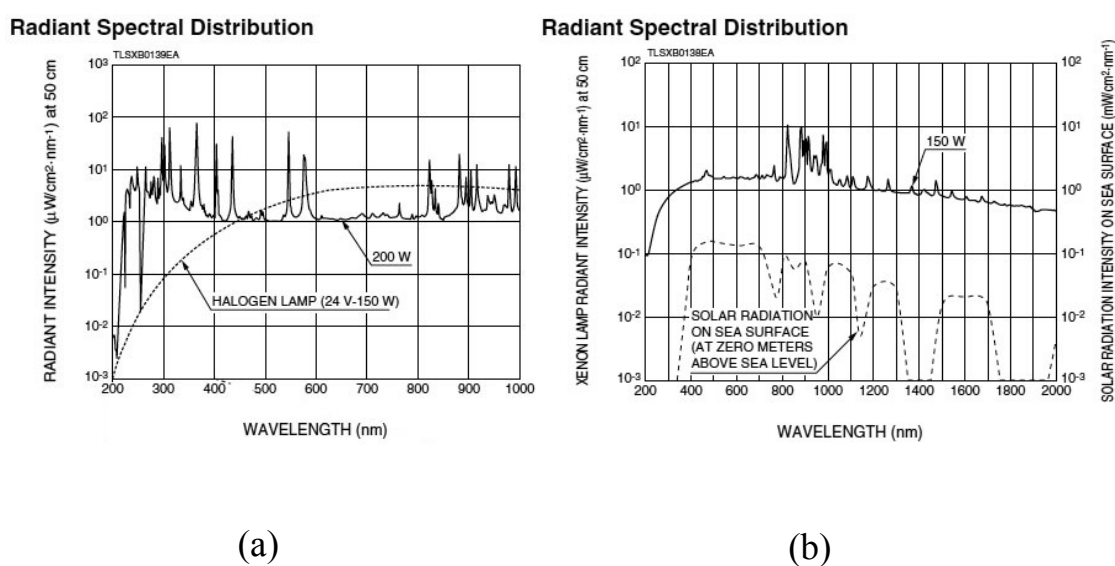
Figure 2.9   Radiant spectral distributions of (a) Hg-Xe and (b) Xe lamp.[34]

The lamp light from the source was collimated and focused using a set of lenses, denoted as L1, L2 and L3 in Figure 2.6. L1 was a biconvex lens with focal length $f = 100$ mm, L2 planoconvex, $f = 150$ mm and L3 biconcave with $f = -50$ mm. The absorption signal was detected by a prism-monochromator (Zeiss, model MM3)–photomuliplier tube (PMT, RCA, 1P28A) combination with a bandwidth of 2 nm. The RCA 1P28A is a standard PMT with well-known characteristics and it is sensitive over a wide spectral range between about 200 to

500 nm with a good quantum efficiency. The monochromator was set for wavelengths between 240 and 280 nm but most of the experiments were carried out at 253 nm or 260 nm, where the benzyl radical and p-methylbenzyl radical are found to possess maximum absorption coefficients, respectively.

The prism-monochromator was calibrated by a low-pressure mercury lamp (ORIEL, model 65130, 22–44W). The well-known two strong peaks of Hg lines at 253.6517 nm and 265.3679 nm were used to calibrate the monochromator. The entrance slit width of the monochromator was 1 mm. The calibration result is given in Figure 2.10.
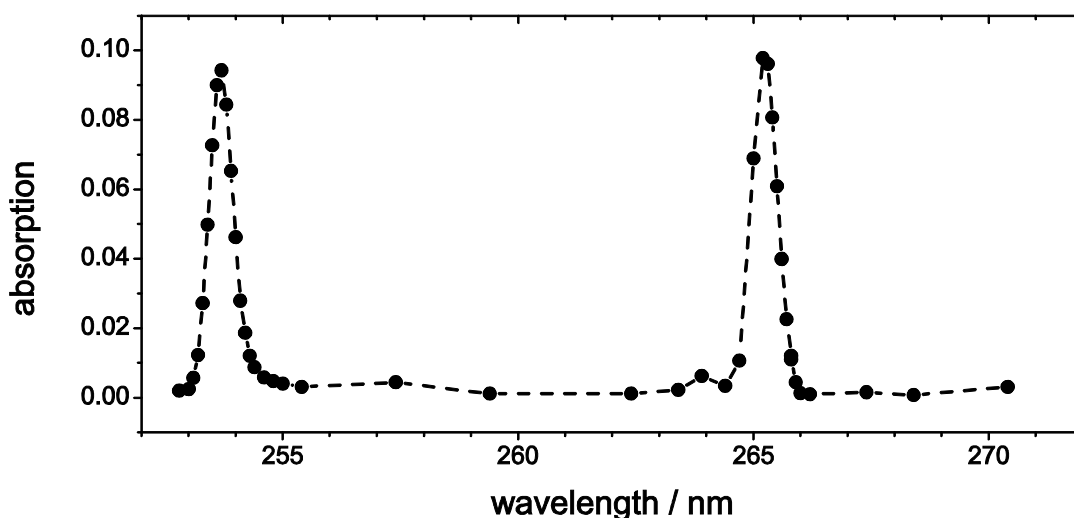
Figure 2.10   Calibration of the monochromator with a mercury lamp (-●-).

The rate constant is strongly dependent on the absorption cross-section (σ) of the radicals for the second-order kinetics, and the σ value has a wavelength dependence, and therefore, the accuracy of the monochromator is essential.

The absorption signal was recorded using a digital storage oscilloscope (LeCroy, model 9400 Dual 125 MHz and Tektronix, model TDS 684A) and saved directly to the computer. The oscilloscope and computer were interfaced by a GPIB card. Before starting the measurement, the discriminator level of the laser energy was set. If the laser energy exceeded or did not reach the discriminator levels within ± 10 % of the averaged value, the data was discarded. Either of two programs, one written in C++ and another in VEE 7.0, monitored the laser energy and the lamp intensity. Typically, between 100 and 200 shots, depending on the

signal intensity, were averaged. As *p*-methylbenzyl radicals have smaller absorption coefficients compared to benzyl, at least one hundred shots were averaged to get a satisfactory signal-to-noise ratio. Usually 2500 data points were recorded by the oscilloscope in each measurement.

2.4.3. Timing control

A pulse / delay generator (Stanford Research System, model DG 535/02) was interfaced with the laser controlling system and the oscilloscope. This pulse generator produced two TTL-pulses: The first pulse was sent to the electromagnetic shutter and to trigger the systems; the second pulse was sent to the oscilloscope and simultaneously to the second DG 535/02, which amplified the signal to 11 V to trigger the laser. The timing sequence is indicated in Figure 2.11.
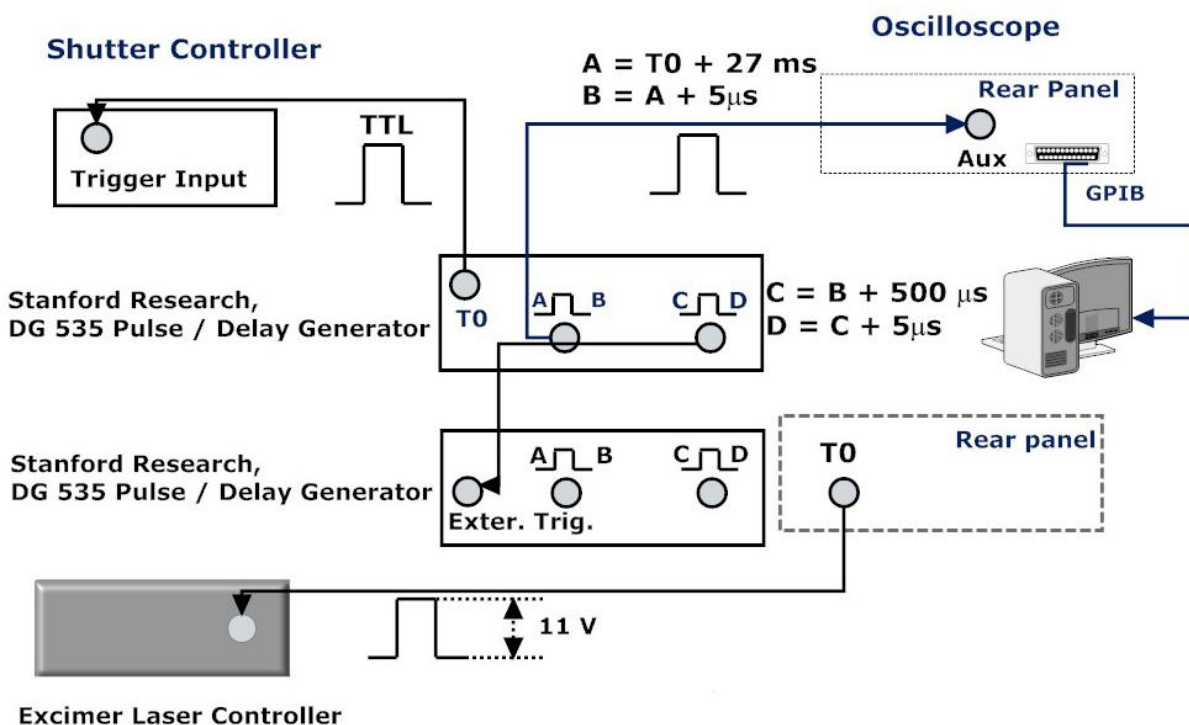
Figure 2.11 Schematic diagram of the timing control of the set-up.

As the decay of the signal typically finished within 10 ms, the opening time of the shutter was set to 40 ms, and the delay time between shutter opening and the laser pulse to 10–20 ms to achieve constant lamp intensity. The timing sequence is briefly described in Figure 2.12.
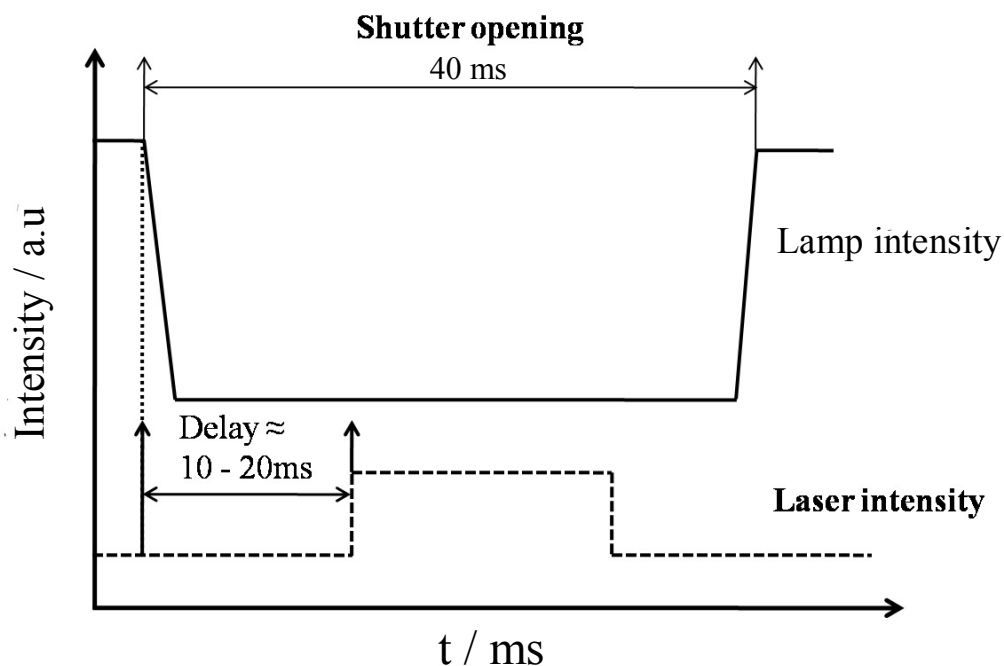
Figure 2.12   Schematic representation of the shutter timing sequence.

2.5.   Gas mixing and gas flow systems

The gas mixing system, both for time-resolved absorption measurements and for transient absorption spectra, is comprised of four gas-mixing vessels. Two mixing vessels, made of stainless steel with a capacity of 50 liters, were used for gas mixtures, for the high-pressure measurements with the compressor, or to investigate the temperature dependence of the rate constant. The other two mixing vessels, with a capacity of 2 liters, were used to investigate the pressure dependence of the rate constant up to 100 bar. A schematic representation of the mixing system is shown in Figure 2.13.

The gas mixtures were prepared in 3 steps:

1. Evacuation of the mixing vessels to below 10^{-3} mbar.
2. Filling the vessels with Cl_2 gas and the target precursors.
3. Filling the vessels with the bath gases up to the required pressures.

All the precursors used for mixture preparations and Cl_2 gas were thoroughly degassed through repeated pump-thaw-freeze cycles, before the required vapor pressure of the reactants was admitted to the vessel. After admission, the vessels were left for homogeneous mixing of the whole volume typically overnight. The bath gases helium, argon, xenon, N_2, and CO_2 had purities greater than 99.998%. Impurities in the bath gases, especially oxygen, were carefully removed by a series of gas cleaning adsorbers (Messer-Griesheim, model Oxysorb, and Alltech, model Oxytrap). Additional reactions of the radicals with oxygen can lead to an overestimate of the measured self-recombination reaction rate of radicals. Based on the experimental results, the gas purifying system was proven to be very effective to remove impurities especially oxygen. To increase the efficiency of the oxygen removal by the Oxysorb and Oxitrap cartridges, the filling rate of the bath gas was controlled not to exceed 1 bar / min.
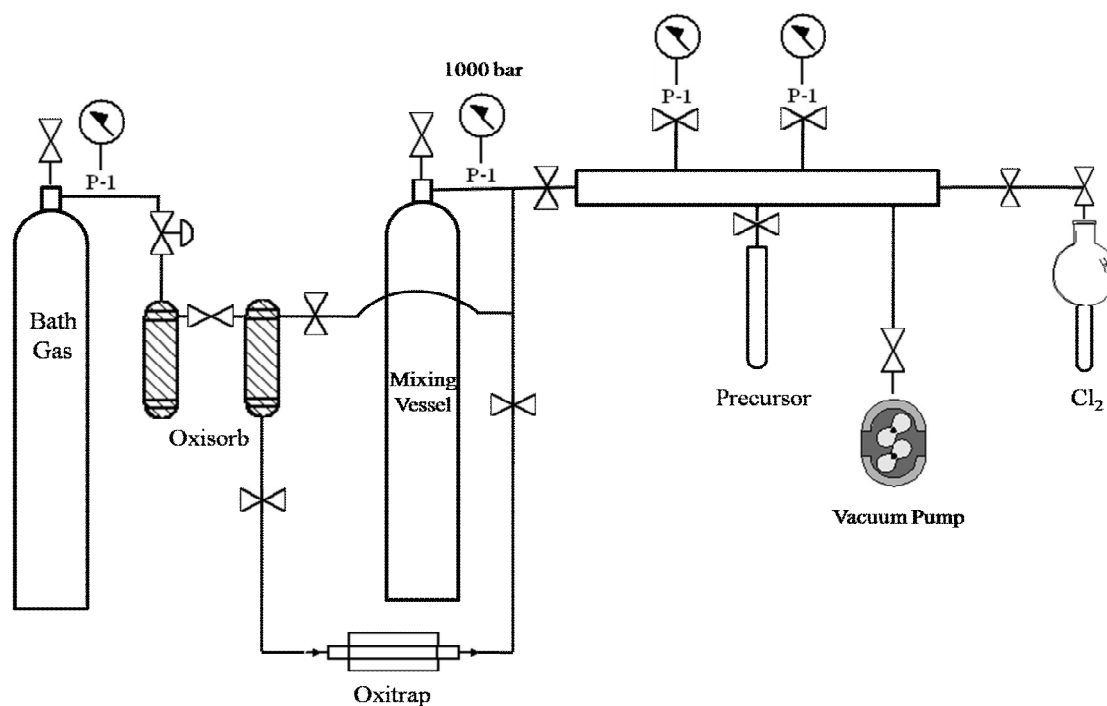
Figure 2.13   Schematic representation of the gas mixing and purifying system.

Pressures up to 120 bar could be reached without the use of a compressor. The mixing vessels were directly connected to the high-pressure optical cell and the pressure was controlled by two micro-metering valves. The compressor was used to acquire pressures higher than 120 bar and was placed between the high-pressure cell and the mixing vessel. Usually, the value from the pressure gauge, placed directly on the high-pressure cell, was sent to the controller of the compressor as the reference value. As the pressures between the micro-metering valve and inside the cell are different, a manometer was used to check the pressure between the compressor outlet and the first micro metering valve for safety reasons.

The chemicals and gases used here are given in Table 2.1 and the physical properties of precursor molecules are summarized in Table 2.2.

Table 2.1   Gases and chemicals.

Chemical	Purity / %	Manufacturer	CAS-Nr.
Toluene	99.8	Aldrich	108-88-3
p-Fluorotoluene	99	Alfa Aesar	352-32-9
Cumene	99.9	Acros Organics	98-82-8
p-Xylene	99	Aldrich	106-42-3
Cl_2	99.8	Air Liquid	7782-50-5
CF_4	99.995	Messer	75-73-0
CF_3H	99.995	Messer	75-46-7
SF_6	99.9	Messer	2551-62-4
CO_2	99.998	Air Liquid	124-38-9
He	99.999	Air Liquid	7440-59-7
Ar	99.998	Air Liquid	7440-37-1

The vapor pressure of the precursor is one of the key factors to select the target molecule. If the substance is a powder or has a low vapor pressure at room temperature, it is difficult to achieve a sufficient concentration of the precursor molecule in the vessel.

Table 2.2   The physical properties of the precursor molecules.

Molecule	Molecular weight / u	Vapor pressure /mbar at 293 K	Boiling point / K	Melting point / K
Toluene	92.1384	29.8	383	180
p-Fluorotoluene	110.1289	54.2	389	217
p-Xylene	106.1650	12.2	411	285

2.6.   Evaluation and data processing

The absorption time profiles once converted from experimentally obtained PMT intensity time profiles are then fitted with a mathematical function. Figure 2.14 schematically represents the time profiles before (i) and after (ii) conversion.
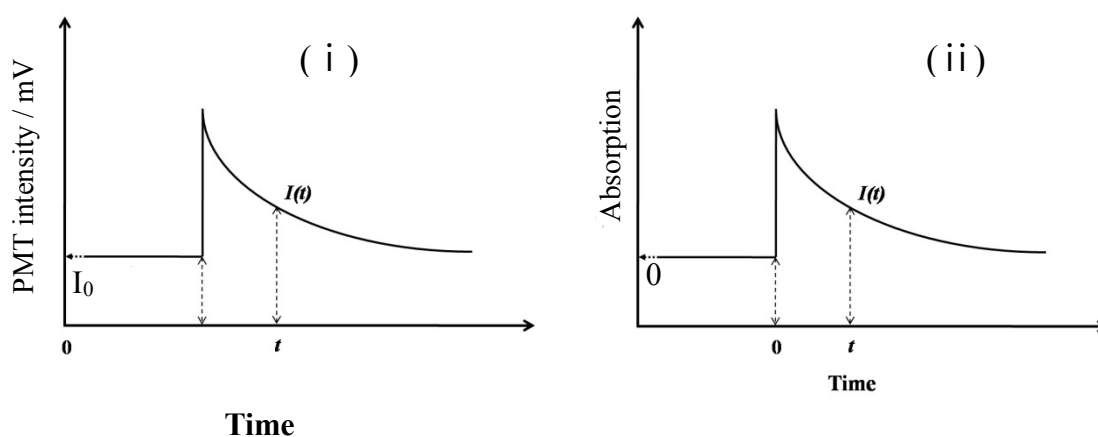
Figure 2.14   PMT intensity time profile (i) and absorption time profile (ii).

The fitting function used for the second-order kinetics was

$$Abs(t) = \frac{[\text{radical}]_0 \cdot \sigma \cdot l}{1 + 2 \cdot k \cdot t \cdot [\text{radical}]_0} + \text{offset} \tag{2.4}$$

Here, σ is the absorption cross-section of the radical, k the combination rate constant, l the

optical path length and [radical]$_0$ the concentration of the radicals at $t = 0$. [radical]$_0$, k and offset are the fitting parameters. The k values were obtained by fitting the experimental data with this function within a $\pm$ 95% confidence level.

Chapter 3

Results

3.1   Recombination reaction of *p*-fluorobenzyl radicals

Oum *et al.*[10] studied pressure and temperature dependent combination rate constants of benzyl radicals in helium, argon, xenon, N_2, and CO_2. An unexpected increase of the rate constant over the limiting high-pressure rate constant (k_∞^{ET}) was reported, which one obtains based on the traditional ET mechanism. In ref. 10, the magnitude of increase of the rate constant depended on the bath gas and increased in the order He $<$ N_2 $\approx$ Ar $\approx$ Xe $<$ CO_2. The RC mechanism was used to interpret the observed rate constants of the benzyl radical combination reaction.

The combination of *p*-fluorobenzyl radicals has been investigated in order to see if the enhancement of recombination rate constants at high pressures, observed in the benzyl radical recombination reaction, can also be found in the case of *p*-fluorobenzyl radicals.[35] Additionally, the effect of fluorine substitution of the benzyl ring was investigated. As fluorine is the strongest electron-withdrawing substituent, the substituent effect on the radical stability and the relation between the radical stability and recombination rate constant can also be investigated. The rate constants of the combination reaction

$$p\text{-F-}C_6H_4\text{-}CH_2 \quad + \quad p\text{-F-}C_6H_4\text{-}CH_2 \quad (+M) \quad \rightarrow \quad C_{14}H_{12}F_2 \quad (+M) \qquad k_1 \qquad (3.1.1)$$
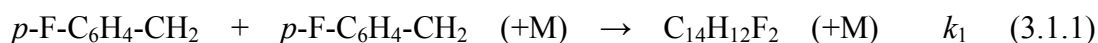
have been measured over the pressure range 0.2–800 bar and the temperature range 255-420 K. Helium, argon, and CO_2 were employed as bath gases (M). There have been several previous measurements related to *p*-flurobenzyl radicals in the gas-phase. The reaction rates of *p*- and *m*-fluorobenzyl radicals with O_2, NO and NO_2 were investigated by discharge flow/laser-induced fluorescence experiments.[36,37] As the fluorine substituted aromatic compounds emit strong fluorescence in the visible region, most of the spectroscopic measurements of *p*-fluorobenzyl radicals were conducted in the visible region (absorption and fluorescence spectra, fluorescence lifetime).[1,2,9,38,39] However, no direct study of the absorption band of *p*-fluorobenzyl radicals in the UV region is available, and there has been no direct measurement of reaction (3.1.1) in the gas-phase either.

In the present work, first, the transient UV absorption spectrum of *p*-fluorobenzyl radicals at room temperature was measured and then the pressure- and temperature-dependence of the absorption coefficient was investigated. The study of the pressure- and temperature-dependent rate constant, k_1, which may provide another example for a significant contribution of the radical-complex mechanism in the gas-liquid transition region are presented.

Like benzyl radicals, *p*-fluorobenzyl radicals were generated by laser flash photolysis of Cl_2 at 308 nm and the subsequent reaction of Cl atoms with excess *p*-fluorotoluene

$$Cl_2 \quad + \quad h\nu\,(308\;nm) \quad \rightarrow \quad 2Cl \qquad\qquad (3.1.2)$$

$$Cl \quad + \quad p\text{-F-C}_6\text{H}_4\text{-CH}_3 \quad \rightarrow \quad p\text{-F-C}_6\text{H}_4\text{-CH}_2 \quad + \quad HCl \qquad\qquad (3.1.3)$$
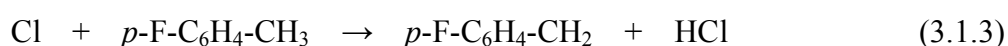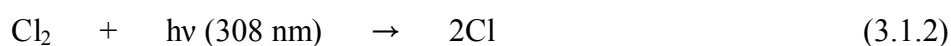
The processes to generate *p*-fluorobenzyl radicals are similar to those of benzyl radicals.[3] The rate constant of reaction (3.1.3) is nearly as large as $k(Cl + toluene) = 6 \times 10^{-10}\,cm^3\,molecule^{-1}\,s^{-1}$.[4] Under these conditions, Cl atoms are instantly and stoichiometically converted to *p*-fluorobenzyl radicals. Typical concentrations were $[Cl]_0\ (=[p\text{-fluorobenzyl}]_0) = (1-5) \times 10^{13}$ molecule s^{-3} and $[p\text{-fluorotoluene}] = (0.7-7) \times 10^{16}$ molecule cm^{-3}.

3.1.1. Determination of $\sigma_{p\text{-fluorobenzyl}}$ and the radical spectrum of p-fluorobenzyl radical

As reaction (3.1.3) follows second-order kinetics and therefore the measured rates are sensitive to the absorption coefficient $\sigma_{p\text{-fluorobenzyl}}$, it is essential to determine values of $\sigma_{p\text{-fluorobenzyl}}$ prior to the kinetic analysis. In the following, we describe how they were experimentally determined. We employed benzyl radicals as a calibration source at the probe wavelength of 253 nm; the absorption coefficient σ_{benzyl} at 253 nm is already known in the literature.[9] Such a calibration procedure was necessary mainly because one cannot easily determine the excitation yield of Cl_2 and the subsequent quantity of $[Cl]_0$ in equation 3.1.2. This quantity can be estimated, if one keeps the same initial concentrations of $[Cl_2]$ for two independent gas mixtures of $[Cl_2]_0$ + [toluene] and $[Cl_2]_0$ + [p-Fluorotoluene]$_0$.
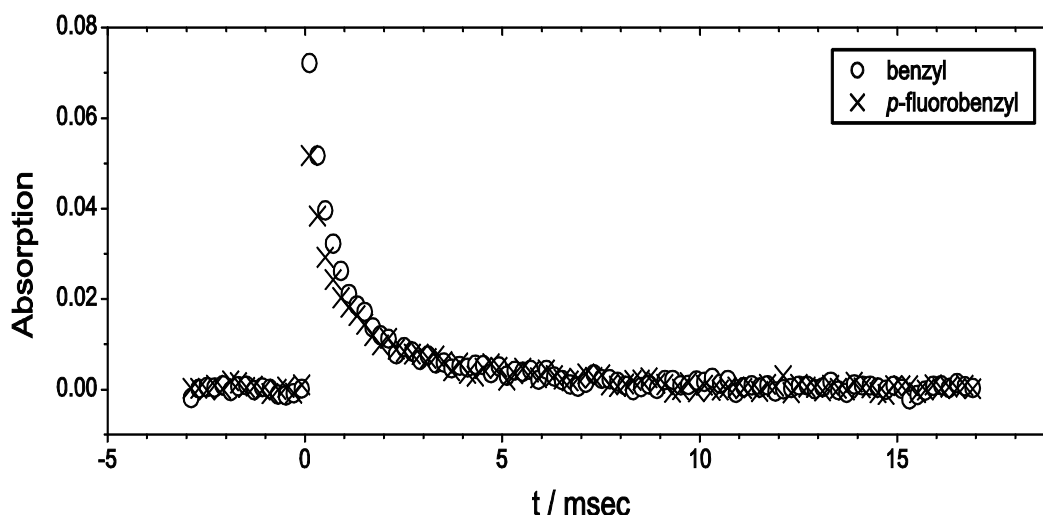
Figure 3.1.1   Typical transient absorption signals of benzyl (○) and p-fluorobenzyl radicals (×) at 253 nm. Signals were recorded after the photolysis at 308 nm of mixtures with the same initial concentration: 0.06 mbar of Cl_2 and 0.28 mbar of toluene and p-fluorotoluene in 700 mbar Ar at 300 K.

First, we measured the absorption-time traces of benzyl radicals at 253 nm, produced in reaction 3.1.1 when toluene was employed instead of p-fluorotoluene. Then, for the same initial concentration of Cl_2, absorption-time traces of p-fluorobenzyl radicals were measured. The absorption maxima were normalized to the laser intensities. Finally, the differences in the absorption signals were compared as shown in Figure 3.1.1 as an example.

The time traces of benzyl radical and p-fluorobenzyl radicals under the same experimental conditions are shown in Figure 3.1.1. Such time traces of both radicals were

measured at various pressures and $Abs_{p\text{-fluorobenzyl}}$ / Abs_{benzyl} ratios measured under various experimental conditions are presented in Figure 3.1.2. As a result, the absorption signals of p-fluorobenzyl radicals were found to be (65 ± 8) % of those of benzyl radicals.
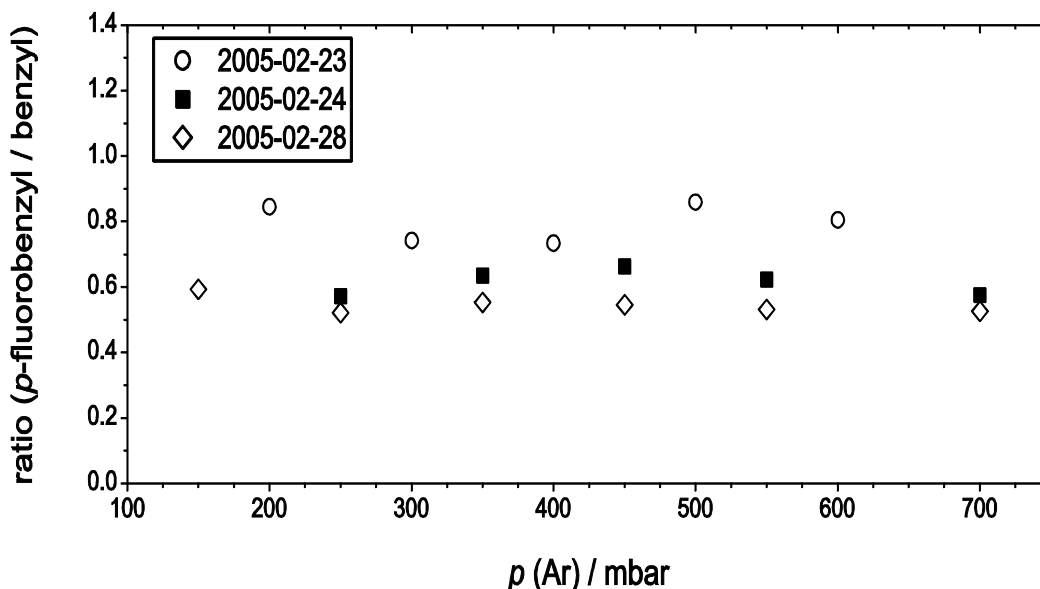
Figure 3.1.2   The ratio of $Abs_{max}(p\text{-fluorobenzyl})$ to $Abs_{max}(benzyl)$ in the pressure range 150 – 700 mbar in Ar at 300 K. Different symbols indicate the data obtained at different days of experiments.

Since the absorption coefficient of benzyl radicals at 253 nm is known to be σ_{benzyl} (253 nm) = 1.3 $\times$ 10^{-16} cm^2 molecule^{-1}, we could determine $\sigma_{p\text{-fluorobenzyl}}$ (253 nm) to be (8.4 ± 1.0) $\times$ 10^{-17} cm^2 molecule^{-1} based on the experimental results presented in Figure 3.1.2. The absorption-time profiles of p-fluorobenzyl radicals were measured at different detection wavelengths between 237 nm and 262 nm with identical initial concentrations of Cl_2 and p-fluorotoluene. As we kept the same experimental conditions during all measurements, the difference of maximum absorption at each wavelength is due to the absorption coefficient. First, we measured the maximum absorption at each wavelength, and these values were corrected with respect to the laser energy and the lamp intensity. As $\sigma_{p\text{-fluorobenzyl}}$ (253 nm, 300 K) was determined to be 8.4 $\times$ 10^{-17} cm^{2}molecule^{-1}, absorption coefficients of p-fluorobenzyl radical at other wavelengths were then scaled to the value at 253 nm. The resulting $\sigma_{p\text{-fluorobenzyl}}$ (λ, 300 K) is shown in Figure 3.1.3. and the values are summarized in Table 3.1.1.
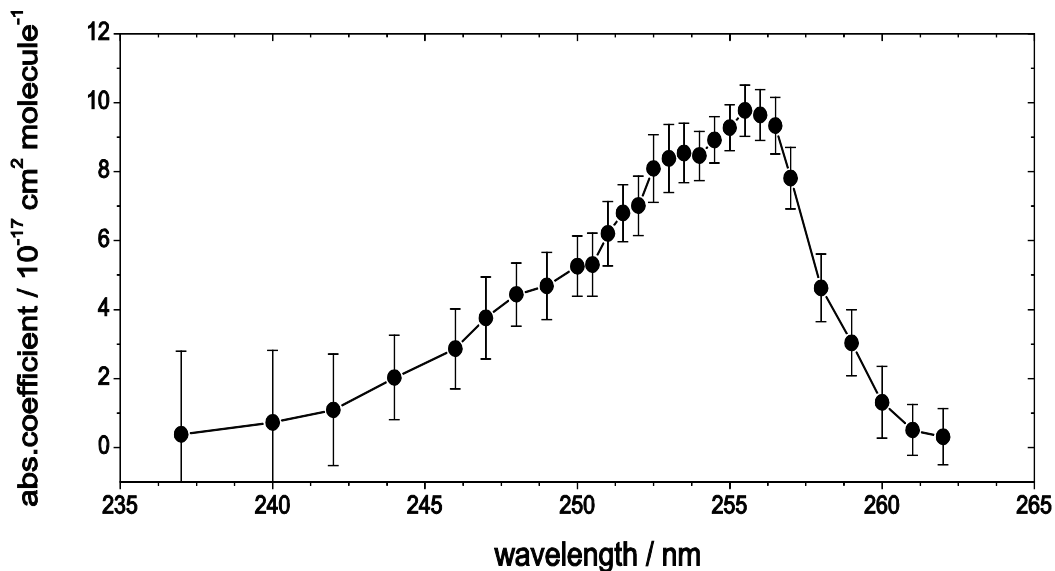
Figure 3.1.3   Transient absorption spectrum of *p*-fluorobenzyl radicals in 350 mbar Ar at 300 K. The $\sigma_{p\text{-fluorobenzyl}}$ values were calibrated with the reference value of the well-known σ_{benzyl} at 253 nm (see text). Error bars indicate the statistical error.

The maximum absorption was located at 256 nm, slightly shifted to the red relative to that of benzyl radical (253 nm).

Table 3.1.1   Absorption coefficients of *p*-fluorobenzyl radicals, $\sigma_{p\text{-flurorbenzyl}}$, at 300 K.

λ / nm	$\sigma_{p\text{-fluorobenzyl}}$[a]	λ / nm	$\sigma_{p\text{-fluorobenzyl}}$[a]	λ / nm	$\sigma_{p\text{-fluorobenzyl}}$[a]
237	0.4 ± 2.4	251	6.2 ± 0.9	256	9.6 ± 0.7
240	0.7 ± 2.1	251.5	6.8 ± 0.8	256.5	9.3 ± 0.8
242	1.1 ± 1.6	252	7.0 ± 0.9	257	7.8 ± 0.9
244	2.0 ± 1.2	252.5	8.1 ± 1.0	258	4.6 ± 1.0
246	2.9 ± 1.2	253	8.4 ± 1.0	259	3.0 ± 1.0
247	3.8 ± 1.2	253.5	8.5 ± 1.0	260	1.3 ± 1.0
248	4.4 ± 0.9	254	8.5 ± 0.7	261	0.5 ± 0.7
249	4.7 ± 1.0	254.5	8.9 ± 0.7	262	0.3 ± 0.8
250	5.3 ± 0.9	255	9.3 ± 0.7		
250.5	5.3 ± 0.9	255.5	9.8 ± 0.7		

[a] Absorption coefficients, given in 10^{-17} cm^2 molecule^{-1}

3.1.2. *P*- and *T*-dependent absorption coefficients of *p*-fluorobenzyl radicals

As experiments were conducted over a wide range of temperatures (255–420 K) and pressures (0.2–800 bar), it is necessary to determine the temperature and pressure dependence of $\sigma_{p\text{-fluorobenzyl}}$. Figure 3.1.4 shows the pressure dependence of the absorption coefficient. The absorption coefficient $\sigma_{p\text{-fluorobenzyl}}$ was found to be weakly dependent on the pressure. In Figure 3.1.4, the ratios of $[p\text{-fluorobenzyl}]_0$ / [Ar] and $[p\text{-fluorobenzyl}]_0$ / $[CO_2]$ were kept constant at different argon pressures between 100 and 800 bar and CO_2 between 10 and 50 bar. The maximum absorption value of *p*-fluorobenzyl radicals at $t = 0$ as a function of argon density (Figure 3.1.4 (a)) and CO_2 density (Figure 3.1.4 (b)) were found to be linear, and this indicates no complications by solvent-induced changes of the absorption coefficients.
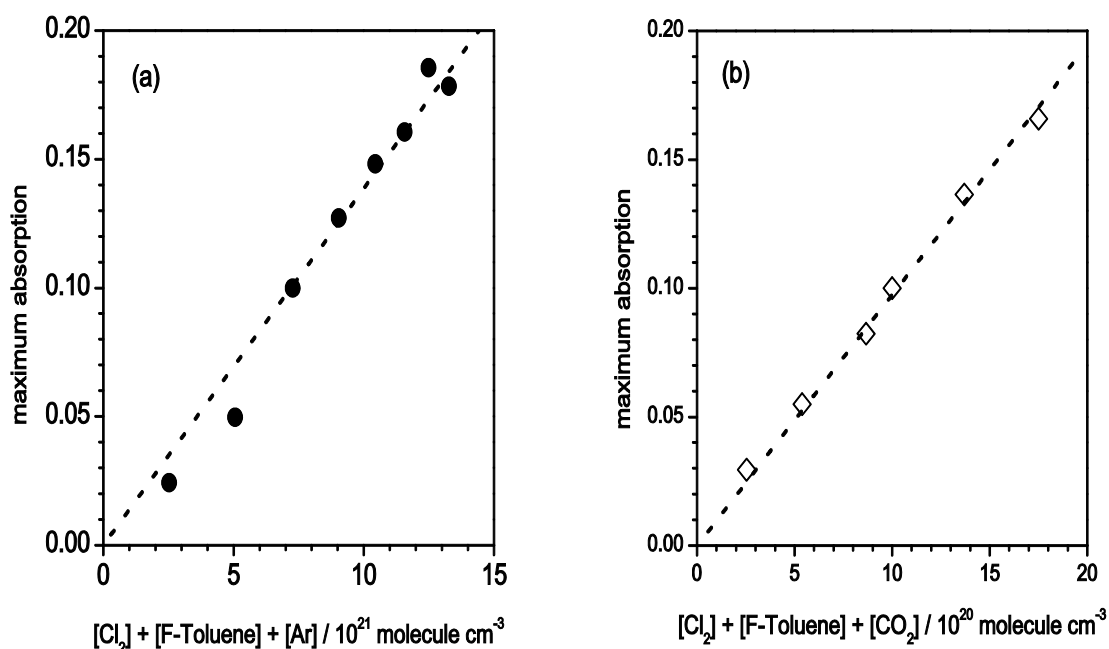
Figure 3.1.4   Density dependence of the absorption coefficient σ of *p*-fluorobenzyl radicals. (a) Maximum absorption of *p*-fluorobenzyl radicals at 253 nm at different Ar pressures (100–800 bar) with constant [Cl_2] / [bath gas] ratio, (b) at different CO_2 pressures (10– 49 bar) with constant ratio [Cl_2] / [bath gas].

In Figure 3.1.5, the absorption coefficients of the *p*-fluorobenzyl radical at different temperatures between 255 and 420 K are shown. The solid line in Figure 3.1.5 represents a fit.

The absorption coefficient $\sigma_{p\text{-fluorobenzyl}}$ shows a weak temperature dependence expressed as

$$\sigma_{p-\text{fluorobenzyl}}(T, 253\,\text{nm}) = (8.4 \times 10^{-17})(\frac{T}{300\,\text{K}})^{-0.05}\,\text{cm}^2\text{molecule}^{-1} \qquad (3.1.4)$$
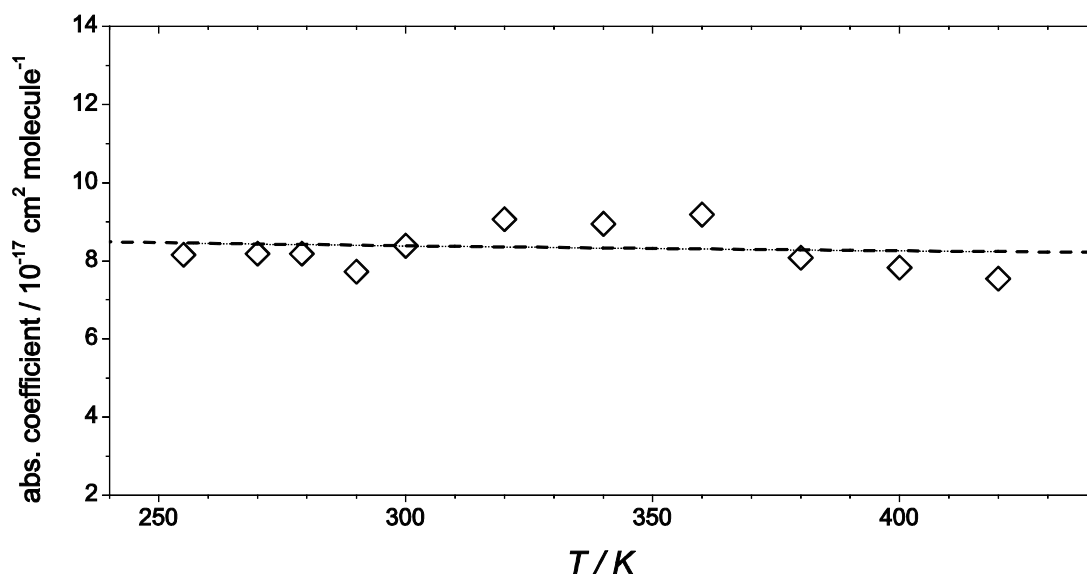
Figure 3.1.5 Temperature dependence of the absorption coefficient of p-fluorobenzyl radicals, $\sigma_{p\text{-fluorobenzyl}}$ in He 5 bar. The values were calibrated at 253 nm over the range 255–420 K and the line indicates the fit with eqn. 3.1.4.

3.1.3. Absorption-time profiles at 253 nm

Figure 3.1.6 shows a typical absorption–time profile of p-fluorobenzyl radicals at 253 nm in 800 bar of argon at 300 K. All absorption-time profiles showed the instant increase of the p-fluorobenzyl radical concentrations, resulting from the H-atom abstraction from p-fluorotoluene by the Cl atom. Clean second-order decay followed the instant increase of absorption. The decay was entirely assignable to reaction 3.1.1. The solid line in Figure 3.1.6 represents a fit for reaction (3.1.1) where the fitting function is:

$$Abs(t) = \frac{a_0 \cdot \sigma \cdot l}{1 + 2 \cdot k \cdot t \cdot a_0} + offset \qquad\qquad (3.1.5)$$

where a_0 denotes the initial concentration of p-fluorobenzyl radicals at $t = 0$, σ is the absorption coefficient of the p-fluorobenzyl radicals at 253 nm, l is the optical path length and k is the rate constant of recombination of p-fluorobenzyl radicals. k, a_0 and $offset$ were set as the fitting parameters. The rate constant of recombination of p-fluorobenzyl radicals can be easily extracted from the absorption signal by employing this fitting function. The profiles were well described by the fitting function, eqn. 3.1.5 and this means that there are no serious systematic deviations, giving additional support to the reported values of k_1.
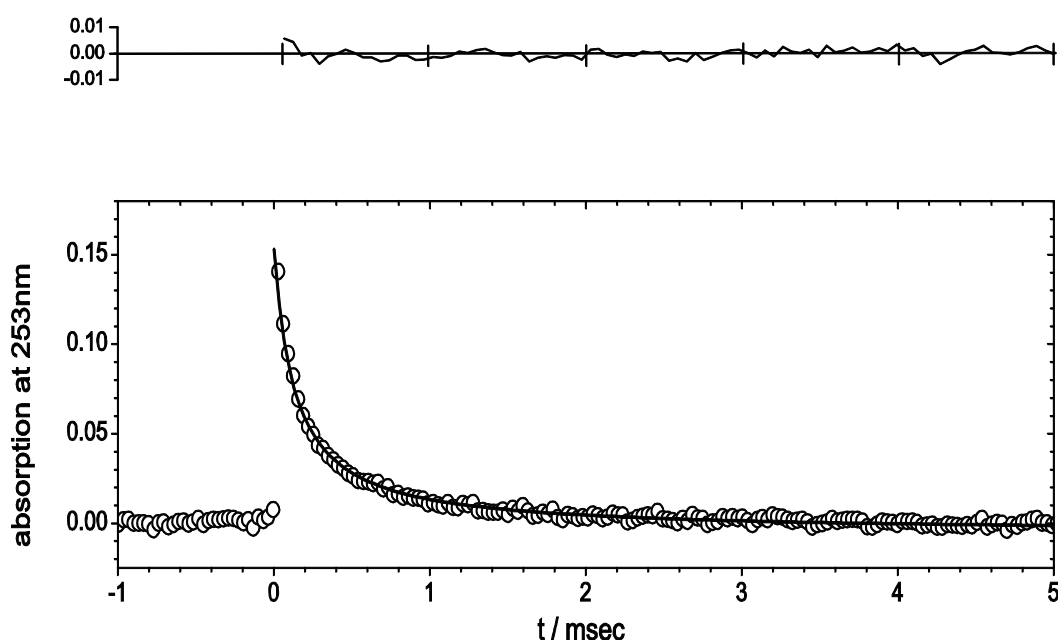
Figure 3.1.6 Typical absorption signal of p-fluorobenzyl radicals at 253 nm, recorded after the photolysis at 308 nm of mixtures of 1.9 mbar of Cl_2, 9.8 mbar p-fluorotoluene and 800 bar of argon at 300 K. ($\circ$) : Experimental data, (solid line) : fit with eqn. 3.1.5. The upper figure is the fit residual.

3.1.4. Pressure and temperature dependence of k_1

As for benzyl radicals, pressure- and bath-gas-independent rate constant values of k_1 were observed below 1 bar. Therefore the limiting "high-pressure" rate constant of the ET mechanism, $k_{1,\infty}^{ET}$, was derived from these constant k_1 values, independent of the bath gas and determined by considering all data points below 1 bar in He, Ar and CO_2.

The experimental results for the pressure dependence of k_1 at 300 K are shown in Figure 3.1.7.
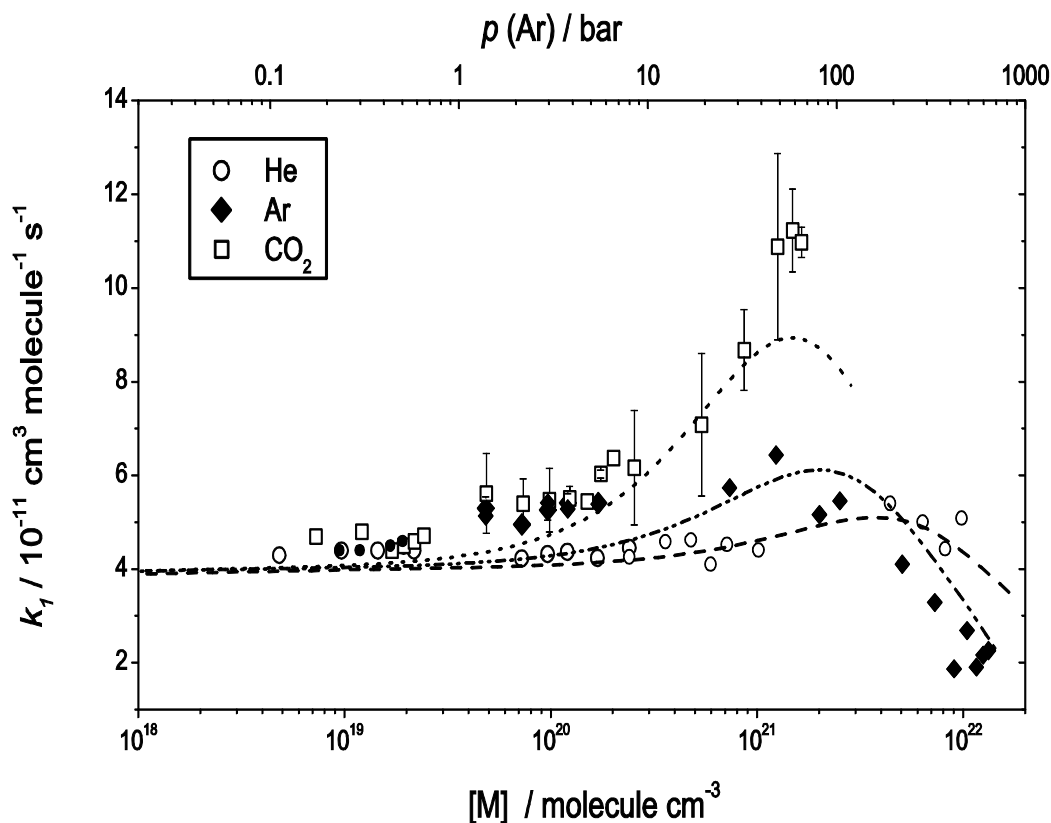
Figure 3.1.7 Rate constant k_1 for recombination of p-fluorobenzyl radicals in helium (○), argon (♦) and CO_2 (□) at 300 K. Error bars for CO_2 indicate the experimental scatter. Lines are rate constants for recombination of unsubstituted benzyl radicals in helium (---), argon (•••) and CO_2 (-••), given for comparison.

The limiting high-pressure rate constants of the energy-transfer-mechanism, $k_{1,\infty}^{ET}$ is

$$k_{1,\infty}^{ET}(300\,\text{K}) = (4.3 \pm 0.5) \times 10^{-11}\,\text{cm}^3\text{molecule}^{-1}s^{-1} \tag{3.1.6}$$

In helium, the k_1 values remained constant at pressures up to 80 bar. In contrast, at pressures

45

above 5 bar, clear indications of a further increase of k_1 were recognized in the bath gases argon and CO_2 in Figure 3.1.7. The results of the pressure dependence of k_1 at 300 K are also summarized in Table 3.1.2.

Tabel 3.1.2 Rate constants for the combination reaction of *p*-fluorobenzyl radicals (k_1) in helium, argon and CO_2 at 300 K.

(a) M = CO_2 at 300 K

p (CO_2)[a]	[CO_2][b]	k_1[c]	p (CO_2)[a]	[CO_2][b]	k_1[c]	p (CO_2)[a]	[CO_2][b]	k_1[c]
0.3	7.25E18	4.5	3	7.35E19	5.4	20	5.39E20	7.1
0.5	1.21E19	4.4	4	9.85E19	5.5	30	8.67E20	8.7
0.7	1.70E19	4.4	5	1.24E20	5.5	40	1.26E21	10.1
0.8	1.94E19	4.4	6	1.5E20	5.4	45	1.49E21	11.2
0.9	2.18E19	4.6	7	1.75E20	6.0	48	1.64E21	10.0
1	2.43E19	4.7	8	2.01E20	6.4			
2	4.87E19	5.6	10	2.54E20	6.2			

(b) M = He at 300 K

p (He)[a]	[He][b]	k_1[c]	p (He)[a]	[He][b]	k_1[c]	p (He)[a]	[He][b]	k_1[c]
0.2	4.83E18	4.3	5	1.20E20	4.4	30	7.14E20	4.5
0.4	9.65E18	4.5	7	1.68E20	4.2	43	1.02E21	4.4
0.6	1.45E19	4.4	10	2.40E20	4.5	200	4.42E21	5.4
0.8	1.93E19	4.4	10	2.40E20	4.3	300	6.36E21	5.0
0.9	2.17E19	4.4	15	3.60E20	4.6	400	8.15E21	4.4
3	7.23E19	4.2	20	4.78E20	4.6	500	9.82E21	5.1
4	9.64E19	4.3	25	5.97E20	4.1			

(c) M = Ar at 300 K

P (Ar)[a]	[Ar][b]	k_1[c]	p (Ar)[a]	[Ar][b]	k_1[c]	p (Ar)[a]	[Ar][b]	k_1[c]
0.39	9.45E18	4.2	4	9.68E19	5.4	100	2.53E21	5.5
0.49	1.19E19	4.3	5	1.21E20	5.4	200	5.06E21	4.1
0.69	1.67E19	4.3	5	1.21E20	5.3	300	7.27E21	3.3
0.79	1.91E19	4.4	7	1.70E20	5.4	400	9.04E21	1.9
2	4.83E19	5.3	7	1.70E20	5.4	500	1.04E22	2.7
2	4.83E19	5.1	10	2.43E20	6.2	600	1.16E22	1.9
3	7.25E19	5.0	30	7.37E20	5.7	700	1.25E22	2.2
3	7.25E19	4.9	50	1.24E21	6.4	800	1.33E22	2.3
4	9.68E19	5.3	80	2.01E21	5.2			

[a] Pressure of the bath gas, given in bar.　[b] Density of the bath gas, given in molecule cm^{-3}.

[c] Rate constant, given in 10^{-11} cm^3 molecule^{-1} s^{-1}.

The rate constant gradually increases until it levels off at densities where the influence of diffusion control sets in. The finally observed decrease of the rate constants at high pressures corresponds to the regime of diffusion-controlled kinetics as expected for these densities. The pressure-induced enhancement of k_1 increases in the order He < Ar < CO_2, similarly to recent studies of combination reactions of CCl_3 radicals[5] and benzyl radicals.[7] For the comparison with earlier results on the recombination of unsubstituted benzyl radicals, three lines representing the pressure dependence of benzyl radical recombination in helium, argon, and CO_2 were added in Figure 3.1.7. Except for a slightly earlier onset of the enhancement of the k_1 values with a slightly larger magnitude in the present results, there were large similarities between the results from p-fluorobenzyl radicals and those from unsubstituted benzyl radicals.

The temperature dependence of $k_{1,\infty}^{ET}(T)$ was also investigated. First, the dependence was measured in helium at 5 bar and over the temperature range 255–420 K such as shown in Figure 3.1.8.
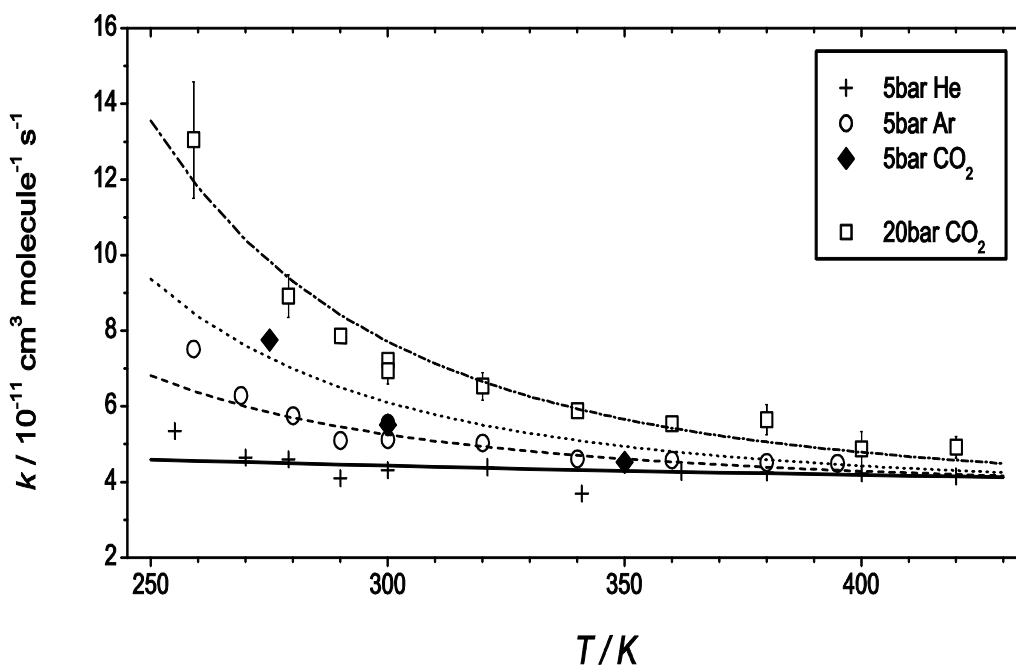
Figure 3.1.8   Temperature dependence of k_1 for 5 bar helium (+), argon (○), and CO_2 (♦), and for 20 bar CO_2 (□). Lines indicate the fit by Eqn. 3.1.7.

The results are summarized in Table 3.1.3.

Table 3.1.3 Rate constants for the combination reaction of *p*-fluorobenzyl radicals (k_1) in helium, argon (5 bar) and CO_2 (5 bar and 20 bar) at various temperatures.

(a) M = He (5 bar) at 300 K

T/K	[M] [a]	k_1 [b]	T/K	[M] [a]	k_1 [b]	T/K	[M] [a]	k_1 [b]
255	1.21E20	5.4	300	1.21E20	4.3	380	1.21E20	4.3
270	1.21E20	4.6	321	1.21E20	4.4	400	1.21E20	4.2
279	1.21E20	4.6	341	1.21E20	3.7	420	1.21E20	4.2
290	1.21E20	4.1	362	1.21E20	4.3			

(b) M = Ar (5 bar) at 300 K

T/K	[M] [a]	k_1 [b]	T/K	[M] [a]	k_1 [b]	T/K	[M] [a]	k_1 [b]
259	1.20E20	7.5	300	1.20E20	5.1	360	1.20E20	4.6
269	1.20E20	6.3	300	1.20E20	5.6	380	1.20E20	4.5
280	1.20E20	5.8	320	1.20E20	5.0	395	1.20E20	4.5
290	1.20E20	5.1	340	1.20E20	4.6			

(c) M = CO_2 (5 bar) at 300 K

T/K	[M] [a]	k_1 [b]	T/K	[M] [a]	k_1 [b]	T/K	[M] [a]	k_1 [b]
275	1.36E20	7.8	300	1.24E20	5.5	350	1.05E20	4.5

(d) M = CO_2 (20 bar) at 300 K

T/K	[M] [a]	k_1 [b]	T/K	[M] [a]	k_1 [b]	T/K	[M] [a]	k_1 [b]
259	5.39E20	13.1	300	5.39E20	7.0	380	3.99E20	5.7
279	5.39E20	8.9	320	4.93E20	6.5	400	3.76E20	4.9
290	5.39E20	7.9	340	4.56E20	5.9	420	3.55E20	4.9
300	5.39E20	7.2	360	4.25E20	5.5			

[a] Density of the bath gas, given in molecule cm^{-3}. [b] Rate constant, given in 10^{-11} cm^3 $molecule^{-1}$ s^{-1}.

A modest negative temperature dependence of $k_{1,\infty}^{ET}$ was observed. Additionally, Ar and CO_2 were used as bath gases to check the temperature dependence of $k_{1,\infty}^{ET}$. Unlike in He, at 5 bar, the enhancement of the k_1 values was clearly taking place at lower temperatures in Ar and even more significantly in CO_2.

The measurements were conducted under the same density conditions. As 5 bar helium at 300 K is equal to 1.2×10^{20} molecule cm^{-3}, the pressures at each temperature were changed to maintain this density. At temperatures near 400 K, the rate constants k_1 values were almost the same. Based on the same rate constant value at high temperatures near 400 K regardless of the

bath gas employed, the temperature dependence of $k_{1,\infty}^{ET}$ could be safely determined from the results in He (5 bar). The resulting temperature dependence of $k_{1,\infty}^{ET}$ over the temperature range 255–420 K can be expressed as

$$k_{1,\infty}^{ET} = (4.3 \pm 0.5) \times 10^{-11} (\frac{T}{300\,\text{K}})^{-0.2}\,\text{cm}^3\text{molecule}^{-1}\text{s}^{-1} \qquad (3.1.7)$$

In contrast, a distinct temperature dependent enhancement of k_1 over the full pressure range was observed in CO_2 at 275, 300, 350 and 400 K. The results are shown in Figure 3.1.9 and summarized in Table 3.1.4.
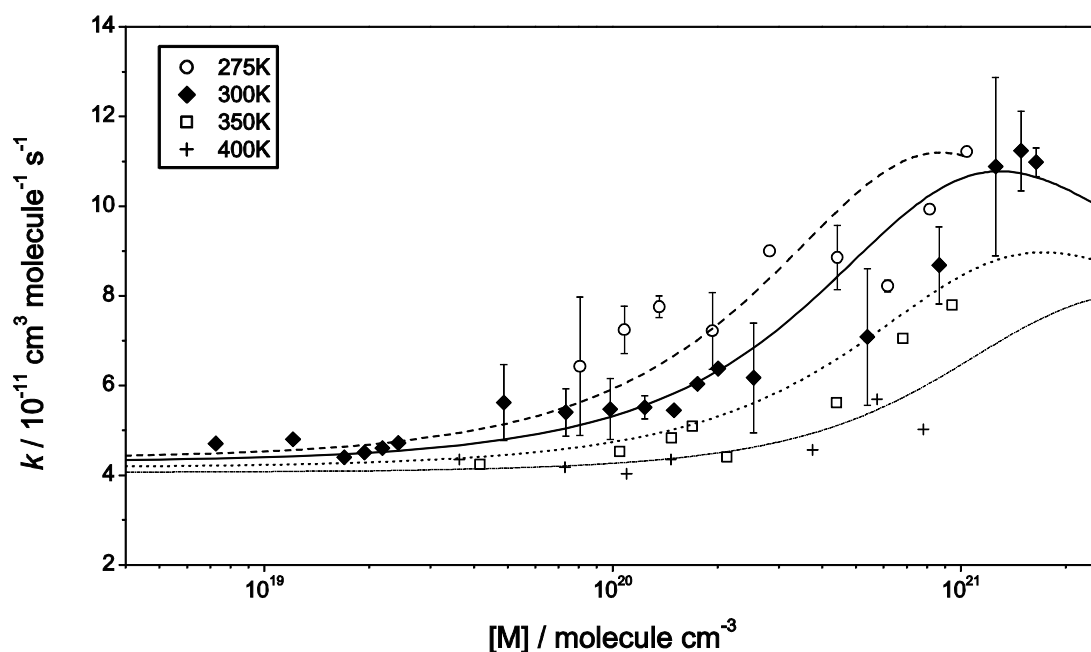
Figure 3.1.9 Density-dependent recombination rate constant at 275 K (○), 300 K (♦), 350 K (□) and 400 K (+). Lines indicate the fits at 275 K (---), 300 K (−), 350 K (•••) and 400 K (-•-).

The most pronounced enhancement of k_1 was observed at 275 K and a much weaker one was observed again with increasing temperature.

49

Table 3.1.4   Rate constants for the combination reaction of *p*-fluorobenzyl radicals (k_1) in CO_2 at 275, 350 and 400 K.

(a) M = CO_2 at 275 K

$p\ (CO_2)$[a]	$[CO_2]$[b]	k_1[c]	$p\ (CO_2)$[a]	$[CO_2]$[b]	k_1[c]	$p\ (CO_2)$[a]	$[CO_2]$[b]	k_1[c]
3	8.06E19	6.4	7	1.93E20	7.2	20	6.17E20	8.2
4	1.08E20	7.2	10	2.83E20	9.0	25	8.13E20	9.9
5	1.36E20	7.8	15	4.42E20	8.9	30	1.04E21	11.2

(b) M = CO_2 at 350 K

$p\ (CO_2)$[a]	$[CO_2]$[b]	k_1[c]	$p\ (CO_2)$[a]	$[CO_2]$[b]	k_1[c]	$p\ (CO_2)$[a]	$[CO_2]$[b]	k_1[c]
2	4.16E19	4.2	8	1.69E20	5.1	30	6.83E20	7.0
5	1.05E20	4.5	10	2.13E20	4.4	40	9.44E20	7.8
7	1.48E20	4.8	20	4.40E20	5.6			

(c) M = CO_2 at 400 K

$p\ (CO_2)$[a]	$[CO_2]$[b]	k_1[c]	$p\ (CO_2)$[a]	$[CO_2]$[b]	k_1[c]	$p\ (CO_2)$[a]	$[CO_2]$[b]	k_1[c]
2	3.63E19	4.3	8	1.47E20	4.4	40	7.81E20	5.0
4	7.29E19	4.2	20	3.76E20	4.6			
6	1.10E20	4.0	30	5.74E20	5.7			

[a] Pressure of the bath gas, given in bar.   [b] Density of the bath gas, given in molecule cm^{-3}.

[c] Rate constant, given in 10^{-11} cm^3 $molecule^{-1}$ s^{-1}.

3.2 Recombination reaction of *p*-methylbenzyl radicals

p-Methylbenzyl radical was selected to determine if there is also an enhancement of recombination rate constants k_1 at high pressures in slightly larger alkyl-substituted systems.

$$p\text{-}CH_3C_6H_4CH_2 \quad + \quad p\text{-}CH_3C_6H_4CH_2 \quad \rightarrow \quad C_{16}H_{18} \quad k_1 \qquad (3.2.1)$$

The rate constants of the combination reaction, k_1, have been measured over the pressure range 2–200 bar and the temperature range 300–515 K. Helium, argon, and CO_2 were used as the bath gas (M). *p*-Methylbenzyl radicals have been widely used in reactions to study para-substituent effects on the reaction of benzyl radical: Tokumura *et al.* investigated the oxygenation reaction rates of benzyl and *p*-methylbenzyl radical in solution by using the UV absorption technique.[36] However, no direct measurement of reaction (3.2.1) in the gas phase has been conducted so far. There are numerous spectroscopic studies of *p*-methylbenzyl radical in the UV and visible range. The doublet-doublet fluorescence of benzyl radicals, *p*-methylbenzyl, and *p*-chlorobenzyl radicals in solution were detected and the substituent effect was studied.[37] The absorption band of *p*-methylbenzyl radicals in the UV region was measured and the spectral features of *p*-xylene, and the *p*-methylbenzyl radical were not quite different from those of toluene and benzyl radicals.[51-54] However, as these measurements were done at high temperatures of over 1000 K, no direct study of the absorption band of *p*-methylbenzyl radicals in the UV region at room temperature is available.

We present the first direct measurement of the recombination reaction of *p*-methylbenzyl radicals in the gas-phase at room temperature. In the following section, the experimental method is briefly described and the experimental results of recombination rate constants for *p*-methylbenzyl radicals are presented. Also the transient UV absorption spectrum of *p*-methylbenzyl radicals and their absorption coefficient ($\sigma_{p\text{-methylbenzyl}}$) at room temperature were determined.

In the present work, the recombination rate constants of *p*-methylbenzyl radicals have been investigated by directly monitoring the absorption signal of the *p*-methylbenzyl radical.

$$Cl_2 \quad + \quad h\nu \quad \rightarrow \quad 2\ Cl \qquad\qquad (3.2.2)$$

$$Cl \quad + \quad p\text{-}CH_3C_6H_4CH_3 \quad \rightarrow \quad p\text{-}CH_3C_6H_4CH_2 \quad + \quad HCl \qquad (3.2.3)$$

p-Methylbenzyl radicals were generated via reactions (3.2.2) and (3.2.3) following excimer laser flash photolysis similarly to the case of *p*-fluorobenzyl radicals. *p*-Xylene was used as a precursor for *p*-methylbenzyl radical. The reagent grade *p*-xylene was obtained from Aldrich, and was purified in a pump-thaw-freezing cycle prior to use. Reaction (3.2.3) is known to solely proceed through a fast H-atom abstraction channel. The reported rate constant for reaction 3.2.3 is $13.3 \times 10^{-11} cm^3 molecule^{-1} s^{-1}$, [55] or $15 \pm 0.1 \times 10^{-11} cm^3 molecule^{-1} s^{-1}$, [56] which is about twice as large as $k(Cl + toluene) = 6 \times 10^{-11} cm^3 molecule^{-1} s^{-1}$. [27]

Initial mixtures ranging from $[Cl]_0 = (0.8 - 3.6) \times 10^{14}$ molecule cm^{-3} and $[p\text{-xylene}] = (0.5 - 1.3) \times 10^{17}$ molecule cm^{-3} were prepared with the target bath gas. The experiments were carried out in a temperature-controlled heatable high-pressure optical cell. Based on the benzyl and *p*-fluorobenzyl radical experiments, the rate constants below 1 bar were not measured on assumption that the rate constants below 1 bar are constant and similar to that of 2 bar. Since only the heatable high-pressure cell was used, the temperature dependence of the enhancement of the rate constant was investigated in the high temperature range above 400 K instead of low temperatures. The absorption coefficients of the *p*-methylbenzyl radical at the desired wavelength and temperature were not known. To determine $\sigma_{p\text{-methylbenzyl}}$, two mixtures with the same initial concentration of Cl_2 and precursors (toluene and *p*-xylene) were prepared separately, and the absorption-time profiles were measured under the same conditions. Finally, comparing the differences in the absorption signals, the absorption coefficient of *p*-methylbenzyl radical, based on that of benzyl radical, could be calibrated.

3.2.1 Transient absorption spectrum of *p*-methylbenzyl radical

The spectral features of the *p*-methylbenzyl radical were similar to those of benzyl radicals, but the wavelength, where the maximum absorption λ_{max} of *p*-methylbenzyl radicals was observed at 300 K, was shifted by about 10 nm to longer wavelength, compared to benzyl radical. [1,7]
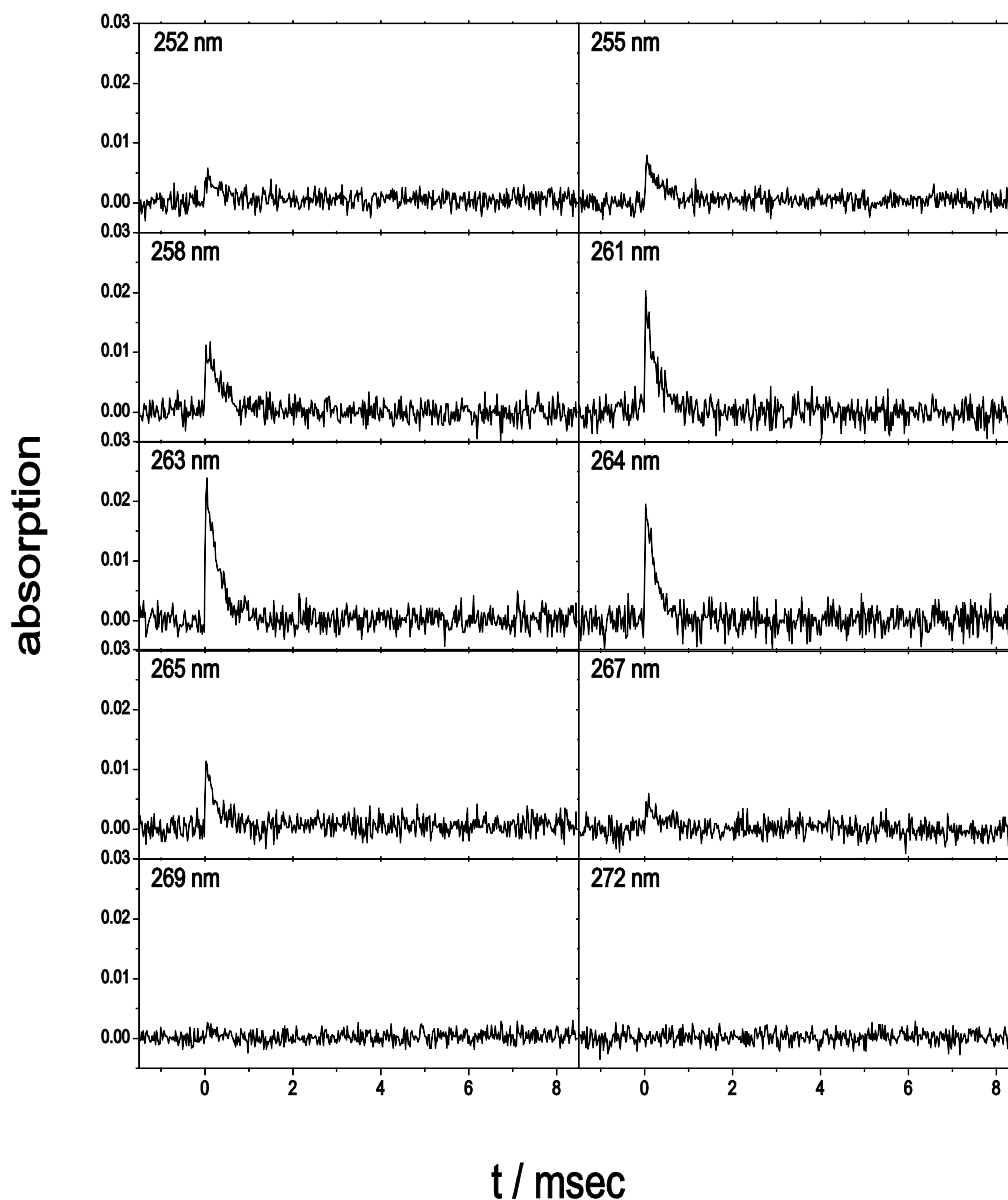
Figure 3.2.1 Transient absorption signals of p-methylbenzyl radicals observed at different probe wavelengths. Initial conditions: $[Cl_2]$ = 1.1 mbar, $[p\text{-xylene}]$ = 2.8 mbar, in 11 bar He. λ_{pump} = 308 nm (155 mJ). The ratio $[Cl_2]$ / $[p\text{-xylene}]$ = 0.4 was kept constant.

Before determining an accurate $\sigma_{p\text{-methylbenzyl}}$ value, the detection wavelength should be selected because the $\sigma_{p\text{-methylbenzyl}}$ at 253 nm is not large enough for the experiment. Therefore, absorption-time profiles of p-methylbenzyl radicals were measured at different detection wavelengths between 245 and 272 nm at 300 K.

In Figure 3.2.1 the absorption signals of the p-methylbenzyl radical measured at 10 different wavelengths are summarized. $[Cl_2]$ = 1.2 mbar and $[p\text{-xylene}]$ = 3 mbar were used

and the measurements were conducted in 12 bar He. As the absorption coefficients of *p*-methylbenzyl radicals, $\sigma_{p\text{-methylbenzyl}}$, were not known at different detection wavelengths between 245 and 272 nm at 300 K, the absorption-time profiles of *p*-methylbenzyl radicals were fitted with the σ_{benzyl} at the wavelength. To determine the error range, the maximum and minimum values in the time interval, where we averaged, were selected. As the signal intensity is strongly dependent on the laser energy and lamp intensity, the Abs_{max} values were corrected with these two factors. Figure 3.2.2 represents the resulting *p*-methylbenzyl radical spectrum at 300 K. The Abs_{max} values were normalized with the value at 263 nm. For comparison, the absorption spectrum of *p*-xylene was also measured and is also shown in the Figure 3.2.2.
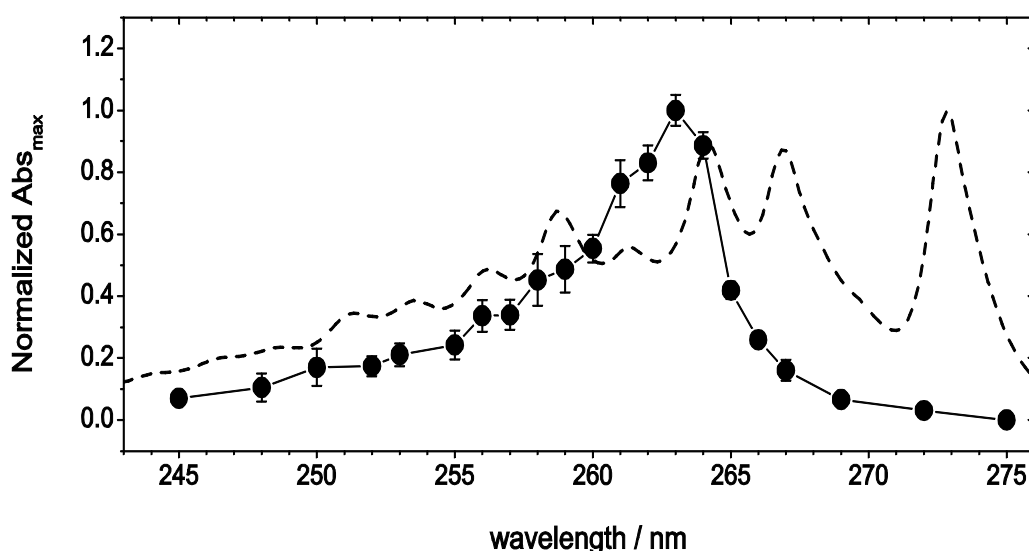
Figure 3.2.2 Transient absorption spectrum of *p*-methylbenzyl radicals (-•-) in [Cl₂] = 1.1 mbar, [*p*-xylene] = 3 mbar and 12 bar He and of 5 mbar *p*-xylene(---). A gas-cell with a 10 cm path length was used to measure the absorption spectrum of *p*-xylene at 300 K.

An almost structureless absorption band was obtained, and the maximum absorption was located at ca. 263 nm. Like for *p*-fluorobenzyl radicals, the exact $\sigma_{p\text{-methylbenzyl}}$ was not known. The same method used to determine the $\sigma_{p\text{-fluorobenzyl}}$ was used, but unlike in the case of *p*-fluorobenzyl radical, a single $\sigma_{p\text{-methylbenzyl}}$ at 253 nm was not sufficient for a reliable determination. Therefore, the transient absorption signals of benzyl radicals and *p*-methylbenzyl radicals were measured at 255 nm, 257 nm and 258 nm under various experimental conditions. Figure 3.2.3 shows the transient absorption signals of benzyl and *p*-methylbenzyl radicals at 257 nm. For comparison, the same initial concentration of Cl$_2$ and the same concentrations of toluene and *p*-xylene were used.
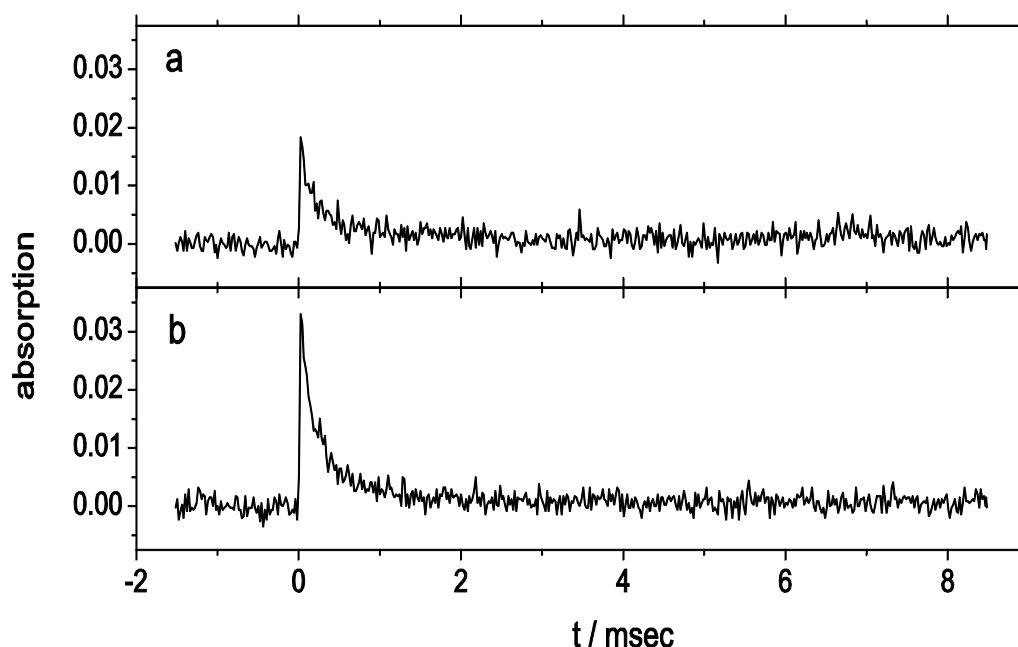
Figure 3.2.3   Typical transient absorption signals of (a) benzyl and (b) *p*-methylbenzyl radicals at 257 nm, recorded after photolysis at 308 nm of mixtures with the same initial concentration (0.28 mbar Cl$_2$, 0.93 mbar of toluene and *p*-xylene, and 7 bar He at 300 K).

As a scattering of the data around the maximum value exists, a narrow range of data was averaged to determine absorption maxima, a_0 value. Before determining $\sigma_{p\text{-methylbenzyl}}$, the flow rate effect on a_0 was investigated and the results are represented in Figure 3.2.4.
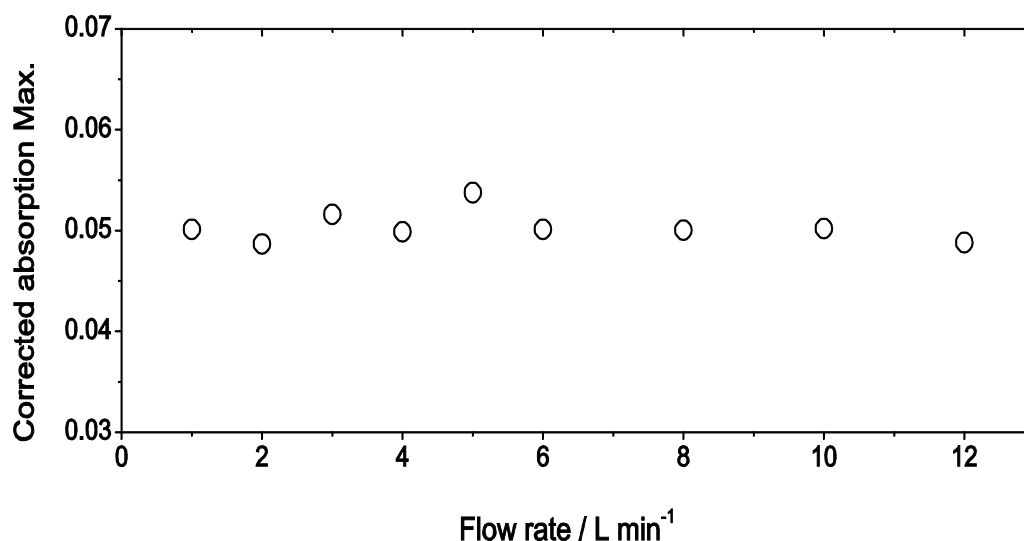
Figure 3.2.4 Flow rate dependence of absorption signal of p-methylbenzyl radicals. Experimental conditions: 0.28 mbar Cl_2, 0.84 mbar p-xylene and 7 bar He. $\lambda_{detection} = 260$ nm and the absorption maxima (Abs_{max}) values were corrected with the laser and the lamp intensity.

Figure 3.2.4 shows that the absorption maximum values are insensitive to the flow rate under our experimental conditions. From the comparison of a_0(p-methylbenzyl) and a_0(benzyl), the ratio was determined under different experimental conditions. The ratio, a_0(p-methylbenzyl) / a_0(benzyl) and the experimentally determined $\sigma_{p\text{-methylbenzyl}}$ at 255 nm, 257 nm and 258 nm are summarized in Table 3.2.1. Also $\sigma_{p\text{-methylbenzyl}}$ at 260 nm, determined by using the a_0 ratio of p-methylbenzyl and benzyl and the normalized Abs_{max}, represented in Figure 3.2.2, is summarized.

Table 3.2.1 Experimentally determined $\sigma_{p\text{-methylbenzyl}}$.

$\lambda_{detection}$/ nm	a_0(p-methylbenzyl) / a_0(benzyl)	σ_{benzyl} at $\lambda_{detection}$ [a]	$\sigma_{p\text{-methylbenzyl}}$ at $\lambda_{detection}$ [a]	$\sigma_{p\text{-methylbenzyl}}$ at 260 nm [a]
255	0.40	5.40E-17	2.17E-17	4.95E-17
257	1.70	1.93E-17	3.28E-17	5.35E-17
257	1.63	1.93E-17	3.14E-17	5.13E-17
258	3.66	1.10E-17	4.02E-17	4.92E-17
258	3.66	1.10E-17	4.02E-17	4.92E-17

[a] absorption coefficient, given in cm^2 molecule^{-1}
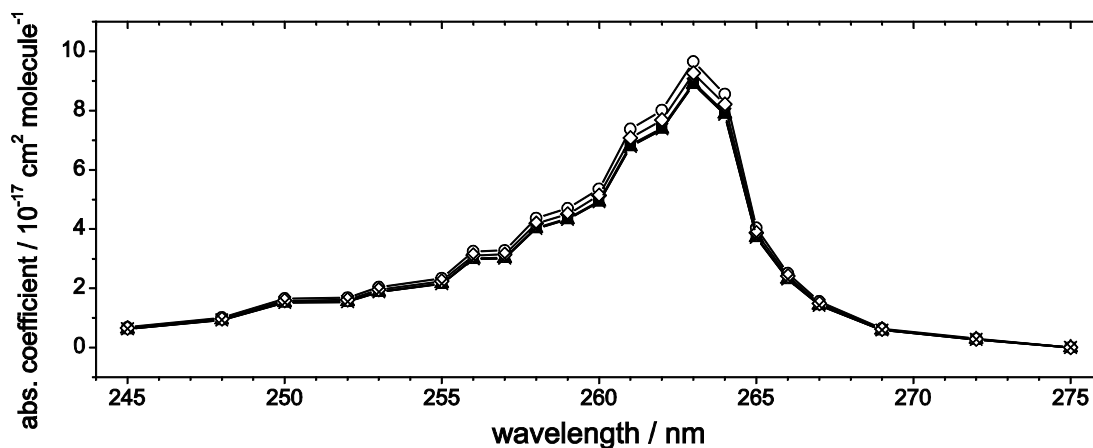
Figure 3.2.5   Absorption spectrum of *p*-methylbenzyl radicals obtained under different experimental conditions. (■) : 0.16 mbar Cl_2, 0.53 mbar *p*-xylene and 4 bar He, with the same concentration ratio 5 and 7 bar He, $\lambda_{detection}$ = 255 nm; (○) : 0.16 mbar Cl_2, 0.53 mbar *p*-xylene and 4 bar He, with the same concentration ratio 5 and 7 bar He, $\lambda_{detection}$ = 257 nm; (▲) : 0.16 mbar Cl_2, 0.53 mbar *p*-xylene and 4 bar He, with the same concentration ratio 5 and 7 bar He, $\lambda_{detection}$ = 258 nm; (◊) : 0.28 mbar Cl_2, 0.93 mbar p-xylene and 7 bar He, with the same concentration ratio 9 bar He, $\lambda_{detection}$ = 257 nm; (×) : 0.28 mbar Cl_2, 0.93 mbar *p*-xylene and 7 bar He with the same concentration ratio 9 bar He, $\lambda_{detection}$ = 258 nm.
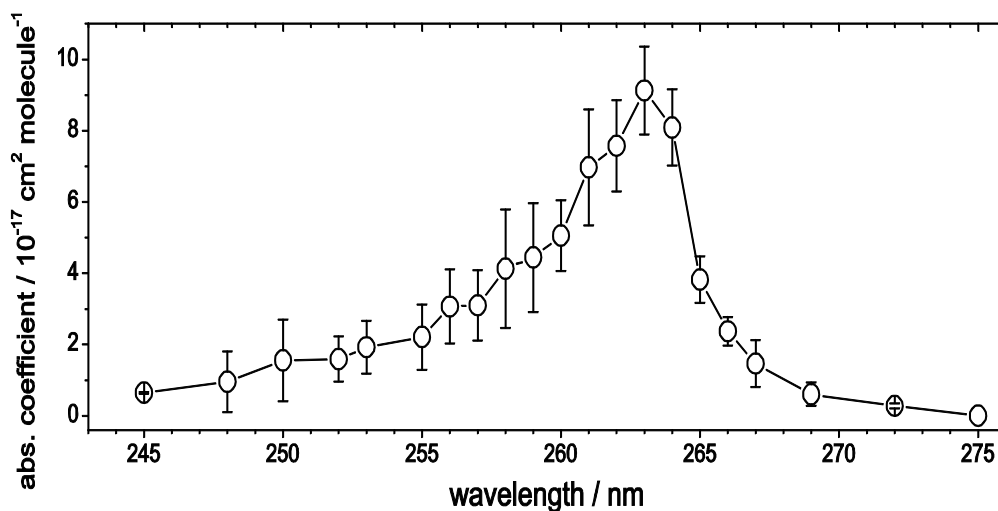
Figure 3.2.6   Transient absorption spectrum of *p*-methylbenzyl radicals at 300 K, see text.

Figure 3.2.5 shows the individual spectra of *p*-methylbenzyl radicals, obtained at different detection wavelengths and the resulting $\sigma_{p\text{-methylbenzyl}}$ (λ, 300 K) is shown in Figure 3.2.6. The $\sigma_{p\text{-methylbenzyl}}$ for the same wavelength was determined by averaging the $\sigma_{p\text{-methylbenzyl}}$ values in Figure 3.2.5. Error bars indicate the statistical errors from Figure 3.2.5 and from Figure 3.2.2 due to the data scattering. Based on Figures 3.2.5 and 3.2.6, as the $\sigma_{p\text{-methylbenzyl}}$ at 253 nm is small, less than 2.0×10^{-17} cm^2 molecule^{-1}, experiments were therefore carried out at 260 nm as the detection wavelength for *p*-methylbenzyl radical to achieve sufficient signal intensity. For this, $\sigma_{p\text{-methylbenzyl}}$ (260 nm, 300 K) = 5.0×10^{-17} cm^2 molecule^{-1} was obtained.

3.2.2 Pressure- and temperature-dependent absorption coefficient of *p*-methylbenzyl radicals.

The measured reaction rates are sensitive to the absorption coefficients of $\sigma_{p\text{-methylbenzyl}}$. As $\sigma_{p\text{-methylbenzyl}}$ depends on the temperature, it is essential to determine the temperature (T)- and pressure (P)-dependent values of $\sigma_{p\text{-methylbenzyl}}$ (P, T). First, $\sigma_{p\text{-methylbenzyl}}$ (P, 300 K) was investigated under various experimental conditions in CO_2 at 300 K and the results are shown in Figure 3.2.7. The Abs$_{max}$ values were corrected with the laser and lamp intensity and then corrected with the initial Cl_2 concentration. The dashed-line is a linear fit considering all data points (y = 0.31795 – 3.066E-4 $\cdot$ x). An insignificant slope indicates that $\sigma_{p\text{-methylbenzyl}}$ (P, 300 K) at 260 nm is almost independent of pressure in this range.

In Figure 3.2.8, the absorption coefficients of *p*-methylbenzyl radicals at 260 nm were measured at different temperatures between 300 and 515 K. $\sigma_{p\text{-methylbenzyl}}$ at 260 nm showed only a weak dependence in this temperature range. The solid line in Figure 3.2.8 (b) represents a fit, where the weak temperature dependence of $\sigma_{p\text{-methylbenzyl}}$ over the temperatures 300–515 K is expressed as:

$$\sigma_{p-methylbenzyl}(260\,\text{nm}) = (5.0 \pm 0.98) \times 10^{-17} (\frac{T}{300\text{K}})^{-0.234}\,\text{cm}^2\text{molecule}^{-1} \qquad (3.2.4)$$
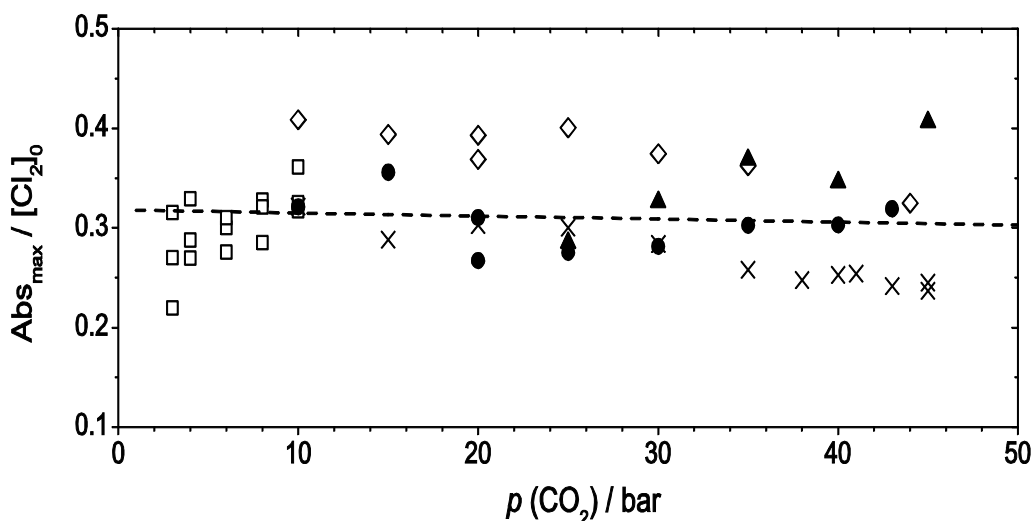
Figure 3.2.7   Pressure dependence of the absorption intensity of *p*-methylbenzyl radicals in CO_2 at 260 nm under different experimental initial conditions. (□) : 0.09 mbar Cl_2, 0.36 mbar *p*-xylene and 3 bar CO_2 with the same concentration ratio up to 10 bar CO_2 (taken on 14.03.2007); (●) : 0.10 mbar Cl_2, 0.40 mbar *p*-xylene and 10 bar CO_2 with the same concentration ratio up to 44 bar CO_2 (taken on 15.03.2007); (×): 0.11 mbar Cl_2, 0.44 mbar *p*-xylene and 10 bar CO_2 with the same concentration ratio up to 45 bar CO_2 (taken on 16.03.2007); (◊) : 0.12 mbar Cl_2, 0.48 mbar *p*-xylene and 10 bar CO_2 with the same concentration ratio up to 45 bar CO_2 (taken on 27.03.2007); (▲) : 0.25 mbar Cl_2, 1.00 mbar *p*-xylene and 25 bar CO_2 with the same concentration ratio up to 45 bar CO_2 (taken on 30.03.2007). The dashed line is a linear fit (see text).
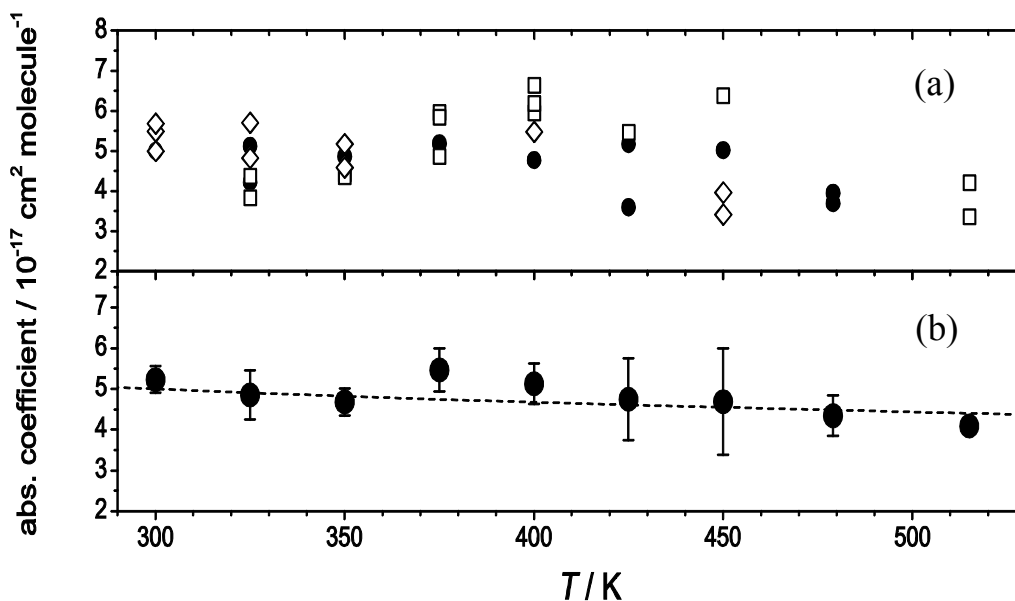
Figure 3.2.8   Temperature dependence of the absorption coefficient $\sigma_{p\text{-methylbenzyl}}$ at 260 nm. (a) : Data obtained under different experimental conditions. (●) : 0.62 mbar Cl_2, 1.25 mbar *p*-xylene and 20 bar CO_2 at 300 K and with the same concentration ratio up to 479 K; (◊) : 0.67 mbar Cl_2, 1.33 mbar *p*-xylene and 20 bar CO_2 at 300 K and with the same concentration ratio up to 450 K; (□) : 0.62 mbar Cl_2, 1.25 mbar *p*-xylene and 5 bar He at 300 K and with the same concentration ratio up to 515 K, (b) : averaged absorption coefficients of *p*-methylbenzyl radical at each temperature. Line indicates the linear fit (see text).

59

3.2.3 Typical absorption signals at 260 nm

p-Methylbenzyl radicals were generated through reaction (3.2.2) and (3.2.3). It is generally found that the probability of photolytic bond fission is greatest at the weakest bond in a molecule. A large difference between the rates of reaction of atomic chlorine with benzene and toluene was observed. The rates of the same reactions with p-xylene are more than twice that of toluene, $k(\text{Cl} + \text{toluene}) = 5.9 \times 10^{-11}$ cm^3 molecule^{-1} s^{-1} and $k(\text{Cl} + p\text{-xylene}) = 1.5 \times 10^{-10}$ cm^3 molecule^{-1} s^{-1}.[56] It can be suggested that the reaction of chlorine atoms with these substituted aromatics, such as toluene and p-xylene, proceed through a mechanism involving hydrogen abstraction from the alkyl groups, not from the aromatic ring itself. The product radical, generated through reaction 3.2.2 and 3.2.3, is definitely a xylyl radical. Figure 3.2.9 shows the typical absorption signal at 260 nm, recorded after the 308 nm-laser photolysis of Cl$_2$ in the presence of p-xylene and He bath gas of 8 bar at 300 K. The signal shows the instant increase in radical concentration, which then is followed by second-order decay. The fit did not show any systematic deviations.
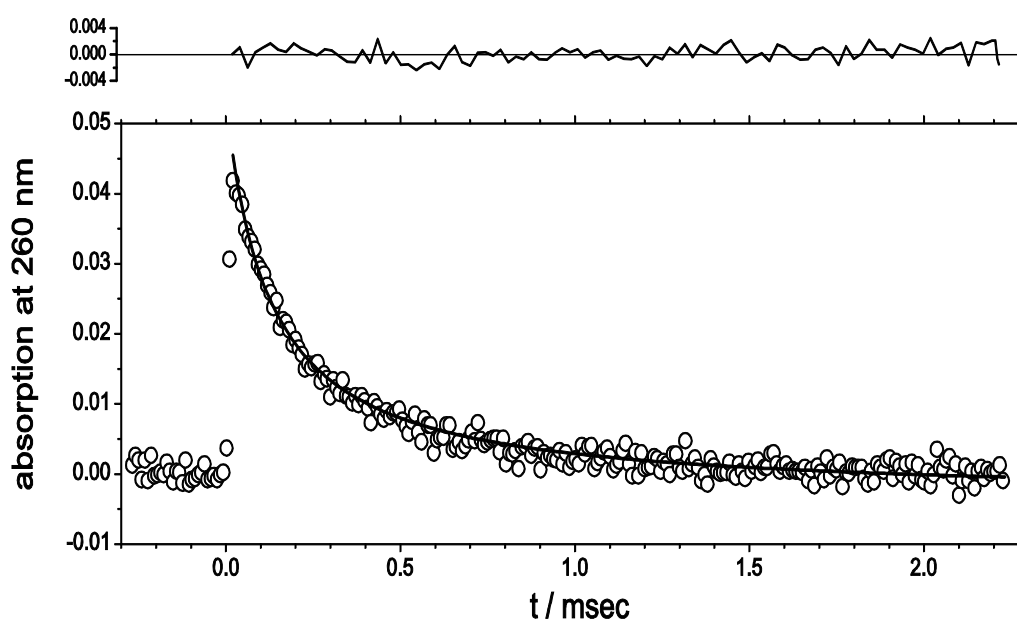
Figure 3.2.9 Typical transient absorption signal of p-methylbenzyl radicals at 260 nm, recorded after the photolysis at 308 nm of mixtures of 0.31 mbar of Cl$_2$, 1.23 mbar of p-xylene and 8 bar CO$_2$ at 300 K. Upper figure is the fit residual.

3.2.4 Pressure and temperature dependence of the rate constant k_1

The experimental results for the pressure dependence of k_1 at 300 K in helium are shown in Figure 3.2.10 and in argon in Figure 3.2.11. Figure 3.2.12 presents the experimental results for the pressure dependence of k_1 at 300 K in CO_2. The results on the pressure dependence of k_1 obtained at 300 K for the bath gases helium, argon and CO_2 are given in Table 3.2.2 and Figure 3.2.13.
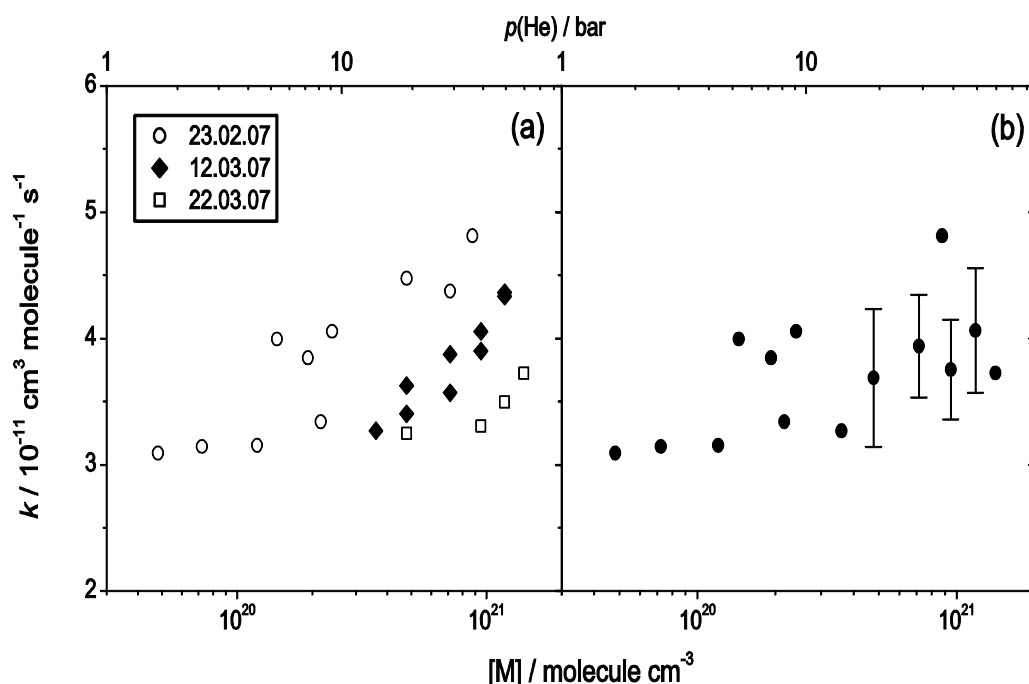
Figure 3.2.10 Recombination rate constant k_1 in He in the pressure range 2 – 60 bar at 300 K. (a) Data obtained under different experimental conditions, ($\circ$) : 0.07 mbar Cl_2, 0.27 mbar p-xylene and 2 bar He at 300 K and with the same concentration ratio up to 37 bar; ($\blacklozenge$) : 0.12 mbar Cl_2, 0.40 mbar p-xylene and 20 bar He at 300K and with the same concentration ratio up to 50 bar; ($\square$) : 0.12 mbar Cl_2, 0.40 mbar p-xylene and 20 bar He at 300 K and with the same concentration ratio up to 60 bar, (b) Average k_1 values obtained from Figure 3.2.10 (a) for the same densities. Error bars indicate the statistical errors for selected points.
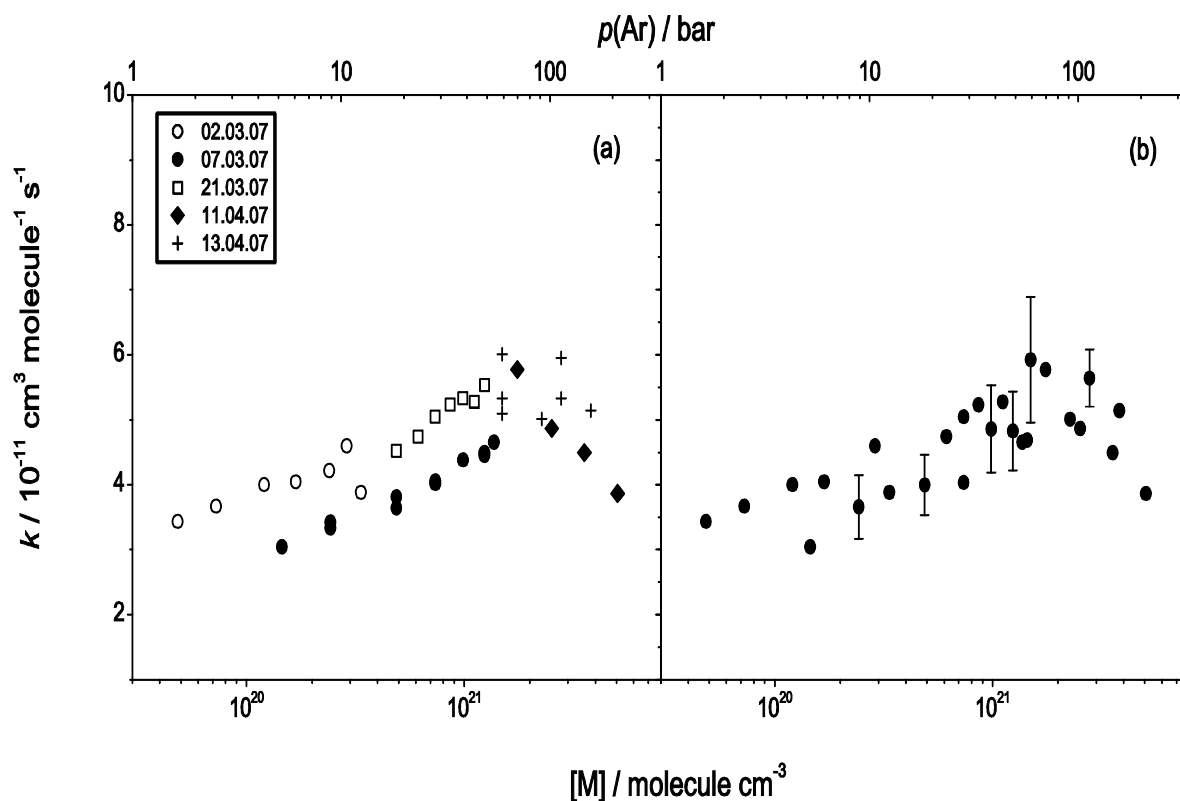
Figure 3.2.11 Recombination rate constant k_1 in Ar in the pressure range 2 - 200 bar at 300 K. (a) Data obtained under different experimental conditions, ($\circ$) : 0.07 mbar Cl_2, 0.27 mbar p-xylene and 2 bar Ar at 300 K and with the same concentration ratio up to 14 bar; ($\bullet$) : 0.20 mbar Cl2, 0.80 mbar p-xylene and 6 bar Ar at 300 K and with the same concentration ratio up to 58 bar; ($\square$) : 0.08 mbar Cl_2, 0.32 mbar p-xylene and 8 bar Ar at 300 K and with the same concentration ratio up to 50 bar; ($\blacklozenge$) : 0.90 mbar Cl_2, 2.70 mbar p-xylene and 70 bar Ar at 300 K and with the same concentration ratio up to 200 bar; (+) : 0.25 mbar Cl_2, 1.71 mbar p-xylene and 60 bar Ar at 300 K and with the same concentration ratio up to 150 bar, (b) Average k_1 values deduced from Figure 3.2.11 (a) for the same densities. Error bars indicate the statistical error for selected points.
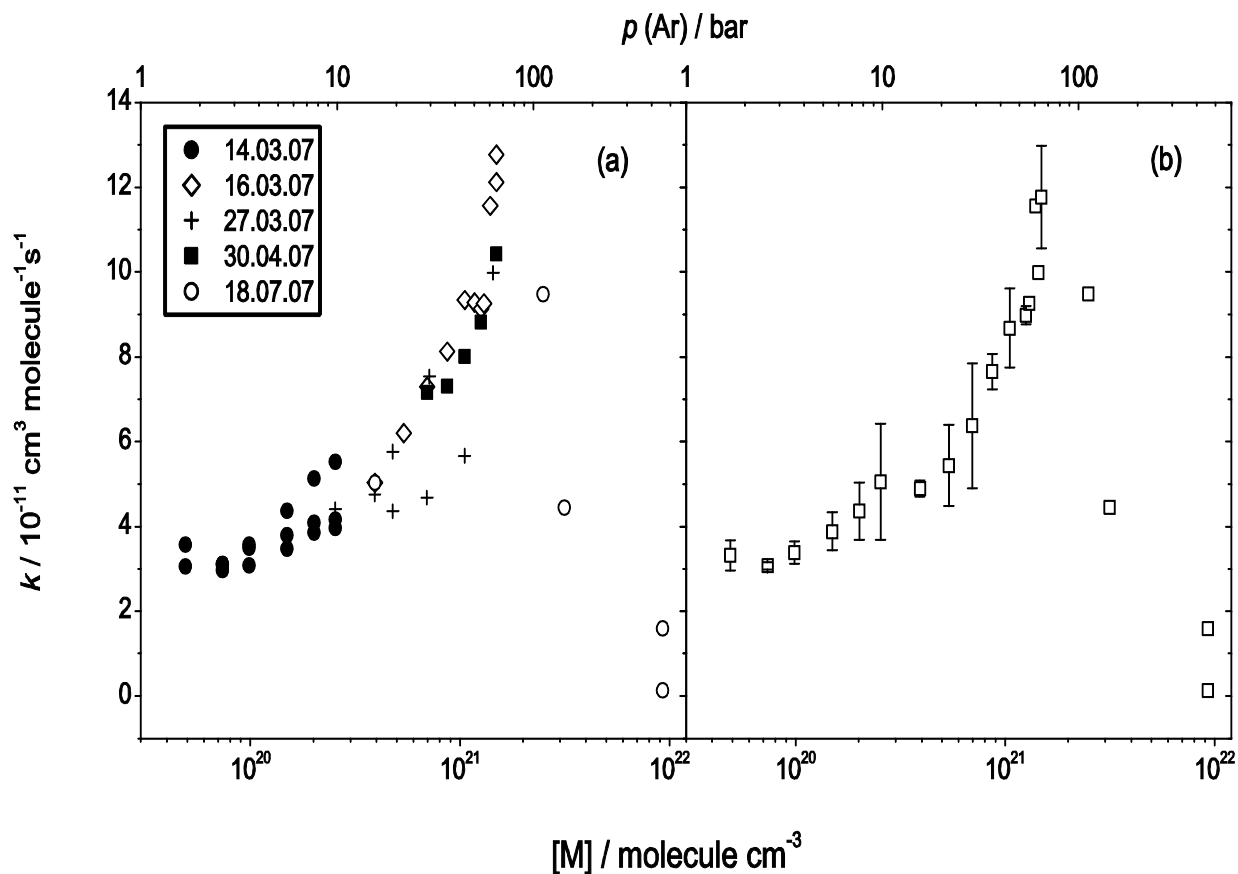
Figure 3.2.12 Recombination rate constant k_1 in CO_2 for the pressure range 2–67 bar at 300 K. (a) Data obtained under different experimental conditions, ($\bullet$) : 0.06 mbar Cl_2, 0.17 mbar p-xylene and 2 bar CO_2 at 300 K and with the same concentration ratio up to 10 bar; ($\Diamond$) : 0.10 mbar Cl_2, 0.40 mbar p-xylene and 10 bar CO_2 at 300 K and with the same concentration ratio up to 45 bar; (+) : 0.12 mbar Cl_2, 0.36 mbar p-xylene and 10 bar CO_2 at 300 K and with the same concentration ratio up to 44 bar; ($\blacksquare$) : 0.30 mbar Cl_2, 0.90 mbar p-xylene and 25 bar CO_2 at 300 K and with the same concentration ratio up to 45 bar; ($\circ$) : 1.00 mbar Cl_2, 3.00 mbar p-xylene and 60 bar CO_2 at 300 K and with the same concentration ratio up to 67 bar, (b) Average k_1 values from Figure 3.2.12 (a) for the same densities. Error bars indicate the statistical error for selected points.
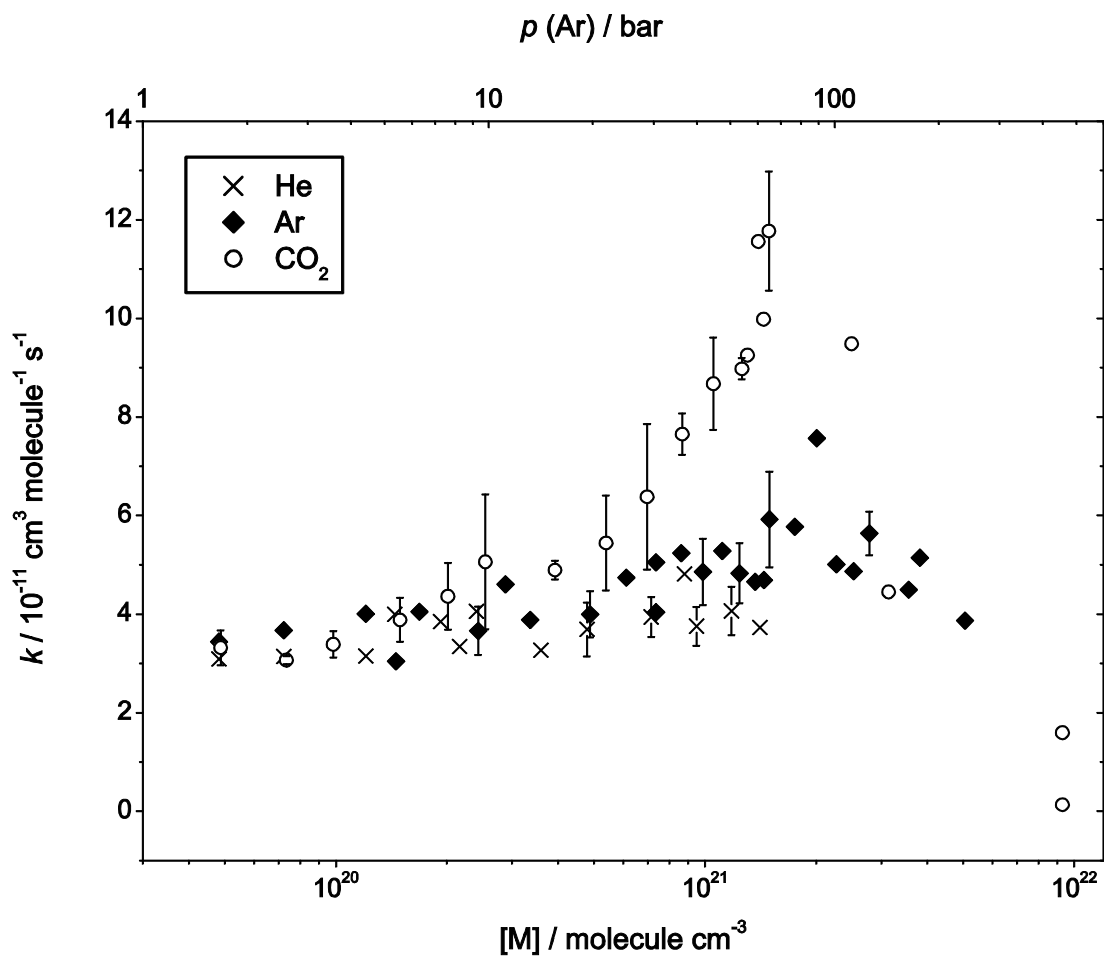
Figure 3.2.13 Density-dependent recombination rate constant k_1 of p-methylbenzyl radicals in He ($\times$), Ar ($\blacklozenge$) and CO_2($\circ$) at 300 K.

Table 3.2.2 Rate constants for the recombination reaction of p-methylbenzyl radicals in helium, argon and CO_2 at 300 K.

(a) M = He at 300 K

| p (He)[a]	[He] [b]	k_1 [c]	p (He) [a]	[He] [b]	k_1 [c]	p (He) [a]	[He] [b]	k_1 [c]
2	4.82E19	3.1	20	4.78E20	4.5	40	9.48E20	3.9
3	7.23E19	3.1	20	4.78E20	3.6	40	9.48E20	4.1
5	1.20E20	3.2	20	4.78E20	3.4	40	9.48E20	3.3
6	1.44E20	4.0	20	4.78E20	3.3	50	1.18E21	4.4
8	1.92E20	3.9	30	7.14E20	4.4	50	1.18E21	4.3
9	2.16E20	3.3	30	7.14E20	3.6	50	1.18E21	3.5
10	2.40E20	4.1	30	7.14E20	3.9	60	1.41E21	3.7
15	3.60E20	3.3	37	8.78E20	4.8			

(b) M = Ar at 300 K

p (Ar)[a]	[Ar] [b]	k_1 [c]	p (Ar) [a]	[Ar] [b]	k_1 [c]	p (Ar) [a]	[Ar] [b]	k_1 [c]
2	4.82E19	3.4	25	6.12E20	4.7	60	1.49E21	7.3
3	7.23E19	3.7	30	7.37E20	4.0	60	1.49E21	6.0
5	1.20E20	4.0	30	7.37E20	4.1	60	1.49E21	5.1
6	1.45E20	3.0	30	7.37E20	5.1	60	1.49E21	5.3
7	1.68E20	4.1	35	8.62E20	5.2	70	1.75E21	5.8
10	2.43E20	4.2	40	9.87E20	5.3	90	2.27E21	5.0
10	2.43E20	3.3	40	9.87E20	4.4	100	2.53E21	4.9
10	2.43E20	3.4	45	1.11E21	5.3	110	2.78E21	6.0
12	2.88E20	4.6	50	1.24E21	5.5	110	2.78E21	5.3
14	3.36E20	3.9	50	1.24E21	4.5	140	3.56E21	4.5
20	4.88E20	4.5	50	1.24E21	4.5	150	3.82E21	5.1
20	4.88E20	3.8	55	1.37E21	4.7	200	5.06E21	3.9
20	4.88E20	3.6	58	1.44E21	4.7			

<div align="center">(c) M = CO_2 at 300 K</div>

p (CO_2) [a]	$[CO_2]$ [b]	k_1 [c]	p (CO_2) [a]	$[CO_2]$ [b]	k_1 [c]	p (CO_2) [a]	$[CO_2]$ [b]	k_1 [c]
2	4.87E19	3.1	10	2.54E20	5.5	35	1.05E21	9.3
2	4.87E19	3.6	10	2.54E20	4.4	35	1.05E21	8.0
3	7.35E19	3.1	10	2.54E20	3.6	40	1.26E21	8.8
3	7.35E19	3.0	10	2.54E20	7.2	40	1.26E21	9.1
3	7.35E19	3.1	10	2.54E20	6.5	41	1.30E21	9.3
4	9.85E19	3.1	15	3.92E20	4.8	43	1.39E21	11.6
4	9.85E19	3.5	15	3.92E20	5.0	44	1.44E21	10.0
4	9.85E19	3.6	20	5.39E20	6.2	45	1.49E21	10.4
6	1.49E20	3.5	20	5.39E20	5.8	45	1.49E21	12.8
6	1.49E20	3.8	20	5.39E20	4.4	45	1.49E21	12.1
6	1.49E20	4.4	25	6.97E20	7.2	60	2.49E21	9.5
8	2.01E20	3.9	25	6.97E20	4.7	65	3.14E21	4.5
8	2.01E20	4.1	25	6.97E20	7.3	67	9.29E21	0.13
8	2.01E20	5.1	30	8.67E20	7.5	67	9.29E21	1.60
10	2.54E20	4.0	30	8.67E20	7.3			
10	2.54E20	4.2	30	8.67E20	8.1			

[a] Pressure of the bath gas, given in bar. [b] Density of the bath gas, given in molecule cm^{-3}. [c] Rate constant, given in 10^{-11} cm^3 $molecule^{-1}$ s^{-1}.

As for benzyl and p-fluorobenzyl radicals, k_1 values are almost identical around 2 bar and independent of the bath gas. Assuming that pressure- and bath-gas-independent rate constant values of k_1 are observed below 1 bar, the limiting "high-pressure" rate constants of the Energy-Transfer mechanism, $k_{1,\infty}^{ET}(300K) = (3.29 \pm 0.25) \times 10^{-11} cm^3 molecule^{-1} s^{-1}$, could be derived from considering k_1 values at the lowest pressure measured in each bath gas. At pressures above 8 bar, clear indications of a further increase in k_1 were recognized in CO_2 (see Figure 3.2.13). The rate constant gradually increased until it slowed at densities where the influence of diffusion control should be considered. The final decrease in the rate constant at high pressures corresponded to a transition into the regime of diffusion-controlled kinetics. As seen in Figure 3.2.13, the pressure-induced enhancement of k_1 increases in the order He < Ar < CO_2, similar to that observed in the experiments on combination reactions of benzyl radicals[10] and p-fluorobenzyl radicals.[11]

The temperature dependence of $k_{1,\infty}^{ET}$ was investigated. First, the dependence was measured in helium at 5 bar over the temperature range 300–515 K, and the results are represented in Figure 3.2.14 and summarized in Table 3.2.3.
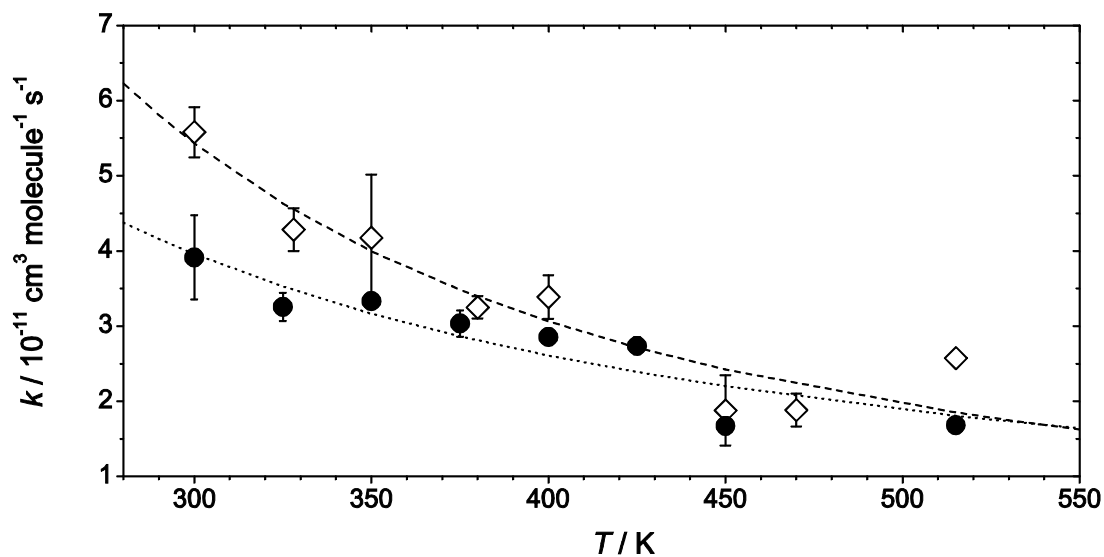
Figure 3.2.14   Temperature dependence of k_1 near 5 bar helium (●) and near 20 bar CO_2 (◊). Dashed and dotted lines indicate the fit with eqn. 3.2.5. Fit results are given in the text (see text).

Table 3.2.3   Rate constants for the combination reaction of *p*-methylbenzyl radicals in helium and CO_2 at various temperatures.

(a) M = He (5 bar) at 300 K

T/K	[M] [a]	k_1 [b]	T/K	[M] [a]	k_1 [b]	T/K	[M] [a]	k_1 [b]
300	1.20E20	4.0	350	1.20E20	3.2	425	1.20E20	2.9
300	1.20E20	3.7	375	1.20E20	2.9	425	1.20E20	2.7
325	1.20E20	3.2	375	1.20E20	3.0	425	1.20E20	2.8
325	1.20E20	3.3	375	1.20E20	3.1	450	1.20E20	1.6
325	1.20E20	3.6	400	1.20E20	2.9	450	1.20E20	1.8
350	1.20E20	3.2	400	1.20E20	2.9	515	1.20E20	1.7
350	1.20E20	3.1	400	1.20E20	2.9			

(b) M = CO_2 (20 bar) at 300 K

T/K	[M] [a]	k_1 [b]	T/K	[M] [a]	k_1 [b]	T/K	[M] [a]	k_1 [b]
300	5.39E20	5.5	350	5.39E20	5.1	400	5.39E20	3.4
300	5.39E20	5.9	350	5.39E20	3.6	450	5.39E20	1.6
300	5.39E20	5.3	380	5.39E20	3.4	450	5.39E20	2.2
328	5.39E20	4.3	380	5.39E20	3.2	470	5.39E20	1.9
328	5.39E20	4.0	400	5.39E20	3.0	515	5.39E20	2.6
328	5.39E20	4.6	400	5.39E20	3.6			
350	5.39E20	3.8	400	5.39E20	3.5			

[a] Density of the bath gas, given in molecule cm^{-3}.   [b] Rate constant, given in 10^{-11} cm^3 $molecule^{-1}$ s^{-1}.

Also the temperature dependence of k_1 was observed in CO_2 (20 bar) and the results are shown in Figure 3.2.14. A modest negative temperature dependence of k_1 was observed in helium, but the enhancement of k_1 values was more pronounced in CO_2. Above 400 K, the k_1 values in CO_2 reached the same value as in helium. As the k_1 value in helium at 5 bar is almost the same as at 2 bar, based on the results in Figure 3.2.14, the temperature dependence of $k_{1,\infty}^{ET}$ could be determined. The equation used to fit the experimental results is

$$y = a[(\frac{T}{300K})^{-b} \bullet (\frac{T}{300K})^{-c}] \tag{3.2.5}$$

where T denotes the temperature, and a, b and c are fitting parameters. In the case of the experiments with 5 bar helium, the fitting parameters c should be zero. In contrast, b are shared to fit the experimental results in CO_2 (20 bar). The resulting temperature dependence of $k_{1,\infty}^{ET}$ in helium over the temperature range $300 - 515$ K is expressed as:

$$k_{1,\infty}^{ET} = (3.96 \times 10^{-11})(\frac{T}{300K})^{-1.45} cm^3 molecule^{-1} s^{-1} \tag{3.2.6}$$

For CO_2 measurements, one obtains

$$k_1 = (5.44 \times 10^{-11})[(\frac{T}{300K})^{-1.45} \cdot (\frac{T}{300K})^{-0.54}] cm^3 molecule^{-1} s^{-1} \tag{3.2.7}$$
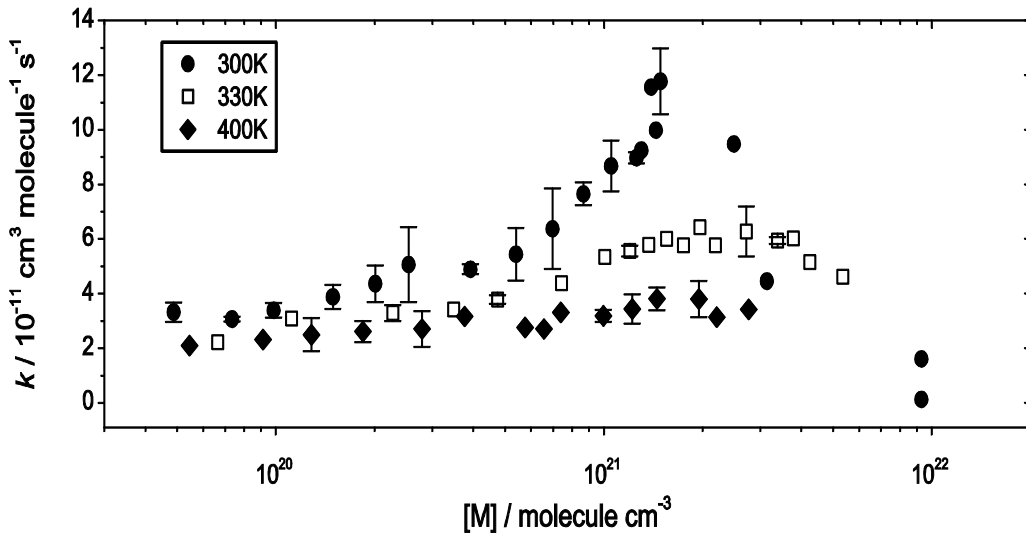

Figure 3.2.15   Density-dependent recombination rate constant k in CO_2 at different temperatures.   (●) : 300 K, (□) : 330 K and (♦) : 400 K.

The temperature dependence of k_1 over the full pressure range was investigated in CO_2 as bath gas at 300, 330, and 400 K. The results are shown in Figure 3.2.15 and summarized in Table 3.2.4.

Table 3.2.4   Rate constants for the combination reaction of *p*-methylbenzyl radicals in CO_2 at 300, 330 and 400 K.

(a) M = CO_2 at 330 K

p (CO_2)[a]	[CO_2] [b]	k_1 [c]	p (CO_2) [a]	[CO_2] [b]	k_1 [c]	p (CO_2) [a]	[CO_2] [b]	k_1 [c]
3	6.65E19	2.21	30	7.43E20	4.38	70	2.19E21	5.77
5	1.12E20	3.09	39	1.01E21	5.34	80	2.72E21	6.92
5.62	2.28E20	3.08	45	1.20E21	5.70	80	2.72E21	5.62
10	2.28E20	3.50	50	1.37E21	5.78	90	3.38E21	5.95
15	3.48E20	3.43	55	1.55E21	6.0	95	3.78E21	6.03
20	4.74E20	3.90	60	1.75E21	5.77	100	4.24E21	5.16
20	4.74E20	3.68	65	1.96E21	6.43	110	5.34E21	4.62

(b) M = CO_2 at 400 K

p (CO_2)[a]	[CO_2] [b]	k_1 [c]	p (CO_2) [a]	[CO_2] [b]	k_1 [c]	p (CO_2) [a]	[CO_2] [b]	k_1 [c]
3	5.46E19	2.10	30	5.74E20	2.76	70	1.45E21	3.74
5	9.13E19	2.32	34	6.56E20	2.70	70	1.45E21	4.27
7	1.28E20	1.59	38	7.39E20	3.31	70	1.45E21	3.27
7	1.28E20	2.85	50	9.96E20	3.21	70	1.45E21	3.95
7	1.28E20	2.82	50	9.96E20	3.39	90	1.95E21	4.51
7	1.28E20	2.73	50	9.96E20	2.94	90	1.95E21	3.69
10	1.84E20	2.05	60	1.22E21	2.80	90	1.95E21	3.20
15	2.79E20	2.24	60	1.22E21	3.94	100	2.21E21	3.14
15	2.79E20	3.17	60	1.22E21	3.21	120	2.76E21	3.43
20	3.76E20	3.16	60	1.22E21	3.81			

[a] Pressure of the bath gas, given in bar. [b] Density of the bath gas, given in molecule cm^{-3}.
[c] Rate constant, given in 10^{-11} cm^3 molecule^{-1} s^{-1}

As for benzyl and *p*-fluorobenzyl radicals, the lower the temperature, the more pronounced the enhancement of k_1. The strong negative temperature dependence of the contribution of the radical complex mechanism to k_1 was once again observed. In contrast, the role of the RC mechanism appears to be negligible at very high temperatures.

3.3   Recombination reaction of benzyl radicals

Even though indications for the RC mechanism have been found in several experimental studies on combination reactions of atoms and small radicals, it was difficult to quantify its exact contribution. The reason is that both the ET mechanism and the RC mechanism contribute simultaneously to the combination rate constant. Oum *et al.*[9,10] set an effective strategy to overcome this problem by investigating combination reactions of large organic radicals. The contribution of the RC mechanism to the combination rate constant k_1 was successfully interpreted and quantified by investigating the benzyl radical recombination reaction.

$$C_6H_5CH_2 \quad + \quad C_6H_5CH_2 \quad (+M) \quad \rightarrow \quad C_{14}H_{14} \quad (+M) \qquad k_1 \qquad (3.3.1)$$
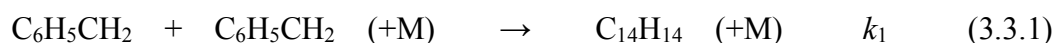
As shown in Chapter 1, Oum *et al.*[10] studied pressure and temperature dependent combination rate constants of benzyl radicals in helium, argon, xenon, N_2, and CO_2. An unexpected increase of the rate constant above the limiting high-pressure rate constant ($k_{1,\infty}^{ET}$) was reported, which one obtains based on the traditional mechanism. The Radical–Complex mechanism has been successfully used to reproduce the observed rate constants of the benzyl radical combination reaction. This mechanism is related to the strength of van der Waals type interactions between radical and solvent molecules (AM) (A denotes the target radical, and M is the bath gas). One of the important factors is the well-depth of the bath gas. Usually the effective well-depth of AM is influenced by several molecular properties such as dipole moment and polarizability. CF_4, CF_3H and SF_6 are good candidates as solvent molecules to elucidate how combination rate constants are influenced by the nature of the radical-solvent molecule interaction.

In this work, we investigated pressure-and temperature-dependent combination rates of benzyl radicals in CF_3H, CF_4 and SF_6 over the pressure range 1-50 bar and temperature range 250-400 K, where earlier measurements in CO_2 showed a marked increase of rate constants beyond the plateau of the limiting high-pressure rate constant.

In ref. 10, the influence of the co-bath gas effect was investigated using bath gas mixtures of argon and xenon. No notable increase of k_1 compared to the measurements in pure argon was found, indicating that the contribution from quenching of electronic states by heavy atoms is insignificant in the benzyl radical recombination. From the earlier measurements of

benzyl radical recombination in refs. 9 and 10, the most significant increase of k_1 was observed in CO_2, and the least in helium. Based on this information, the co-bath gas effect on the increase of the combination rate constant k_1 of benzyl radical was investigated in bath gas mixtures of CO_2 and helium in the range of $40 - 160$ bar at 300 K. In ref. 10, the decrease of the rate constant, k_1, due to the influence of diffusion was not observed in CO_2, because it was difficult to reach more than 50 bar CO_2 without a compressor. The rate constant k_1 of benzyl radicals was therefore measured in the high-pressure range up to 60 bar in CO_2 at 300 K in this work.

In this work, benzyl radicals were generated by the laser photolysis of Cl_2 at 308 nm using an excimer laser, and the subsequent fast bimolecular reaction of chlorine atoms with an excess amount of toluene.

$$Cl_2 \quad + \quad h\nu \quad (308 \text{ nm}) \quad \rightarrow \quad 2\ Cl \qquad (3.3.2)$$

$$Cl \quad + \quad C_6H_5CH_3 \quad \rightarrow \quad C_6H_5CH_2 \quad + \quad HCl \qquad (3.3.3)$$
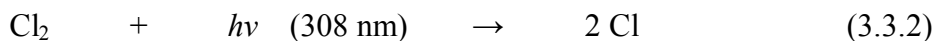
The recombination rate constant, k_1, of reaction (3.3.1) was measured by monitoring the UV-absorption signal of benzyl radicals at 253 nm on time scales of µs to ms.

According to ref. 10, the reaction (3.3.1) is the major channel, and other possible side reactions should be insignificant, because toluene was always present in excess. Also, due to the small absorption coefficients of products like bibenzyl ($\sigma_{bibenzyl} \approx 1.0 \times 10^{-19}$ $cm^2 molecule^{-1}$)[5] compared to the strong absorption of benzyl radical, the effect of residual absorption from products should be negligible. Typical concentrations of chlorine and toluene were: $[Cl]_0 = (1–5) \times 10^{13}$ molecule cm^{-3} and $[Toluene] = (0.7–7) \times 10^{16}$ molecule cm^{-3}. Because of the second order kinetics of reaction (3.3.1), measured k_1 values are very sensitive to the absorption coefficient of benzyl radicals. In the present work, the temperature dependent $\sigma_{benzyl}(T)$ values from ref. 10 were used, which are in good agreement with the literature value of Ikeda *et al.*[42]

$$\sigma_{benzyl}(T) \approx 1.3 \times 10^{-16} \left(\frac{T}{300K}\right)^{-0.25} cm^2 molecule^{-1} \qquad (3.1.4)$$

3.3.1 Absorption-time profiles at 253 nm

Figure 3.3.1 shows a typical absorption signal of benzyl radicals at 253 nm, recorded after the 308 nm laser photolysis of Cl_2 in the presence of toluene and the bath gas SF_6 at 300 K. All absorption-time profiles showed an instant increase of the benzyl radical concentrations, which then was followed by a clean second-order decay. The fits did not show any systematic deviations, giving additional support to the reported values of k_1.
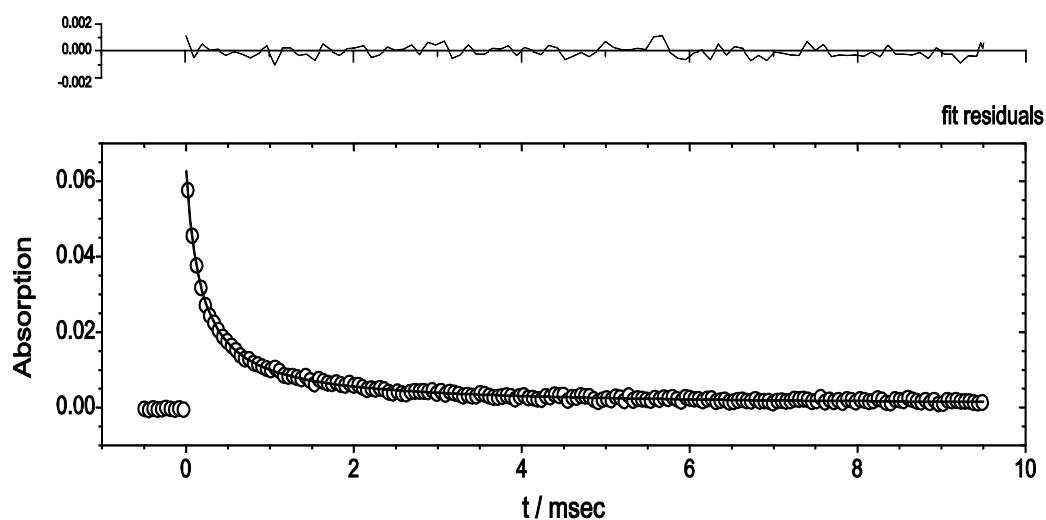
Figure 3.3.1 Typical transient absorption signal of benzyl radicals at 253 nm, recorded after the photolysis at 308 nm of mixtures of 0.42 mbar of Cl_2, 2.10 mbar of toluene and 6 bar SF_6 at 300 K. The upper figure is the fit residual.

3.3.2.   Pressure - dependent absorption coefficients of benzyl radicals, σ(*P, 300 K*)

In ref. 10, no significant spectral shift of the absorption band of benzyl radicals in the wavelength range 240 – 268 nm was observed over the pressure range 7 – 37 bar in CO_2. The maximum absorption values as a function of the SF_6 bath gas pressure were also measured in this work to confirm the pressure dependence of σ_{benzyl}. Figure 3.3.2 shows the maximum absorption values as a function of the SF_6 bath gas pressure. $\sigma_{benzyl} = 1.3 \times 10^{-16}$ $cm^2 molecule^{-1}$ at 253 nm in this pressure range was used to obtain the k_1 value from fitting. The observed linear relationship is consistent with a constant absorption coefficient.
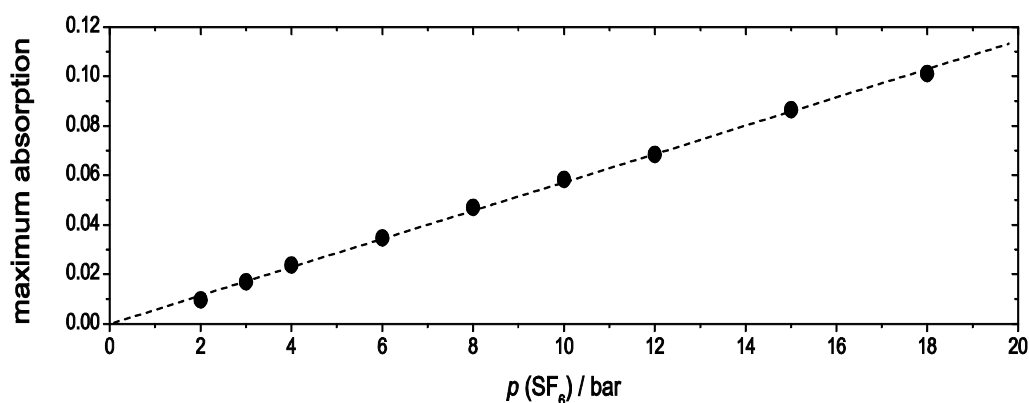
Figure 3.3.2   Maximum absorption of benzyl radicals at 253 nm at different SF_6 pressures (2 - 18 bar) with constant $[Cl_2]$ / [bath gas] ratio.

3.3.3. Pressure dependence of the rate constant k_1

The results of the pressure dependence of k_1 at 300 K are shown in Figure 3.3.3 and summarized in Table 3.3.1. From the constant k_1 values at low pressures, one can directly determine the limiting high-pressure rate constant $k_{1,\infty}^{ET}$ of the ET mechanism. It is also noticeable that the constant k_1 values are bath gas independent. To determine the $k_{1,\infty}^{ET}$, the k_1 values at the lowest pressure in each bath gas were averaged.

We determine $k_{1,\infty}^{ET}$ for the reaction as:

$$k_{1,\infty}^{ET} = 4.1 \times 10^{-11} \mathrm{cm^3 molecule^{-1} s^{-1}} \qquad (3.3.5)$$

which is in agreement with the previous work from ref. 10. The increase of the rate constant over the range 2 – 60 bar were observed in the bath gas SF_6, CF_3H, and CF_4 at pressures beyond the "high-pressure limit" of the ET mechanism.
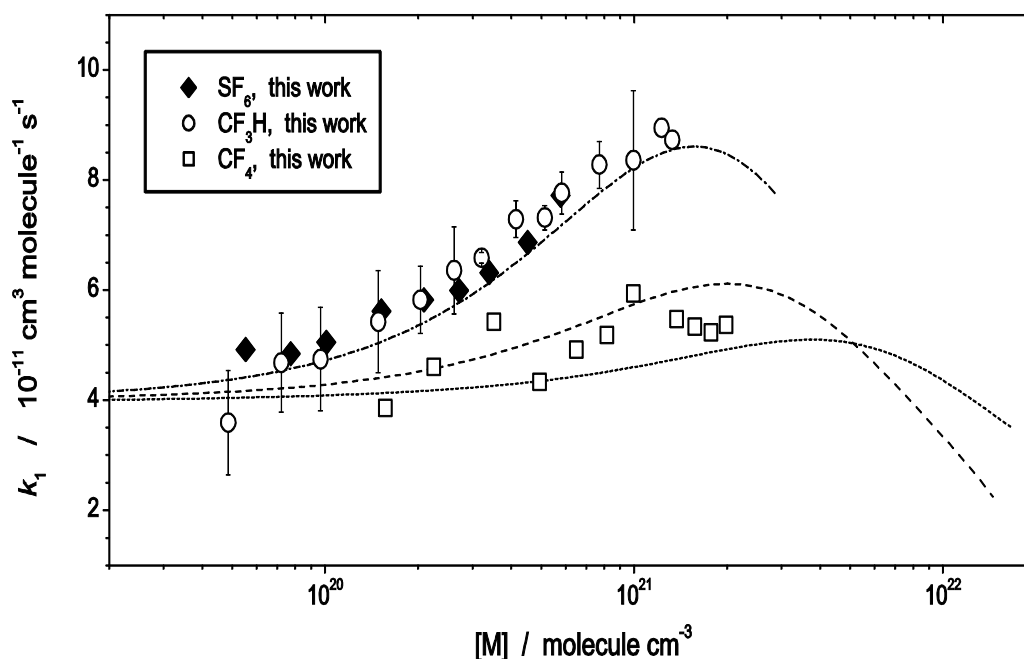
Figure 3.3.3   Recombination rate constant k_1 in SF_6 (♦), CF_3H (○) and CF_4 (□) at 300 K. Lines indicate the simulation from the kinetic model for CO_2 (-•-), Ar (---), and He (•••) from ref. 10, given for comparison.

Table 3.3.1   Rate constants k_1 of the combination reaction of benzyl radicals in CF_4, SF_6 and CF_3H at 300 K.

(a) M = CF_4 at 300 K

p (CF_4)[a]	[CF_4] [b]	k_1 [c]	p (CF_4) [a]	[CF_4] [b]	k_1 [c]	p (CF_4) [a]	[CF_4] [b]	k_1 [c]
7	1.56E20	3.9	25	6.49E20	4.9	50	1.57E21	5.3
10	2.25E20	4.6	30	8.15E20	5.2	55	1.77E21	5.2
15	3.52E20	5.4	35	9.92E20	5.9	60	1.98E21	5.4
20	4.94E20	4.3	45	1.37E21	5.8			

(b) M = SF_6 at 300 K

p (SF_6) [a]	[SF_6] [b]	k_1 [c]	p (SF_6) [a]	[SF_6] [b]	k_1 [c]	p (SF_6) [a]	[SF_6] [b]	k_1 [c]
2	4.80E19	4.9	6	1.56E20	5.6	12	3.39E20	6.3
3	7.46E19	4.9	8	2.13E20	5.8	15	4.48E20	6.9
4	1.01E20	5.1	10	2.74E20	6.0	18	5.75E20	7.7

(c) M = CF_3H at 300 K

p(CF_3H)[a]	[CF_3H][b]	k_1[c]	p(CF_3H)[a]	[CF_3H][b]	k_1[c]	p(CF_3H)[a]	[CF_3H][b]	k_1[c]
2	4.86E19	3.6	10	2.61E20	6.4	25	7.72E20	8.3
3	7.20E19	4.7	12	3.21E20	6.6	30	9.96E20	8.4
4	9.66E19	4.8	15	4.15E20	7.3	34.2	1.23E21	9.0
6	1.49E20	5.4	18	5.14E20	7.3	41.6	1.33E21	8.7
8	2.04E20	5.8	20	5.83E20	7.8			

[a] Pressure of the bath gas, given in bar. [b] Density of the bath gas, given in molecule cm^{-3}.
[c] Rate constant, given in 10^{-11} cm^3 molecule^{-1} s^{-1}.

3.3.4. Temperature dependence of the rate constant k_1

The temperature dependence of k_1 was investigated in the bath gases CF_3H and SF_6 and the results are illustrated in Figure 3.3.4 and Figure 3.3.5 over the range 275–400 K and summarized in Table 3.3.

Figure 3.3.4   Density dependence of the combination rate constant k_1 in CF_3H at different temperatures. Lines are the results from a fit in terms of the Radical-Complex mechanism with consideration of diffusion at high pressures. (-•-) : 275K, (---) : 300 K and (•••) : 350 K.
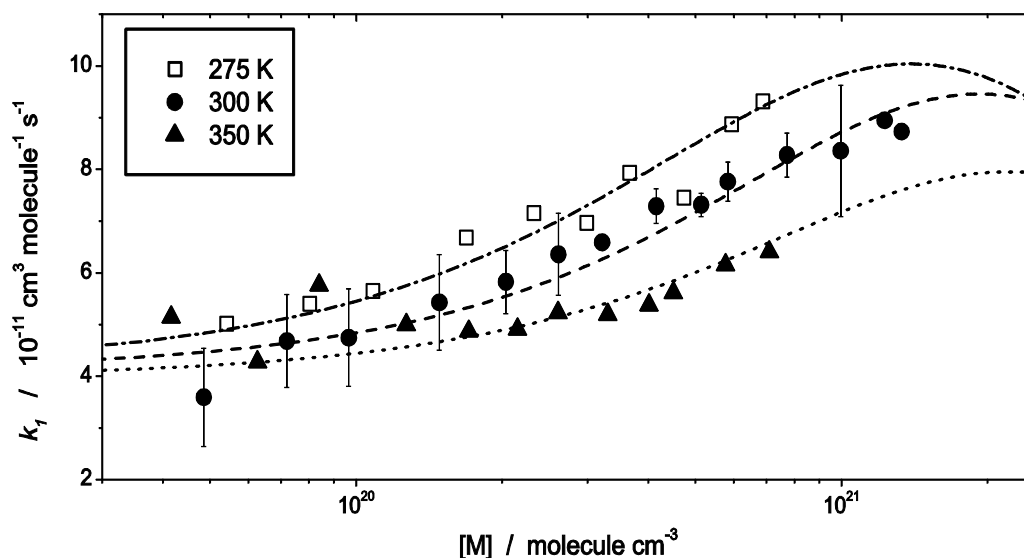

Figure 3.3.5   Density dependence of the combination rate constant k_1 in SF_6 at different temperatures. Lines are the results from a fit in terms of the Radical-Complex mechanism with consideration of diffusion at high pressures. (-•••-) : 275K, (---) : 300 K, (•••) : 350 K and (-•-) : 400 K.
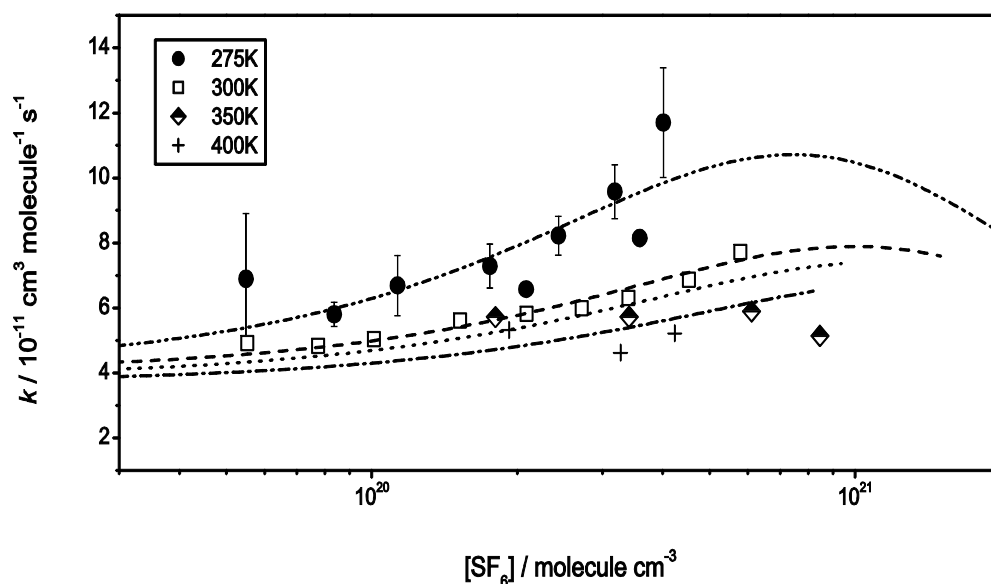
Pronounced temperature dependence with a stronger increase of the rate constants at lower temperatures was determined, both in CF_3H and SF_6. A more pronounced temperature-dependence in SF_6 than in CF_3H was observed.

Table 3.3.2   Rate constants of the combination reaction of benzyl radicals (k_1) in CF_4 at 275 K and 350 K and in SF_6 at 275 K, 350 K and 400 K

(a) M = CF_3H at 275 K								
$p(CF_3H)^a$	$[CF_3H]^b$	k_1^c	$p(CF_3H)^a$	$[CF_3H]^b$	k_1^c	$p(CF_3H)^a$	$[CF_3H]^b$	k_1^c
2	5.42E19	5.0	8	2.32E20	7.1	15	4.74E20	7.5
3	8.03E19	5.4	10	2.98E20	7.0	18	5.94E20	8.9
4	1.08E20	5.7	12	3.66E20	7.9	20	6.88E20	9.3
6	1.69E20	6.7						

(b) M = CF_3H at 350 K								
$p(CF_3H)^a$	$[CF_3H]^b$	k_1^c	$p(CF_3H)^a$	$[CF_3H]^b$	k_1^c	$p(CF_3H)^a$	$[CF_3H]^b$	k_1^c
2	4.16E19	5.1	8	1.71E20	4.9	18	4.01E20	5.4
3	6.27E19	4.3	10	2.15E20	4.9	20	4.50E20	5.6
4	8.39E19	5.8	12	2.61E20	5.2	25	5.77E20	6.2
6	1.27E20	5.0	15	3.30E20	5.2	30	7.10E20	6.4

(c) M = SF_6 at 275 K								
$p(SF_6)^a$	$[SF_6]^b$	k_1^c	$p(SF_6)^a$	$[SF_6]^b$	k_1^c	$p(SF_6)^a$	$[SF_6]^b$	k_1^c
2	1.76E18	6.9	6	1.22E20	7.4	12	3.48E20	10.7
3	3.04E19	5.5	8	1.90E20	8.0			
4	5.99E19	6.9	10	2.65E20	9.6			

(d) M = SF_6 at 350 K								
$p(SF_6)^a$	$[SF_6]^b$	k_1^c	$p(SF_6)^a$	$[SF_6]^b$	k_1^c	$p(SF_6)^a$	$[SF_6]^b$	k_1^c
4	9.25E19	7.6	11	3.39E20	5.7	18	8.45E20	5.7
7	1.79E20	5.7	15	6.09E20	5.9			

(e) M = SF_6 at 400 K								
$p(SF_6)^a$	$[SF_6]^b$	k_1^c	$p(SF_6)^a$	$[SF_6]^b$	k_1^c	$p(SF_6)^a$	$[SF_6]^b$	k_1^c
9	1.91E20	5.32	14	3.31E20	4.62	17	4.23E20	5.22

[a] Pressure of the bath gas, given in bar. [b] Density of the bath gas, given in molecule cm^{-3}.
[c] Rate constant, given in 10^{-11} cm^3 $molecule^{-1}$ s^{-1}.

3.3.5. Measurement of k_1 in CO_2-He mixtures

From previous measurement results of combination reactions of benzyl radicals, it was found that the magnitude of enhancement of k_1 is the largest in CO_2, and the smallest in helium. The combination of CO_2 and He is a good candidate to investigate co-bath gas effects on k_1. First, the influence of co-bath gas effect at constant CO_2 pressure and varying helium pressures on the combination rate constant k_1 was investigated, and the results are represented in Figure 3.3.6 and summarized in Table 3.3.3.

Figure 3.3.6   Density dependence of the combination rate constant k_1 in the bath gas mixture of CO_2 and He at 300 K. ($\bullet$) : constant CO_2 pressure 46 bar + varied He pressure (25 - 110 bar), (half-filled diamond) : constant CO_2 pressure 20 bar + varied He pressure (20 - 90 bar), ($\square$) : pure CO_2, (+) : pure He, Lines = rate constants for recombination of benzyl radicals in CO_2 ($\bullet\bullet\bullet$), and He (---) from ref. 10.

In ref. 10, the highest pressure measured was 42 bar. However, a decrease of the combination rate constant k_1, due to the contribution of diffusion-control, was not observed up to that pressure. To check the change of k_1 at high pressure, the mixing ratio CO_2 (46 bar) + He (25–110 bar), was selected. In ref. 10, the least increase of rate constant k_1 was observed in the bath gas helium and almost constant k_1 values were measured in the pressure range 20 – 90 bar. The results clearly show that the increase of the rate constant k_1 solely depends on the CO_2 partial pressure. This points toward a preferential solvation of the benzyl radicals by CO_2, and negligibly weak interaction of helium.
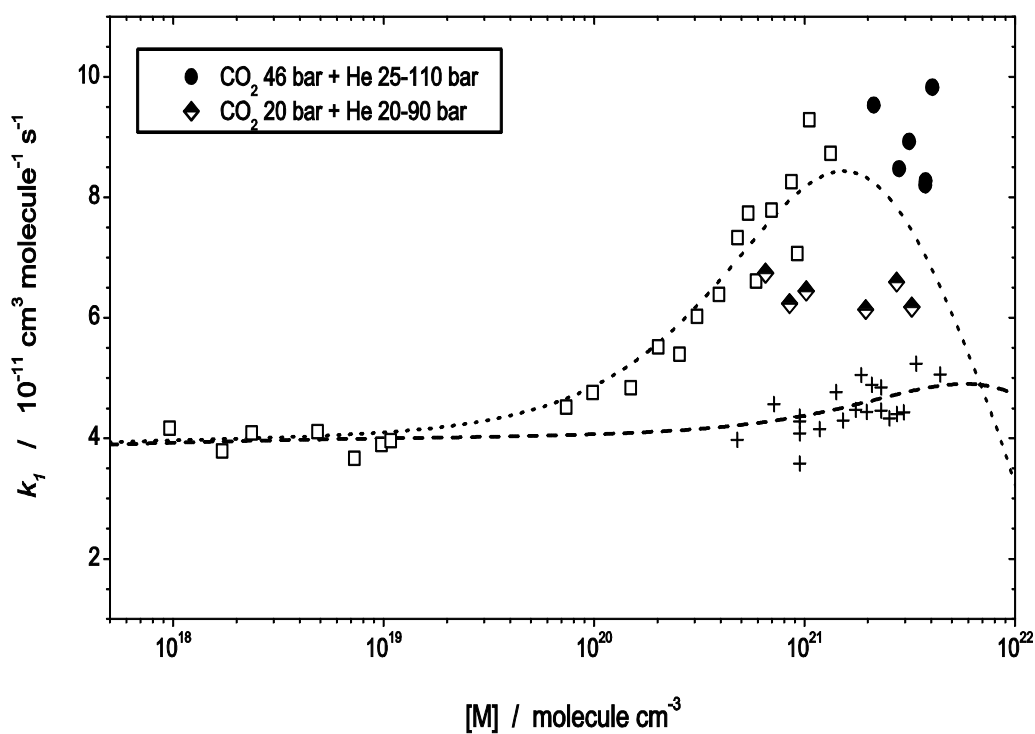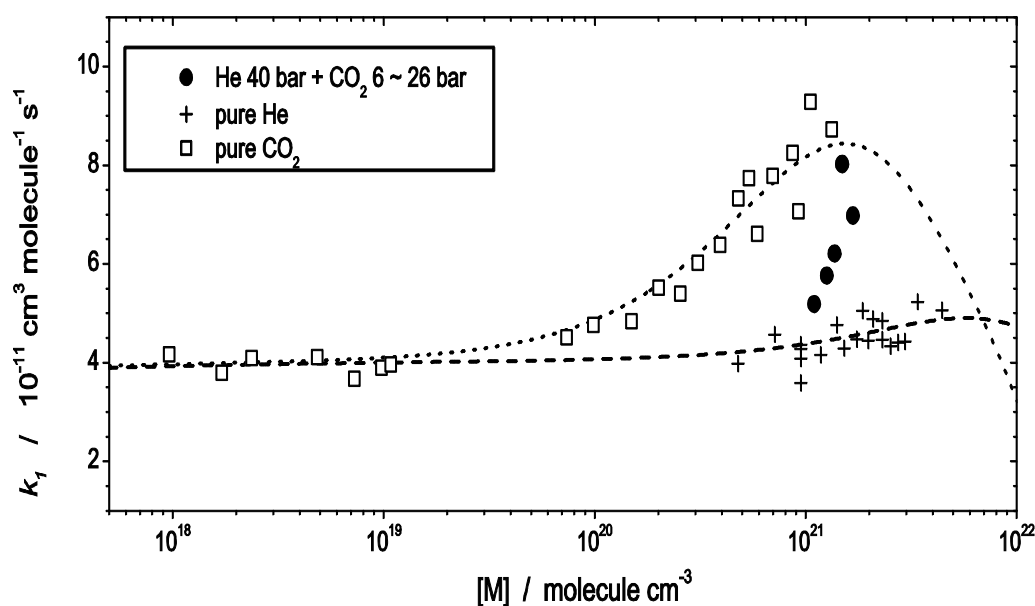

Figure 3.3.7 Density dependence of the combination rate constant k_1 in the bath gas mixture of CO_2 and He at 300 K. (●) : constant He pressure 40 bar + varied CO_2 pressure (6 - 26 bar), (□) : pure CO_2, (+) : pure He, Lines = rate constants for recombination of benzyl radicals in CO_2 (•••), and He (---) from ref. 10.

Table 3.3.3   Rate constants k_1 of the combination reaction of benzyl radicals in He / CO_2 mixtures at 300 K.

(a) M = CO_2 (46 bar) and He (25 – 110 bar) at 400 K

p (M) [a]	[M] [b]	k_1 [c]	p (M) [a]	[M] [b]	k_1 [c]	p (M) [a]	[M] [b]	k_1 [c]
71	2.13E21	9.5	115	3.14E21	8.9	142	3.75E21	8.3
100	2.81E21	8.5	141.5	3.75E21	8.2	155	4.05E21	9.8

(b) M = CO_2 (20 bar) and He (20 – 90 bar) at 400 K

p (M) [a]	[M] [b]	k_1 [c]	p (M) [a]	[M] [b]	k_1 [c]	p (M) [a]	[M] [b]	k_1 [c]
27	6.52E20	6.7	40	1.02E21	6.5	60	1.49E21	6.8
33	8.48E20	6.2	47	1.19E21	5.8	80	1.95E21	6.1

(c) M = He (40 bar) and CO_2 (6 – 26 bar) at 400 K

p (M) [a]	[M] [b]	k_1 [c]	p (M) [a]	[M] [b]	k_1 [c]	p (M) [a]	[M] [b]	k_1 [c]
46	1.10E21	5.2	56.5	1.37E21	6.2	66	1.68E21	7.0
52	1.26E21	5.8	60	1.49E21	8.0			

[a] Pressure of the bath gas, given in bar. [b] Density of the bath gas, given in molecule cm^{-3}.
[c] Rate constant, given in 10^{-11} cm^3 $molecule^{-1}$ s^{-1}.

In contrast, Figure 3.3.7 shows the results, measured under constant He pressure and varying CO_2 pressure conditions. The data clearly show that the density-induced increase of k_1 is correlated with the partial pressure of CO_2, regardless of the specific helium pressure.

3.3.6. Pressure dependence of k_1 in the high pressure range

According to ref. 10, k_1 passes over a maximum and starts decreasing, which can be attributed to a transition to diffusion-controlled kinetics in the bath gases Ar and He. But in CO_2, such a change of k_1 at the highest pressure was not observed because the reachable maximum pressure of CO_2 mixture was around 50 bar and pressure is too low to observe the onset of diffusion control for k_1. Therefore, in this work the pressure dependence of k_1 in the high pressure range up to 70 bar were studied at 300 K and the observed pressure dependence of k_1 is shown in Figure 3.3.8 and summarized in Table 3.3.4
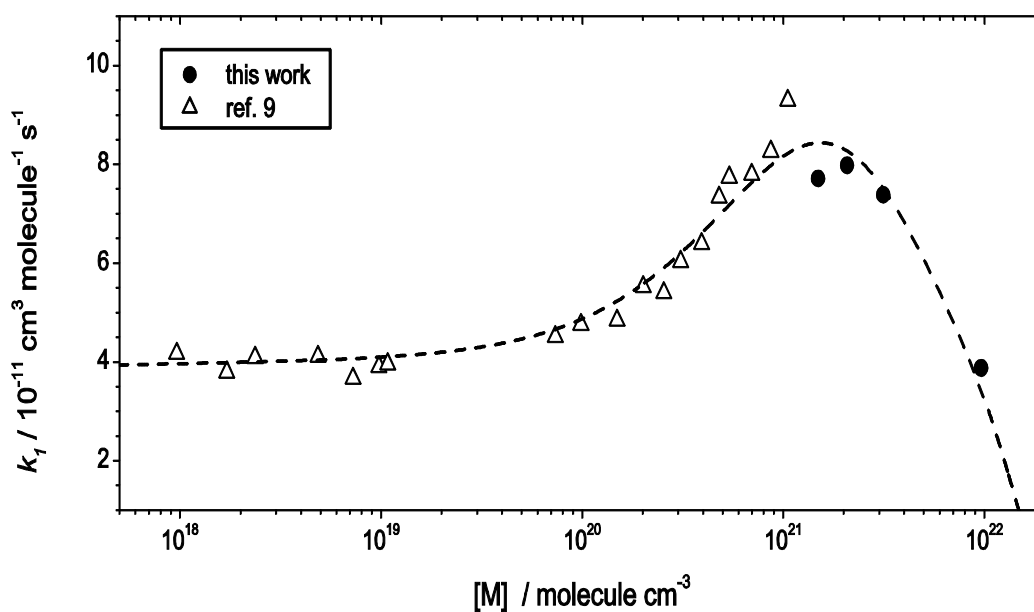

Figure 3.3.8   Recombination rate constant k_1 in CO_2 at 300 K. (Δ) : CO_2 up to 41 bar from ref. 10, ($\bullet$) : CO_2 in the pressure range 45 – 70 bar from this work. Lines = rate constants for recombination of benzyl radicals in CO_2 from ref. 10.

The decrease of the rate constants at pressures above 40 bar in CO_2 was observed like in helium and argon observed in ref. 10 and the observed decrease corresponds to a transition into the regime of diffusion-controlled kinetics. As the increase of k_1 is most significant in CO_2, the transition to diffusion-controlled kinetics was more clearly observed than in helium and argon. Figure 3.3.8 shows that the calculated pressure dependence of k_1 from ref. 10 agrees well with the current experimental results.

Table 3.3.4   Rate constants k_1 of the combination reaction of benzyl radicals in CO_2 (45 – 70 bar) at 300 K.

$$M = CO_2 \text{ at } 300 \text{ K}$$

$p(CO_2)^a$	$[CO_2]^b$	$k_1{}^c$	$p(CO_2)^a$	$[CO_2]^b$	$k_1{}^c$	$p(CO_2)^a$	$[CO_2]^b$	$k_1{}^c$
45	1.49E21	7.7	65	3.14E21	7.4	70	9.66E21	3.9
55	2.10E21	8.0						

[a] Pressure of the bath gas, given in bar. [b] Density of the bath gas, given in molecule cm^{-3}.
[c] Rate constant, given in 10^{-11} cm^3 $molecule^{-1}$ s^{-1}.

Chapter 4

Discussion and outlook

4.1   Transient absorption spectra of benzyl-type radicals

The shape of the room-temperature gas-phase transient absorption bands of *p*-fluorobenzyl near 256 nm and of *p*-methylbenzyl radicals near 263 nm does not significantly differ from that of benzyl radicals. In Figure 4.1, we compare the transient absorption spectra of these radicals. The absorption maxima, corresponding to the $X^2B_2 \rightarrow 4^2B_2$ transition, are shifted to the red for the *p*-fluorobenzyl radicals (max. at ca. 256 nm), for the cumyl radicals (max. at ca. 258 nm) and for the *p*-methylbenzyl radicals (max. at ca. 263 nm), compared to benzyl radicals (max. at 255 nm). Claridge and Fischer[43] investigated several electronic spectra of substituted benzyl radicals in cyclohexane at 295 K. Three band systems have been known with 0-0 transitions from the $^2B_2$ ground electronic state to the 4^2B_2 (near 258 nm), 2^2A_2 (near 316 nm), and 1^2A_2 (near 463 nm) excited states, respectively. The authors found similar red shifts of the absorption maxima of the $X^2B_2 \rightarrow 4^2B_2$ transition for substituted benzyl radicals; e.g., absorption maxima in cyclohexane lie at 258 nm for benzyl radical, at 269 nm for 4-chlorobenzyl, and at 263 nm for 4-methoxybenzyl radicals.
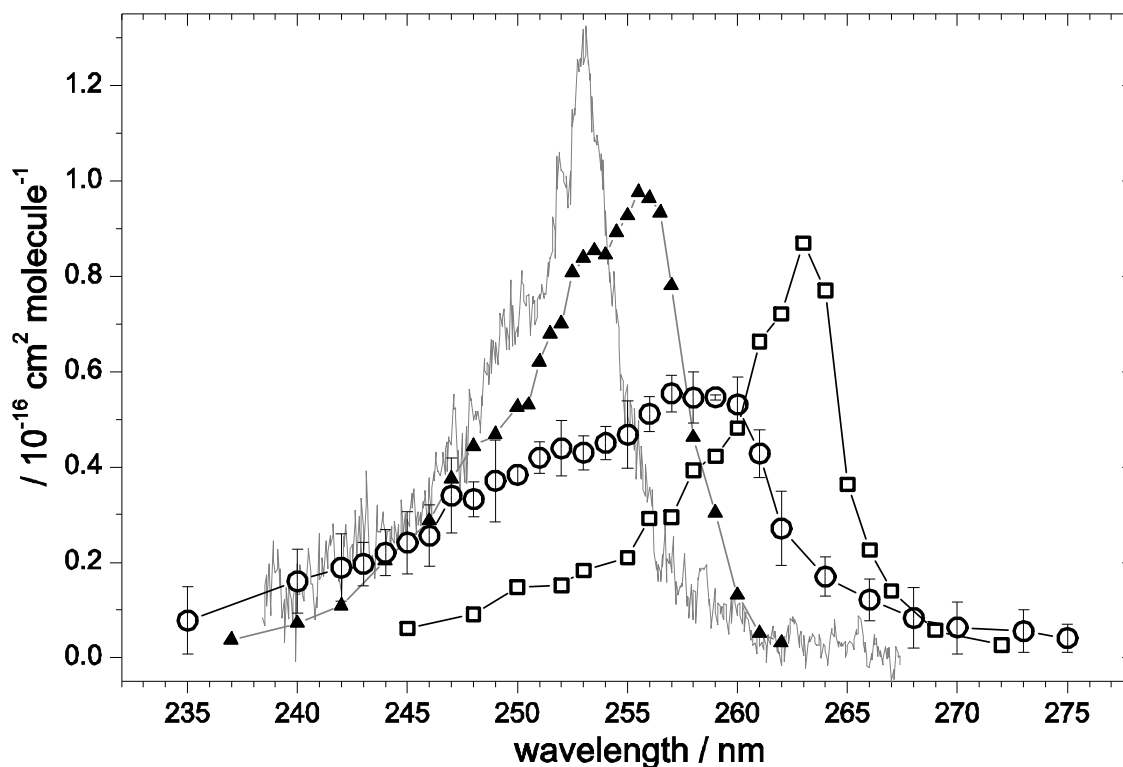
Figure 4.1 Gas-phase transient absorption spectrum of benzyl-type radicals: *p*-fluorobenzyl (▲) , cumyl radicals (○) and p-methylbenzyl radicals (□). Transient absorption spectra of benzyl (solid line)[44] are compared. The figure was taken from ref. 12.

Apparently, the absorption band becomes broad for cumyl radicals in Figure 4.1. The reason for broadening of the absorption band for cumyl compared to benzyl radicals is certainly not due to the vibrational cooling of the radicals. Radicals were prepared from the H-abstraction reactions with Cl atoms:

$$Cl + C_6H_5CH_3 \rightarrow C_6H_5CH_2 \quad + \quad HCl \qquad \Delta H_r = -59.0 \text{ kJ mol}^{-1} \qquad (4.1.1)$$

$$Cl + C_6H_5CH(CH_3)_2 \rightarrow C_6H_5C(CH_3)_2 + HCl \qquad \Delta H_r = -82.4 \text{ kJ mol}^{-1} \qquad (4.1.2)$$

We note that the spectra in Figure 4.1 are "cold" spectra of the corresponding radicals, as they were obtained at total pressures of 5 mbar Ar (benzyl), 350 mbar Ar (*p*-fluorobenzyl) and 4 bar He (cumyl radicals). Under these conditions, radicals are expected to be completely deactivated by collisions with the bath gases. On the other hand, the substitution on the benzyl ring, i.e. *p*-fluoro or *p*-methyl, does not result in significant band broadening.

Furthermore, the maximum absolute absorption coefficients decrease in the order benzyl > *p*-fluorobenzyl ≥ *p*-methylbenzyl > cumyl. A similar reduction of the apparent absorption of

the 258 nm band was observed in several substituted benzyl radicals in solution.[43] For example, they found that the addition of a second chlorine to the benzyl ring lowers the absorption coefficients to ca. 56 %. The authors excluded the possible complex formation of radicals with parent molecules in solution as the reason for such a reduction, as suggested by Sangster et al.,[45] however the reason for such an experimental observation still remains unclear.

We note here that recombination rate constants (k) obtained in this thesis are from a model based on second-order kinetics, where we assumed that the absorption coefficients of the radicals are insensitive to the change of density of the solvent medium. There were some apparent experimental indications that the change in absorption coefficients of benzyl, p-fluorobenzyl and p-methylbenzyl radicals as a function of pressure was only a minor effect, see for example, Figure 3.1.4 and Figure 3.2.7. We note, however, that there is growing experimental evidence of a density-dependent spectral shift and broadening of the absorption bands of the benzyl type radicals from a recent work of Sölter et al.[46] When the details of the pressure-dependent absorption coefficients of the radicals as a function of the pressure of the bath gas, especially CO_2, are available, the density-dependent enhancement of the recombination rate constants obtained in this thesis has to be revisited.

4.2   Limiting high-pressure rate constants of the ET mechanism

In the following sections, we compare the current results on the pressure- and temperature-dependent radical recombination rate constants for three benzyl-type radicals, i.e. benzyl, p-fluorobenzyl and p-methylbenzyl radicals. This can be done from different aspects of the Energy-Transfer mechanism, Radical-Complex mechanism and finally diffusion-controlled kinetics. Figure 4.2 summarizes the current results of the pressure dependence of k_{rec} for those three benzyl-type radicals. Several points can be made. First, *the experimental limiting high-pressure rate constants of the Energy-Transfer mechanism, k_∞^{ET} for the three benzyl-type radicals are very similar* (compare the pressure-independent k_{rec} values below ca. 5 bar):
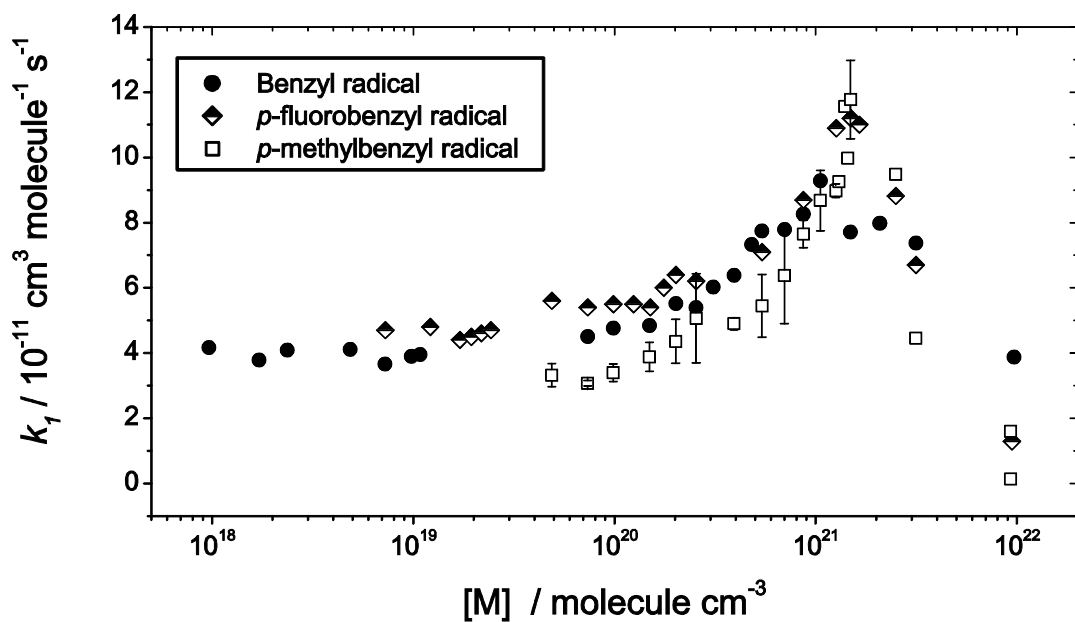
Figure 4.2 Comparison of density dependence of the combination rate constant k_{rec} in CO_2 for benzyl (●), p-fluorobenzyl (◆) and p-methylbenzyl radicals (□) at 300 K. Lines are from the fit in terms of the Radical-Complex mechanism, see text.

$$k_\infty^{ET} \text{(benzyl)} = (4.1 \pm 0.3) \times 10^{-11} \, (T/300 \text{ K})^{-0.45} \text{ cm}^3 \text{ molecule}^{-1} \text{ s}^{-1} \qquad (4.2.1)$$

$$k_\infty^{ET} \text{(}p\text{-fluorobenzyl)} = (4.3 \pm 0.5) \times 10^{-11} \, (T/300 \text{ K})^{-0.2} \text{ cm}^3 \text{ molecule}^{-1} \text{ s}^{-1} \qquad (4.2.2)$$

$$k_\infty^{ET} \text{(}p\text{-methylbenzyl)} = (3.3 \pm 0.3) \times 10^{-11} \, (T/300 \text{ K})^{-0.9} \text{ cm}^3 \text{ molecule}^{-1} \text{ s}^{-1} \qquad (4.2.3)$$

In order to quantitatively understand the effect of the substitution of functional groups to the benzyl rings in the recombination of benzyl-type radicals, we compare the limiting high-pressure rate constant of the ET mechanism given by phase space theory, $k_\infty^{ET, PST}$, as well as the experimental rigidity factors for the three benzyl-type radicals investigated in this work: For benzyl radicals,[10]

$$k_\infty^{ET, PST} \text{(benzyl)} = 1.7 \times 10^{-10} \, (T / 30 \text{ K})^{+0.40} \text{ cm}^3 \text{ molecule}^{-1} \text{ s}^{-1} \qquad (4.2.4)$$

$$f_{rigid}^{exp} \text{(benzyl)} \approx 0.24 \, (T / 300 \text{ K})^{-0.5} \qquad (4.2.5)$$

and for p-fluorobenzyl radicals,[11]

$$k_\infty^{ET, PST} \text{(}p\text{-fluorobenzyl)} = 1.4 \times 10^{-10} \, (T / 300 \text{ K})^{+0.42} \text{ cm}^3 \text{ molecule}^{-1} \text{ s}^{-1} \qquad (4.2.6)$$

87

$$f_{rigid}^{exp} \; (p\text{-fluorobenzyl}) \approx 0.31 \, (T \, / \, 300 \text{ K})^{-0.6} \qquad (4.2.7)$$
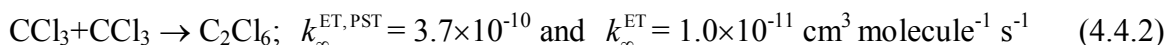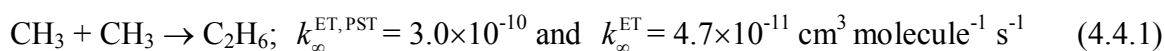
$k_\infty^{ET,PST}$ appear to decrease only slightly on the absolute scale, and slightly increasing experimental rigidity factors as benzyl $\leq$ p-fluorobenzyl.

4.3   RC mechanism

Secondly, the enhancement of k_{rec} beyond the k_∞^{ET} value was observed for all three benzyl-type radicals in the present work, which *qualitatively resembles that of benzyl radicals*. Quantitatively, however, its onset is observed to occur earlier for p-fluorobenzyl radicals (at already ca. 5 bar) than for benzyl radicals (ca. 10 bar). Furthermore, the degree of the enhancement of k_{rec} at higher pressures (before the onset of diffusion control) is somewhat increasing in the order benzyl < p-fluorobenzyl < p-methylbenzyl radicals. This indicates that the limiting high-pressure rate constant of the radical-complex mechanism, k_{AM+AM}, is slightly sensitive to additional substitution of functional groups at the para-position of the benzyl rings: this may influence the rotational hindrance of the radicals and eventually the recombination kinetics.

4.4   Effect of steric hindrance on the recombination rates

The question of the steric effect of the reactants on the recombination rate constants is an interesting but difficult one to answer. For example, from the evaluation of experimental high-pressure rate constants of the radical recombination reactions from Cobos and Troe,[47] $k_\infty^{ET,PST}$ values seem less sensitive to the change of the molecular complexity of the radicals in a series of methyl-type radical reactions, while k_∞^{ET} becomes slower for heavier and larger CCl_3 radicals:

$$CH_3 + CH_3 \rightarrow C_2H_6; \; k_\infty^{ET,PST} = 3.0 \times 10^{-10} \text{ and } k_\infty^{ET} = 4.7 \times 10^{-11} \text{ cm}^3 \text{ molecule}^{-1} \text{ s}^{-1} \qquad (4.4.1)$$

$$CCl_3 + CCl_3 \rightarrow C_2Cl_6; \; k_\infty^{ET,PST} = 3.7 \times 10^{-10} \text{ and } k_\infty^{ET} = 1.0 \times 10^{-11} \text{ cm}^3 \text{ molecule}^{-1} \text{ s}^{-1} \qquad (4.4.2)$$

For *tert*-butyl radical recombination, an even slower $k_\infty^{ET} \approx 4 \times 10^{-12}$ cm^3 molecule^{-1} s^{-1} was reported in ref. 48. It is interesting to note that Naroznik and Niedzielski predict a "stronger"

negative temperature dependence (n) in $k_\infty^{ET}\left(T/300K\right)^{-n}$ as CH_3 ($n = 0.5$, over 300–700 K) < *tert*-butyl ($n = 1.5$) and attribute this due to the steric hindrance. Interesting comparative study to our current results is the investigation of reactive of polycyclic aromatic aryl radicals in the gas-phase. Chen et al.[49] investigated the reactions of phenyl, 1- and 2-naphtahlenyl, and 9-anthracenyl radicals with toluene and naphthalene in the gas-phase at 400 and 450 °C. The relative arylation rates with toluene were almost similar for all 4 radicals, regardless of the complexity of the substitutients to the benzyl-ring. It is important to note that, in order to correlate the kinetic data with respect to the steric effect of the radicals in the recombination reaction, the quantity which one has to compare is probably the rigidity factor, not the absolute limiting high-pressure rate constants.[12]

Such an interpretation can be however irrelevant unless one determines the correct diffusion kinetics of the radicals, where in most cases the interaction between radical and solvent molecules is not considered. The measured values in solution can be simply reflecting the difference in diffusion coefficients of the corresponding radicals, rather than the reactivity of the steric hindrance effect. We state another experimental example. Claridge and Fischer investigated self-termination reaction of several substituted benzyl radicals in solution and discussed about the question whether the slower rates of some of the substituted benzyl radicals, especially 2-chloro and 2-methoxybenzyl, are deviations from complete diffusion control caused by steric factors.[43] The measured termination rate constants (k_t) in cyclohexane decrease from 3.9, 3.1, 1.8×10^{-12}, cm^3 molecule^{-1} s^{-1} for benzyl, 4-chlorobenzyl and 2-chlorobenzyl radicals, respectively. Considering diffusion coefficients of corresponding substituted toluene, the ratio of k_t / k_{diff} was found to be decreasing in the order benzyl (1.23) > 4-chlorobenzyl (1.10) > 2-chlorobenzyl (0.64) radicals. The authors attributed this reduction of the ratio k_t / k_{diff} for more substituted benzyl radicals to the steric hindrance effect. However, it should be mentioned that these authors estimated the diffusion rate constants by the Smoluchowski equation with the diffusion coefficient, D, of the radical approximated by that of the corresponding hydrocarbon, RH: this is then assumed to be the upper limit of the recombination rate constants in solution. At this moment, we can only emphasize the importance of estimate the correct diffusion coefficients of radicals, which must have been overestimated in the work of Claridge and Fischer.[43] Therefore, we cannot tell if their observation of reduced termination rate constants in cyclohexane for substituted benzyl radicals is correlated to the steric hindrance alone or due to the combination of slower diffusion rate constant and steric effects.

4.5 Common features of the role of the RC mechanism in combination reactions of "small" polyatomic and "large" organic radicals

We have presented experimental results of the radical combination reactions of several benzyl-type radicals over the gas-to-liquid transition range. The reaction systems which have been studied here can be grouped into two categories including previous works: one case where the limiting high-pressure rate constant of the energy-transfer mechanism (k_∞^{ET}) is reached at already ca. 1 bar, and the other case where k_∞^{ET} can be reached at relatively higher pressures (e.g., at ca. $\geq$1000 bar) such that the diffusion-controlled kinetics starts influencing on the recombination rate constants at pressures where k_∞^{ET} is not yet reached. The former system includes the combination reactions of CCl_3+CCl_3, CCl_3+Br,[7] the self-combination reactions of benzyl radicals,[10] p-fluorobenzyl radicals[11] and preliminary results of p-methylbenzyl radical recombinations from this thesis. The latter system covers CCl_3+O_2,[50] $O+O_2$,[1,21] and unpublished results of self-combination of ClO radicals.[6] As a general rule, in the latter case, one cannot easily identify and/or separate the role of radical-complex mechanism from the measured recombination rate constants (k_{rec}). This is mainly because the increasing contribution from the radical-complex mechanism on k_{rec} values is added up at higher pressures but still the resulting fall-off curves can appear smooth without revealing an S-shape. Furthermore, near 1000 bar, the diffusion-controlled kinetics will bring down k_{rec} values for most polyatomic radicals, then it is difficult to determine the limiting high-pressure values of both mechanisms. Therefore, such experimental observations of the enhancement of recombination rate constants of large organic radicals in the gas-to-liquid transition region where density-independent k_∞^{ET} is expected, lay the groundwork for identifying and understanding the role of the RC mechanism in radical combination reactions.

4.6 The nature of the radical-solvent molecule interaction

While AM concentrations influence (linearly or quadratically) k^{RC}, the competing ET dynamics is not restricted to the remaining and decreasing concentration of uncomplexed $[A]_{eq} = [A] - [AM]_{eq}$. Radical complexes can as well participate in an ET type dynamics, *e.g.* $AM + A + M \rightarrow A_2M + M$ (or $A_2 + 2M$). Interesting differences may influence the shape of the pressure-dependent transition from k_0^{RC} to k_∞^{RC}. If radical complexes AM are very weak, with correspondingly short life times of AM, the reactions really follow the original "chaperon" model. In these cases the reaction always process under dynamical "high pressure

conditions", i.e. "stabilization" of A_2 (by $A_2M \rightarrow A_2 + M$ or $A_2M_2 \rightarrow A_2 + 2\,M$) is faster than the alternative "redissociation" ($A_2M \rightarrow A + AM$ or $A_2M_2 \rightarrow AM + AM$)." In all such cases the transition corresponds to the same curve of transition $k_0 \rightarrow k_\infty$ which is simply the density dependent increase and saturation of the AM concentration (neglecting here higher complexes). If however AM complexes are bound sufficiently strongly, fast stabilization of the A_2 or A_2M product from AM + AM by dissociation of an M is no longer automatically guaranteed. In such cases even at the saturation level of AM concentration the combination reaction may show further pressure dependence of the ET-type, when the AM "complexes" then mainly behave like somewhat larger ordinary molecules (AM+AM+M), stabilized by additional bath gas collisions.

The interpretation of our observations in terms of a contribution from the radical-complex mechanism can only be correct if the rate constants for the reaction AM+AM are larger than the corresponding values for A+A (likewise, the reaction AM+BM should be faster than A+B). If k_{AM+A} and k_{AM+AM} would not be larger than k_{A+A}, then no rate constant enhancement of k_{rec} would have been observed. It is, therefore, of central importance to rationalize the conclusion about the order of the rate constants, i.e. $k_{A+A} < k_{AM+A} < k_{AM+AM}$.

Our current interpretation in terms of the different rigidity factor appears consistent with the experimental observations. At present these interpretations still have some hypothetical character and need further backup from quantitative tests in other experimental systems and from detailed CT calculations of the capture process on improved potential surfaces. Both are underway and a corresponding comprehensive treatment will be given in the future. However the present study already provides another piece of experimental evidence for the assumed role of the radical-complex mechanism: A pronounced negative temperature dependence of the rate constant enhancement at the elevated densities was observed, just in line with basic expectations for increasing contributions from radical-complex mechanism at decreasing temperatures.

References

(1)   Hippler, H.; Rahn, R.; Troe, J. *J. Chem. Phys.* **1990**, *93*, 6560.

(2)   Hippler, H.; Luther, K.; Troe, J. *Chem. Phys. Lett.* **1972**, *16*, 174.

(3)   Hippler, H.; Luther, K.; Troe, J. *Ber. Bunsen Phys. Chem.* **1973**, *77*, 1020.

(4)   Hippler, H.; Troe, J. *Int. J. Chem. Kin.* **1976**, *8*, 501.

(5)   Baer, S.; Hippler, H.; Rahn, R.; Siefke, M.; Seitzinger, N.; Troe, J. *J. Chem. Phys.* **1991**, *95*, 6463.

(6)   Stark, H. Ph.D. Thesis, Göttingen University, 1999.

(7)   Oum, K.; Luther, K.; Troe, J. *J. Phys. Chem. A* **2004**, *108*, 2690.

(8)   Fernandes, R. X.; Luther, K.; Troe, J. *J. Phys Chem. A* **2006**, *110*, 4442.

(9)   Oum, K.; Sekiguchi, K.; Luther, K.; Troe, J. *Phys. Chem. Chem. Phys.* **2003**, *5*, 2931

(10)   Luther, K.; Oum, K.; Sekiguchi, K.; Troe, J. *Phys. Chem. Chem. Phys.* **2004**, *6*, 4133.

(11)   Lee, C. Y.; Luther, K.; Oum, K.; Troe, J. *J. Phys. Chem. A.* **2006**, *110*, 2613.

(12)   Oum, K. Habilitation Thesis, Uni. Göttingen, 2008.

(13)   Lindemann, F. A. *Trans. Faraday Soc.* **1921**, *17*, 598.

(14)   Christiansen, J. A. Ph.D thesis, Universitaet Kopenhagen, 1921.

(15)   Troe, J. *J. Phys Chem.* **1979**, *83*, 114.

(16)   Porter, G.; Smith, J. A. *Proc. Roy. Soc., A* **1961**, *261*, 28.

(17)   Eusuf, M.; Laidler, K. J. *Trans. Faraday Soc.* **1963**, *59*, 2790.

(18)   Rabinowitch, E. *Trans. Faraday Soc.* **1937**, *33*, 283.

(19)   Bunker, D. L.; Davidson, N. *J. Am. Chem. Soc.* **1958**, *80*, 5090.

(20)   Schwarzer, D.; Teubner, M. *J. Chem. Phys.* **2002**, *116*, 5680.

(21)   Luther, K.; Oum, K.; Troe, J. *Phys. Chem. Chem. Phys.* **2005**, *7*, 2764.

(22)   Troe, J. *Ann. Rev. Phys. Chem.* **1978**, *29*, 223.

(23)   Atkinson, R. *Chem. Rev.* **1986**, *86*, 69.

(24)   Robaugh, D.; Tsang, W. *J. Phys Chem.* **1986**, *90*, 4159.

(25)   Braun-Unkhoff, M.; Frank, P.; Just, T. 22nd Symposium on Combustion,

1988, Seattle.

(26)   Litzingen, T. A.; Brezinsky, K.; Glassman, I. *Combustion Flame* **1986**, *63*, 251.

(27)   Noziere, B.; Lesclaus, R.; Hurley, M. D.; Dearth, M. A.; Wallington, T. J. *J. Phys. Chem.* **1994**, *98*, 2864.

(28)   Poulter, T. C. *Phys. Rev.* **1930**, *35*, 297.

(29)   Poulter, T. C. *Phys. Rev.* **1932**, *40*, 860.

(30)   Bridgeman, P. W. *Rev. Mod. Phys.* **1946**, *18*, 1.

(31)   Hahn, J. Ph.D. Thesis, Uni. Göttingen, 2004.

(32)   Porter, G. *Proc. Roy. Soc. London* **1950**, *A200*, 284.

(33)   Norrish, R. G. W.; Porter, G. *Proc. Roy. Soc. London* **1952**, *A210*, 439.

(34)   Handbook, LOT-Orel.

(35)   Husain, D.; Pritchard, H. O. *J. Chem. Phys.* **1959**, *30*, 1101.

(36)   Kajimoto, O. *Chem. Rev.* **1999**, *99*, 355.

(37)   Brennecke, J.; Chateauneuf, J. E. *Chem. Rev.* **1999**, *99*, 433.

(38)   Gao, D. F.; Stockwell, W. R.; Milford, J. B. *J. Geophys. Res. [Atmos]* **1995**, *100*, 23153.

(39)   Hansen, J. C.; Francisco, J. S. *Chem. Phys. Chem* **2002**, *3*, 833.

(40)   Keck, J. C. *J. Chem. Phys.* **1958**, *29*.

(41)   Hippler, H.; Luther, K.; Troe, J. *Ber. Bunsen Phys. Chem.* **1973**, *77*, 1104.

(42)   Ikeda, N.; Nakashima, N.; Yoshihara, K. *J. Phys. Chem.* **1984**, *88*, 5803.

(43)   Clarldge, R. F. C.; Fischer, H. *J. Phys. Chem.* **1983**, *87*, 1960.

(44)   Fay, N. Untersuchungen zur Temperatureabhängigkeit des Energietransfers hoch schwingungsangeregten Biphenylens. Ph. D. Thesis, Göttingen University, 1997.

(45)   McAskill, N. A.; Sanster, D. F. *Aust. J. Chem. Soc.* **1977**, *30*, 2107.

(46)   Sölter, L. Diploma Thesis, Uni. Göttingen, 2008.

(47)   Cobos, C. J.; Hippler, H.; Luther, K.; Ravishankara, A. R.; Troe, J. *J. Phys. Chem.* **1985**, *89*, 4332.

(48)   Naroznik, M.; Niedzielski, J. *Theor. Chem. Acc.* **2002**, *108*, 103.

(49)   Chen, R. H.; Kafafi, S. A.; Stein, S. E. *J. Am. Chem. Soc.* **1989**, *111*, 1418.

(50)   Luther, K.; Oum, K.; Troe, J. *J. Phys. Chem. A* **2001**, *105*, 5535.

(51)   Shimada, T.; Ojima, Y.; Nakashima, N.; Izawa. Y.; Yamanaka. C. *J. Phys. Chem.* **1992**, *96*, 6298

(52)   Brand. U.; Hippler. H.; Lindemann. L.; Tro. J. *J. Phys. Chem.* **1990,** *94*, 6305

(53)   Bolovinos, A.; Philis, J.; Pantos, E.; Tsekeris, P.; Andritsopoulos. G. *J. Mol. Spectrosc.* **1982**, *94*, 55

(54)   Brouser, L. D.; Mueller-Markgraf. W.; Troe. J. *J. Phys. Chem*. **1988**, *92*, 4905

(55)   Wallington, T. J.;Skewes, L. M.; Siegl, W.O. *J. Photochem. Photobio, A: chemistry*. **1988**, *45*, 167

(56)   Shi. J.; Bernhard, M. J. *Int. Jour. Chem. Kinet.* **1997**, *29*, 349

Curriculum Vitae

Persönliche Daten

Name	Changyoul Lee
Geburtsdatum	20. 01.1975
Geburtsort	Cheonan-si, Südkorea
Staatsangehörigkeit	Südkorea

Ausbildung

03/1991 - 02/1993	Allgemeine Hochschulreife (Jungang High School, Südkorea)
03/1993 - 02/2000	Chemiestudium an der Chungnam National Universität in Daejeon, Südkorea
02/2000	B. Sc in Chemie
11/1994 - 01/1997	Wehrdienst
03/2000 - 02/2002	Masterarbeit mit dem Titel "Electroacoustic application for the enzymatic reaction; the hydrolysis of urea catalyzed by urease" in der Gruppe von Prof. Dr. Joong-Gill Choi an der Yonsei Universität in Seoul, Südkorea
02/2002	M. Sc in Chemie
05/2003 - 03/2004	Gastwissenschaftler von PD. Dr. Kawon Oum am Institut für Physikalische Chemie der Universität Göttingen, Deutschland
04/2004 - heute	Doktorarbeit mit dem Titel " Pressure and temperature dependence of recombination reactions of benzyl-type radicals" in der Gruppe von Prof. Dr. J. Troe und PD. Dr. K. Oum am Institut für Physikalische Chemie der Universität Göttingen, Deutschland